SEISMIC PERFORMANCE EVALUATION OF SEMI-RIGID COMPOSITE COLD-FORMED STEEL-RUBBERISED CONCRETE BUILDINGS

A Thesis

by

Dieudonne Iraguha

Submitted to the

Graduate School of Sciences and Engineering
In Partial Fulfillment of the Requirements for
the Degree of

Master of Science

in the
Department of Civil Engineering

Özyeğin University
March 2023

SEISMIC PERFORMANCE EVALUATION OF SEMI-RIGID COMPOSITE COLD-FORMED STEEL-RUBBERISED CONCRETE BUILDINGS

Advisor: Asst. Prof. Dr. Derya Deniz

Co-Advisor: Asst. Prof. Dr. Alireza Bagheri Sabbagh

Approved by:

Asst. Prof. Dr. Derya Deniz,
Advisor,
Department of Civil Engineering
Özyeğin University

Prof. Dr. Gülay Altay,
Department of Civil Engineering
Özyeğin University

Prof. Dr. Bülent Akbaş,
Department of Civil Engineering
Gebze Technical University

Date Approved: 21 March 2023

“It takes a lot of courage, humility, and self-awareness to look at ourselves closely and with honesty.’’

Todd Davis

ABSTRACT

Over the past few years, cold-formed steel (CFS) structural elements have been extensively used as a cost-effective and fast way of achieving sustainable buildings thanks to their low embodied carbon. Besides, the increased demand for CFS systems in multi-story construction has led to the development of competent CFS lateral force-resisting systems with moment-resisting connections. These rigid connections are implemented to compensate for the shortcomings of traditional CFS framing systems that use simply supported floor-to-wall connections and hence cannot adequately dissipate large moments present in multi-story structures. With this in mind, this study focuses on the seismic performance evaluation of rubberised concrete-filled cold-formed steel (CFS-RuC) tube frames equipped with a recently developed semi-rigid moment-resisting connection. A numerical study is carried out in ABAQUS to examine the effect of different dimensions for CFS-RuC sections and side plates on the behavior of the semi-rigid connection adopted herein. A validation study of the semi-rigid connection is conducted in SAP2000 to come up with a practical plastic hinge model to use at frame-level analysis.

Design of case studies of 2, 5, and 8 story- CFS-RuC buildings is accomplished per the TBEC 2018 and AISI-S100-16 codes. Seismic performance evaluation of the case study buildings at the performance point is investigated through nonlinear static pushover analyses. Alternatively, the seismic behavior of CFS-RuC buildings is probabilistically assessed through fragility curves generated by a fragility tool, SPO2FRAG. Results indicate that these new composite systems possess higher stiffnesses and adequate energy absorption capability in comparison to their bare counterparts. They also displayed a

ductile deformation which enabled the fulfillment of the code-prescribed performance level of life safety.

ÖZETÇE

Son yıllarda, soğuk şekillendirilmiş çelik (CFS) yapı elemanları, düşük karbon içeriği sayesinde sürdürülebilir binaları elde etmenin maliyet etkili ve hızlı bir yolu olarak yaygın bir şekilde kullanılmaktadır. Ayrıca, çok katlı yapı sektöründeki CFS sistemlerine yönelik artan talep, moment aktaran birleşimlere sahip yetkin yanal kuvvete dayanıklı CFS sistemlerin geliştirilmesine yol açmıştır. Bu moment aktaran birleşimler, basit mesnetli döşemeden duvara birleşimleri kullanan ve dolayısıyla çok katlı yapılarda bulunan büyük momentleri yeterince dağıtamayan geleneksel CFS çerçeveleme sistemlerinin eksikliklerini telafi etmek için uygulanmaktadır. Bunu göz önünde bulundurarak, bu çalışma, yakın zamanda geliştirilen yarı rijit moment aktaran birleşimleri ile donatılmış kauçuklu beton dolgulu soğuk şekillendirilmiş çelik (CFS-RuC) boru çerçevelerin sismik performans değerlendirmesine odaklanmaktadır. Farklı CFS-RuC kesit ve yan plakalar boyutların birleşim davranışı üzerindeki etkisini incelemek için ABAQUS'ta sayısal bir çalışma yapılmıştır. Çerçeve düzeyinde analizde kullanılacak basitleştirilmiş bir plastik mafsal modeli bulmak için SAP2000'de yarı rijit birleşimi bir doğrulama çalışması yapılımıştır.

2, 5 ve 8 katlı CFS-RuC binaların parametrik çalışmalarının tasarımı TBEC 2018 ve AISI-S100-16 yönetmeliklerine uygun olarak tamamlanmıştır. Statik itme analizleri ile performans noktasında örnek olay incelemesi binaların sismik performans değerlendirmesi araştırılmıştır. Alternatif olarak, CFS-RuC binalarının sismik davranışı, bir kırılganlık aracı olan SPO2FRAG uygulama tarafından oluşturulan kırılganlık eğrileri yoluyla olasılıksal olarak değerlendirilmiştir. Sonuç olarak, bu yeni kompozit sistemlerin, kauçuklu beton dolgusuz soğuk şekillendirilmiş çelik (CFS) versiyonlar ile

kıyasladığında daha yüksek sertliklere ve yeterli enerji sünme kapasitesine sahip olduğunu göstermektedir. Ayrıca, yönetmelik tarafından belirlenen can güvenliği performans seviyesinin karşılanmasını mümkün kılan sünek bir deformasyon sergilemişlerdir.

ACKNOWLEDGMENTS

Reflecting back to the very first moments of this Master's study: the application process, acceptance to the programme, first lectures, and all the challenges that followed, I realize that without the aid and assistance of numerous individuals, I would not have made it this far.

First and foremost, I would like to express how deeply indebted I am to my advisor, Dr. Derya Deniz. As a hard-working, selfless, and incredible mentor, Dr. Derya is always present and ready to help her students navigate different complexities of research, especially those like me, who came with no research experience. Her endless support and patience offered me the flexibility to explore and acquire more knowledge, which sharpened my research skills. Her generosity with her precious time, knowledge, and resources played key role in the success of my thesis. She consistently encouraged me to keep pursuing opportunities, like attending conferences that would ensure growth and advancement in my career. As a well-connected researcher, Dr. Derya allowed me to participate in a multi-disciplinary research project and collaborate with leading experts in my field. I am very thankful for her prompt feedbacks on my reports and thesis, which helped me improve the quality of my work. I can attest to all positive attributes and inspirations I gained under her supervision. Thanks, Dr. Derya, for everything.

I would also like to acknowledge my co-advisor, Dr. Alireza Bagheri Sabbagh, for his invaluable guidance and feedback throughout our research project. His expertise in my field really intervened when things were starting to get rough and I was stuck not knowing what the next step is. Most importantly, I am grateful for his willingness to share

his model with me, which helped me advance in my analyses. Thanks for inspiring me to consider specializing in this field.

In addition, I also want to extend my thanks to the most esteemed professors on my thesis committee: Prof. Dr. Gülay Altay and Prof. Dr. Bülent Akbaş, for sparing time and agreeing to attend my thesis defense. Their feedback on the content and methodology of my research helped me improve the quality of my thesis. The discussions we had together on multiple occasions regarding the ambiguity of my topic made me considerate of the implications of assumptions found in my work.

Special thanks to the graduate administrative staff, especially Gizem Bakır for being always supportive and for assisting in all academic matters. In particular, I would like to thank her for her tireless efforts in helping me resolve a complex visa matter that could have potentially interrupted my studies.

To my colleagues and friends, thanks for keeping company throughout my academic life. Your energy, presence, and support were what made graduate school loads bearable.

Finally, I want to express my gratitude to my family; since day, one you never ceased to show me love and support. Thank you for supplying me with everything I needed to succeed.

TABLE OF CONTENTS

LIST OF TABLES

LIST OF FIGURES

This page is intentionally left blank

CHAPTER I

INTRODUCTION

1.1 Background and Problem Statement

The disastrous effects of the severe 1999 earthquakes in Istanbul raised huge concerns about the vulnerability of the city's building stock towards likely future earthquakes [1]. These concerns mostly can be attributed to the inadequacy of traditional seismic design methods and structural deficiencies such as stiffness-soft story, horizontal, and vertical irregularities identified in reinforced concrete (RC) buildings. Given that Istanbul is densely populated along with its important role in commercial and cultural activities, a necessity to quickly adopt viable mitigation strategies has emerged. Essentially, in the face of global climate emergencies, mitigation plans to be followed should incorporate both earthquake-resistant systems and ways of cutting significant amounts of carbon emissions associated with the construction process.

Presently, the industrial and construction sectors, which are major contributors to worldwide CO_2 emissions, are currently concentrating on reducing the use of virgin materials by instead opting for the usage of recycled materials. Normally, waste materials that are not recycled end up being stockpiled. Very recently, rubber from scrap tires has found application in the construction sector as a replacement for normal aggregate in concrete [2]. According to some studies, adding rubber to normal concrete improves its energy-dissipative properties (i.e, ductility), which is a preferred property in high seismic like zones Istanbul [3]. Beyond showing improved performance, rubberised concrete (RuC) composites that utilize rubber aggregates from recycled tires, enable less greenhouse gas emissions and have the potential to offer economic benefits. Moreover, shaking table tests on rubberized concrete structures noted that seismic forces on this type of structures were low due to increased damping, therefore allowing designs with fewer materials [3].

With the sustainability criteria in mind, cold-formed steel structural systems have also proven to permit efficient material utilization as they provide lightweight structures and still exhibit high axial and bending capacity [4]. In addition, most cold-formed steel systems employ lightweight steel framing system (LSF). This type of framing has benefits such as reduced construction completion time and less energy consumption hence fewer CO_2 emissions [5]. However, unlike conventional hot-rolled steel framing, which commonly features moment-resisting connections, regular cold formed steel (CFS) systems use simply supported floor-to-wall connections [6], which do not possess adequate moment capacity to dissipate earthquake-induced moments. So, effort in the literature has been made to come up with moment-resisting connections for CFS structures [7]. On the other hand, CFS sections are made of slender elements which are susceptible to premature local buckling, so that's why most CFS sections are designed with underutilized large sections in an attempt to overpass such limit state [17].

In this study, new solutions to the current drawbacks of CFS structures are explored by employing a new composite system of cold-formed steel hollow sections filled with rubberized concrete (CFS-RuC). Validation study of a newly developed semi-rigid connection for the CFS-RuC composite system is conducted to come up with a practical plastic hinge model to use at frame-level analysis. Design of case study CFS-RuC buildings per Turkish Building Earthquake Code (TBEC2018) and North American specification for the design of cold-formed steel (AISI-S100-16) is accomplished. Later, seismic performance evaluation of the case study buildings at the performance point is investigated through nonlinear static pushover analysis. Finally, the seismic behavior of

CFS-RuC buildings is probabilistically assessed through fragility curves generated by the SPO2FRAG tool[62].

1.2 Literature Review

1.2.1 Overview

Occurrence of strong earthquakes like the 1994 Northridge and 1999 Marmara earthquakes led to the upgrading of seismic codes used globally. Nowadays, seismic design of structures situated in high seismic zone ensure that structural elements can sustain large deformations by fulfilling the ductility criteria prescribed by the codes [18]. On the other hand, experimental and numerical studies of researchers have focused on finding alternative energy-dissipative materials and new methods of construction in the context of reducing seismic losses [19].

In this part of the study, brief reviews which are relevant to the topic of this thesis are presented. First, general applications and advantages of concrete-filled steel tube structures are summarized to assist in grasping the fundamental structural behavior of the CFS-RuC composite system to be introduced later. Following that, a comprehensive review of research developments on seismic-resistant systems for CFS structures with a focus on moment-resisting frames is covered, followed by existing studies on rubberized concrete as an environmentally friendly material.

1.2.2 Applications and General Structural Properties of Concrete-Filled Steel Tube Structures

Concrete-filled steel tube structures (CFST) have gained popularity in recent years, owing to several advantages they offer over other conventional construction methods [20]. Among those include high strength and high ductility, reduced labor and materials since formworks can be omitted. Fig. (1-1) shows a typical square, rectangular, and circular hollow sections infilled with concrete where D and B represent the external dimensions of the composite section and t is the thickness of the steel tube. Although circular CFST sections may be preferred for some aesthetic reasons, rectangular and square sections are widely chosen over circular ones since their beam-to-column connection design is less complex.

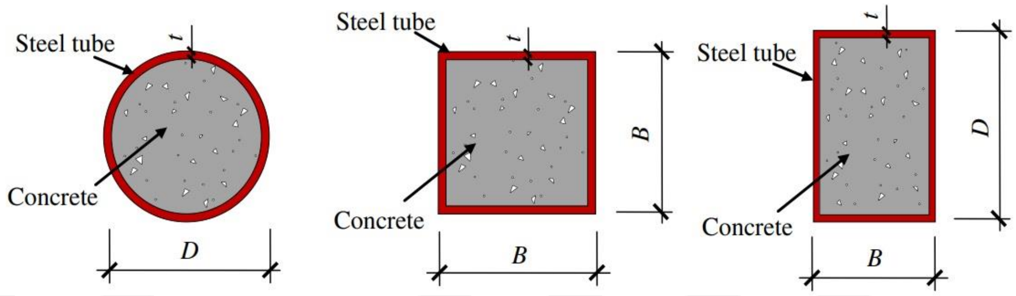

Figure 1-1. Typical circular, square, and circular concrete-filled tube sections [20]

In CFST columns, the outer steel tube applies a confinement effect to the infilled concrete, whereas the concrete restrains the slender steel tube from exhibiting premature local buckling. Fig. (1-2) illustrates the local buckling modes of a square hollow steel tube, concrete, and the corresponding CFST section. The emphasis here is on how the concrete core successfully prevents the inward buckling of the steel tube.

Such effective configuration of steel and concrete in CFST sections allows maximum exploitation of the composite's most prominent characteristics which generates in return a robust system with high compressive capacity and seismic resistance. As a result, CFST systems are deemed suitable for construction where high axial compression capacity is required like in multi-story buildings. Usually, CFST columns are chosen to avoid unnecessary large-size columns which is mostly the case in the design of high-rise RC buildings. Typical setup of the CFST structure is a combination of normal steel beams and steel or RC shear walls connected to the concrete-filled steel tube columns. The sample building shown in Fig. (1-3) is an international commercial building with square

CFST column sections and RC shear walls connected to I-steel beams [21]. It is composed of 24-story and 15-story towers with 84.3 m and 55.5 m in height, respectively. The largest composite column section used here has 600 mm of dimension and a minimum tube thickness of 16 mm was used.

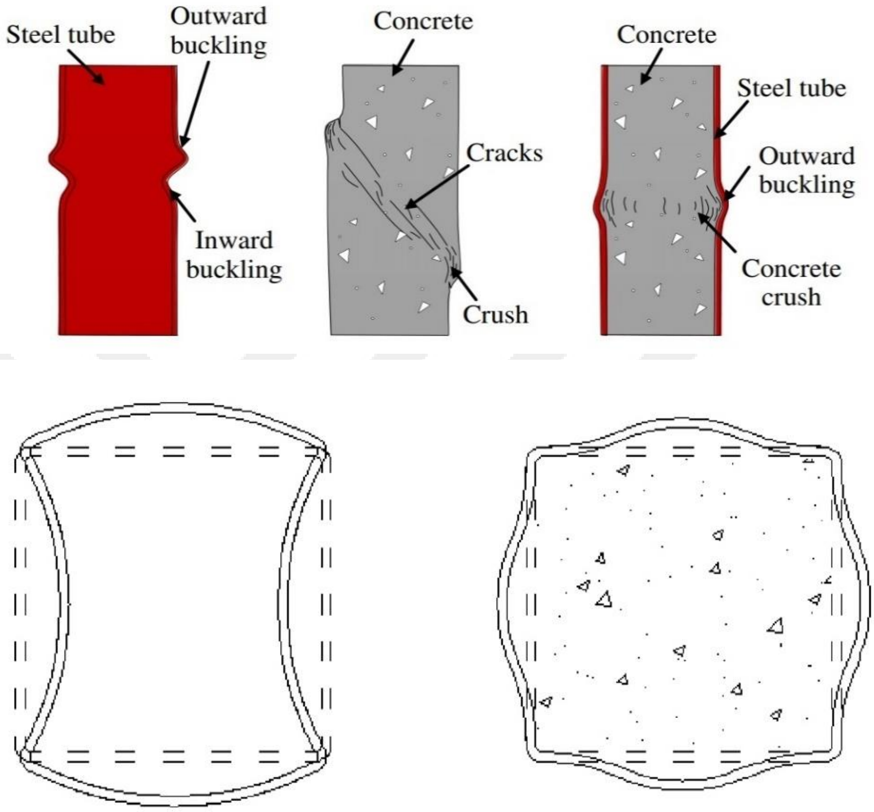

Figure 1-2. Buckling modes of a square hollow steel tube, concrete and CFST section with their top views below [20]

Figure 1-3. Multi-story commercial building featuring CFST columns [21]

1.2.3 Earlier Work on CFS Seismic-Resistant Systems

Over the past few years, cold-formed steel (CFS) structural elements have been extensively used as a cost-effective and fast way of achieving sustainable buildings thanks to their low embodied carbon [22]. The increased demand for CFS systems in multi-story construction has pushed researchers to dedicate their efforts to enhancing the performance of current CFS lateral force-resisting systems. Braced-wall systems are the most common lateral force-resisting systems for CFS buildings, with many applications in single-story structures. Moment-resisting systems using bearing-type bolts are also frequently adapted for CFS buildings in high-seismic regions. Reviews in this part, are progressive research on moment resisting systems with a focus on major features and hindrances present in each developed system.

Special bolted moment frames (SBMF) are the first moment-resisting systems presented by the America Iron and Steel Institute (AISI) as one of the techniques that can be adopted in the seismic design of cold-formed steel buildings. Due to the low rigidity of CFS beam-to-column connections resulting from the slenderness of CFS sections, it was realized that the strong column-weak beam philosophy could not be applied to SBMF connection design. Alternatively, a strong column-weak connection theory can be achieved by designing beams and columns to remain elastic while the slip-bearing action at bolt holes can be relied on to dissipate seismic energy. This concept was verified by Uang et al [7] through cyclic tests on SBMF connections. Additionally, cyclic test results showed that specimens were able to attain a 4% story drift, and at first it was observed that while in the elastic range, the moment connection behaved like a rigid joint until slippage occurred. Therefore, the slippate triggered bearing at bolt holes and later on leading to hardening in strength until collapse.

Although SBMF systems displayed adequate ductility, a variety of CFS moment-resisting frames (MRFs) with different connection configurations and design parameters is required. In the analytical and experimental study performed by Mojtabaei et al, an innovative CFS portal frame which consists of a back-to-back C-channel beam connected to two built-up box columns using gusset plates was developed and monotonically pushed. A parametric study was conducted to assess the effect of axial load levels and width-to-thickness ratios of column sections on energy dissipation capacity, ultimate displacement, and lateral force resistance. The obtained results later revealed that no yielding was observed before the buckling point was reached and the first damage was identified near the column-to-base connection. All MRFs under consideration in this study achieved the sway capacity of 4% drift which is the requirement for special moment frames as per AISC 341 [25]. It was also discovered that an increase in axial load level significantly diminished the ultimate lateral load and ductility ratio of the portal frame. This effect was drastically dominating for column sections with high width-to-thickness ratios. From the parametric study results, CFS frames with high width-to-thickness ratios were deemed inadequate for seismic design since they experience premature local buckling hence low ductility.

The research on the seismic performance of CFS moment-resisting frames was further extended by the numerical and experimental study conducted by Bagheri Sabbagh et al.(2011) [16] where the effects of connection types and arrangement of cross-sections were accounted for in the seismic behavior evaluation. In this study, experimental results were used to validate results obtained in the finite element analysis. As displayed in Fig. (1-4) both results present the same limit states and deformability. It was also highlighted that using an increased number of bends on beam flanges and out-of-plane stiffeners as shown in Fig. (1-4) improved the rigidity of the member thus improving the elastic and post-elastic behavior. Additionally, curved beam flanges with infinite bends were able to shift the local buckling to the web through the arching action of flange elements. Similarly, it was also pointed out that assigning at least two pairs of out-of-plane stiffeners was enough to delay the buckling of web and flange elements. In comparison to sections without stiffeners, the aforementioned minimum configuration of out-of-plane stiffeners resulted in a 28% increase in the moment capacity of beams and a 50% increase in the connection ductility.

Unlike in the above-stated study, where the load path is only considered to be from the beam web to the gusset plate (web-connected), Papargyriou et al [26] suggested new CFS connection configurations that allow the load to not only be transferred through the beam web but also can be transmitted through flange elements as well (flange-connected). This kind of implementation was compared to the web-connected and web-and-flange-connected configurations to assess the effects of different configurations on the deformability, bearing strength, and stiffness of the connection.

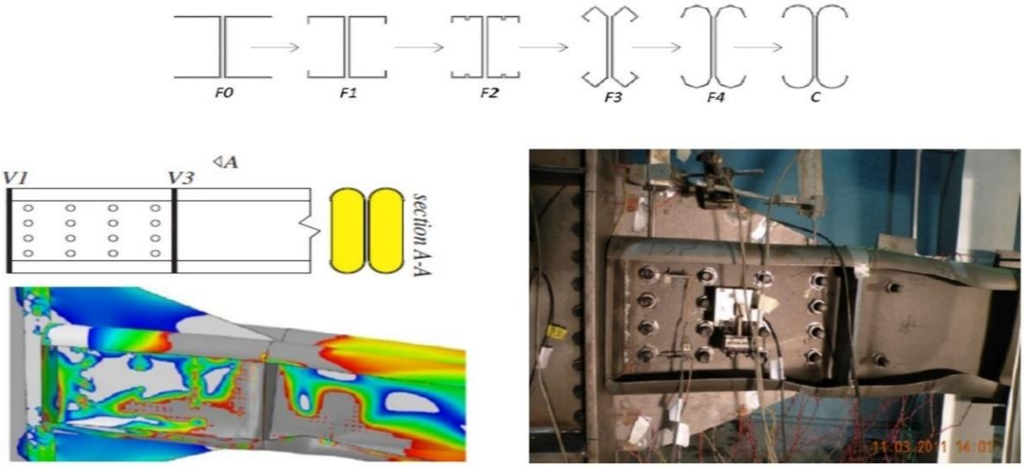

Figure 1-4. Out of plane stiffener configuration and local buckling deformations of specimens

Fig. (1-5) shows a 3D view of the different connection types involved in this study. For the web-connected connections, it was later inferred that a rounded T-shaped gusset plate with a thickness twice larger than that of the beam displayed an improved flexural strength and rigidity, while still offering less barrier for the floor system due to its rounded shape. Further, for the flange-connected connections featuring seat angles and stiffeners, four times larger moment capacity and rotational stiffness were obtained in comparison to their unstiffened versions. Finally, the best-performing configuration for the web-and-flange connected connections was the one using seat angles and a gusset plate of thicknesses twice larger than that of the beam but without the top stiffener.

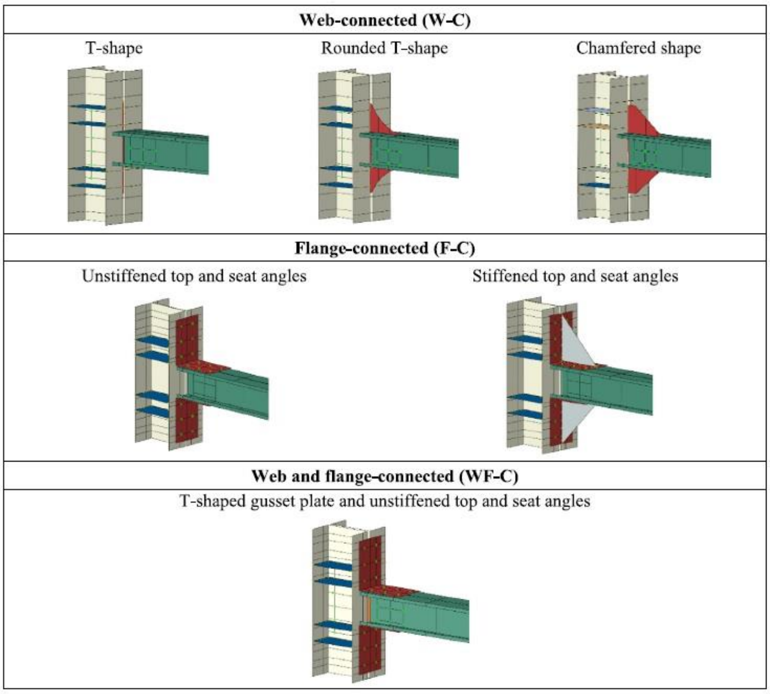

Figure 1-5. 3D graphical representation of connection types [26]

1.2.4 Literature Review In Relation To Rubberised Concrete-Filled Steel Structures

Recently, several attempts have been made to address the environmental and fire risks that recycled tires are likely to pose. As one of the remedies to the waste management issue of recycled tires, researchers proposed the usage of rubber from tires as a replacement material for normal aggregates in concrete [27]. Thanks to the elastic and flexible nature of rubber particles in rubberized concrete (RuC), it displays improved structural properties such as energy absorption capacity and ductility [30]. In one of the studies [31], these were the main properties based on to adopt RuC blocks as flexible roadside barriers since, unlike rigid concrete blocks, upon impact RuC blocks are able to absorb more kinetic energy, therefore, enabling less damage to be endured by the motorists (9, behavior). The negative side of replacing normal aggregates with rubber is that the compressive and tensile strengths of RuC are relatively low in comparison to normal concrete [32]. This issue can be solved by externally confining the RuC core inside steel tubes to restrain it from spalling and cracking under compression. Given the high ductility property of rubber particles, this composite setup generates a more seismic-resistant section.

To understand the behavior of rubberized concrete-filled steel tubes (RuCFST) under axial, flexural, and combined loading, Dong et al [33] conducted an experiment on 30 specimens by varying parameters such as rubber content, section thickness, and load eccentricities. The purpose here was to investigate the practicality of RuC in delaying local buckling (improving the ductility) and to construct interaction diagrams that would facilitate the design of RuCFST. Fig. (1-6) shows the graphical representation of a RuCFST cross-section and the test setup used for column and beam specimens. Experimental results showed that the compressive strength of RuCFST members reduced as the rubber replacement ratio got higher. The strong bond at the interface zone between steel and RuC infill played a huge role in delaying collapse as the deformability of RuC prevented the buckles from quickly propagating. The interaction diagrams were developed following the typical CFST diagram shown in Fig. (1-6). The theoretical calculations and experimental results-based interaction diagrams have approximately predicted the behaviour of RuCFST at an acceptable level.

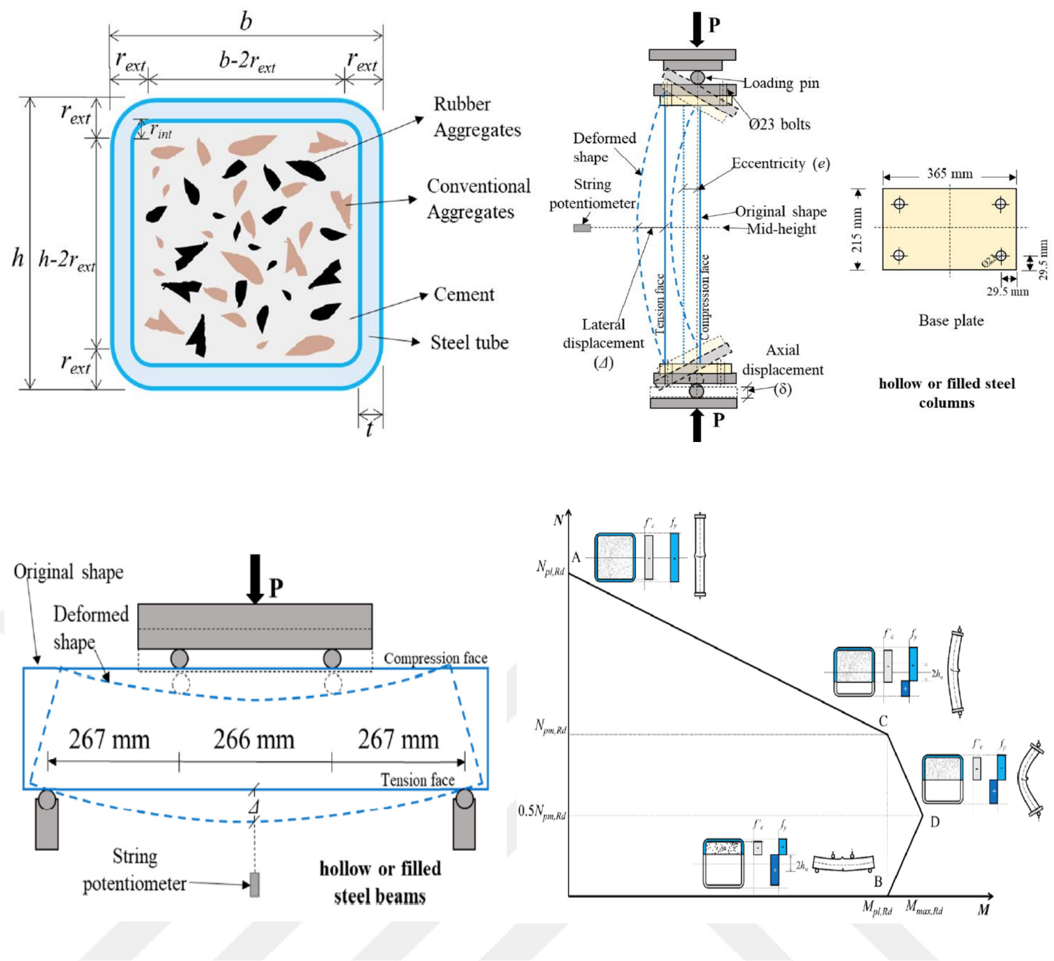

Figure 1-6. RuCFST cross-section and test setup along the interaction diagram for CFST design

Similarly, Silva et al (2017) [34] assessed the flexural behavior of square/rectangular RuCFST columns under monotonic and cyclic bending. Here also, the aim was to investigate the influence of rubber content and cross-sectional slenderness. The experimental campaign consisted of 20 CFST columns. Some of the specimens were filled with normal or rubberized concrete and others were left hollow. For such intensive experimental work, an economical and timesaving method was implemented, where a special steel box was designed to be placed at the bottom of every specimen to provide the required fixity for columns. Results show that both square and rectangular CFST/ RuCFST behaved in a ductile manner under both loadings. During monotonic loading, all specimens nearly maintained their flexural capacities. As expected in the cyclic loading, local buckling of the RuCFST outer section happened, leading to stiffness degradation. For specimens with small thicknesses, fracture of the steel section was observed due to repetitive cycles (fatigue).

Up to this stage, all reviewed studies covered only the behavior of standard concrete-filled steel tubes made with conventional steel. However, the current huge demand for rigid CFS sections in multi-story applications calls for comprehensive studies on composite cold-formed steel sections as a step towards enhancing the axial compression capacity of slender CFS section elements. As shown in Fig. (1-7), Rohola et al [35] developed composite build-up columns from typical CFS slender sections infilled with concrete. Results like load-bearing capacity and failure modes of the composite columns were extracted from the experiments carried out, where columns were axially loaded until failure. To validate experimental results, column steel sections were modeled as shell elements in ABAQUS [36]. The testing campaign involved 12 innovative specimens and design estimations were made using Eurocode EN 1994-1-1 for measuring how accurately the current codes can predict the capacity of such slender elements. Results showed that the failure of rectangular specimens was mainly governed by global buckling, whereas for the square ones, local and distortional buckling dominated. It was also found that the composite setup contributed to the observed high compressive strength of the steel element when compared to its bare steel counterpart. This can be attributed to the restraining effect of the concrete core that prevents buckling of steel.

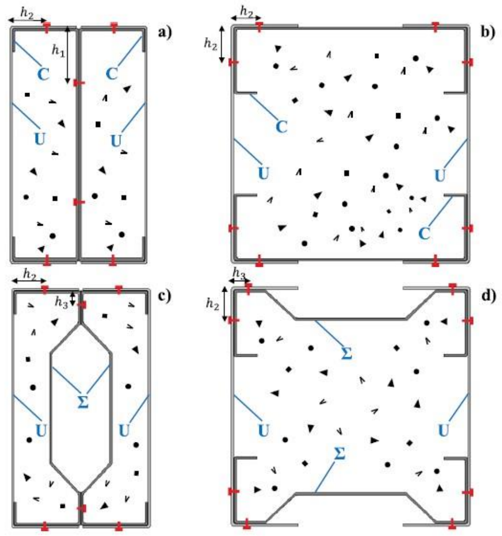

Figure 1-7. The geometry of the composite built-up columns

Very recently, through both experimental and numerical study, Alireza et al [37] proposed a new semi-rigid beam-to-column connection for built-up rubberized concrete-filled cold-formed steel sections. As illustrated in Fig. (1-8) and (1-9), this connection consists of a CFS tubular beam and column filled with rubberized concrete (Ruc) and then connected to each other through side plates that are welded on both column faces and screwed at the beam end. Both composite and bare steel detailed FE models that were involved in the parametric study were subjected to controlled displacement loading. Connections employing bare CFS section elements were predominantly affected by the beam local buckling (BLB) limit state. However, for composite connections, this limit state was either eliminated or postponed owing to presence of infilled RuC. Instead, for this type of connection, side plate plasticity (SPP), yielding and ultimate screw shear (YSS and USS) limit states were the principal failure limit states. Consequently, the moment capacity and ductility of composite connections were found to be high in comparison to the bare steel connections. Lastly, it was concluded that in fact all connections developed within this study can be classified as semi-rigid, and the composite ones appeared to possess higher connection stiffness than their bare counterparts.

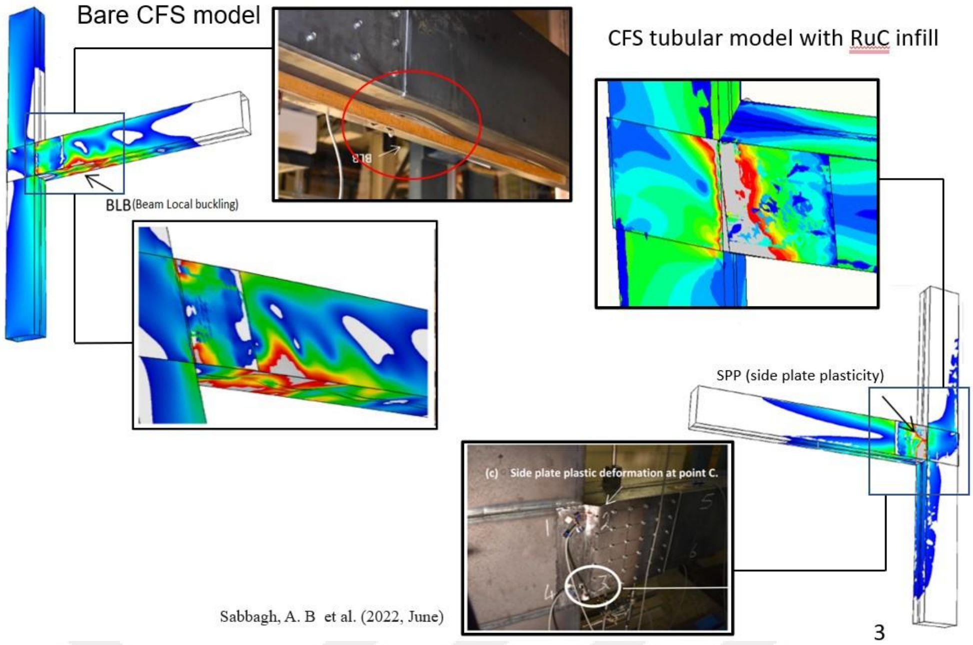

Figure 1-8. Comparison between the numerical and test results of the CFS-RuC connection

1.3 Research Aim

Recent studies on cold-formed steel structures attempted to upgrade their seismic resistance capacity by introducing new moment-resisting connections and different configurations of shear wall systems [7]. Moreover, to address the section slenderness issue of CFS section elements, in some studies, usage of built-up CFS sections and concrete-filled CFS sections was encouraged in order to enhance the axial compression capacity of steel elements. However, in the face of global climate emergencies, extensive studies are required to come up with new solutions that tackle the aforementioned issues of CFS systems as well as the embodied carbon problem of the construction process.

Presented below in Fig. (1-9) is the composite CFS connection system adopted herein and it was earlier proposed by Alireza et al [17]. As already described in the literature review, it consists of rubberized concrete-filled cold-formed steel (CFS-RuC) columns and beams connected through side plates that are welded on the column faces and are then screwed to both faces of the beam. This type of connection system incorporates features that handle the environmental burden caused by recycled tires since rubber particles find application in this rubberized concrete system as aggregates. Additionally, unlike typical steel connections that employ bolted connections, within this system, self-drilling screw connections are featured, which facilitate fabrication and accelerate the installation.

The main objectives of this research work are:

- Develop additional FE models of the CFS-RuC semi-rigid connection in an attempt to rerun the same parametric study conducted by Alireza et al [17]. The primary difference here is that new dimensions of the CFS-RuC beams, columns and sideplates are used to assess how they affect the overall behavior of the connection.
- Create a modeling protocol that facilitates frame-level analysis of structures featuring the CFS-RuC connection.
- To check the applicability of existing design strategies for standard CFST systems when used to design CFS-RuC members.
- To design and evaluate the seismic performance of the CFS-RuC case study buildings according to the requirements of the 2018 Turkish Seismic Code (TSC 2018) [38].

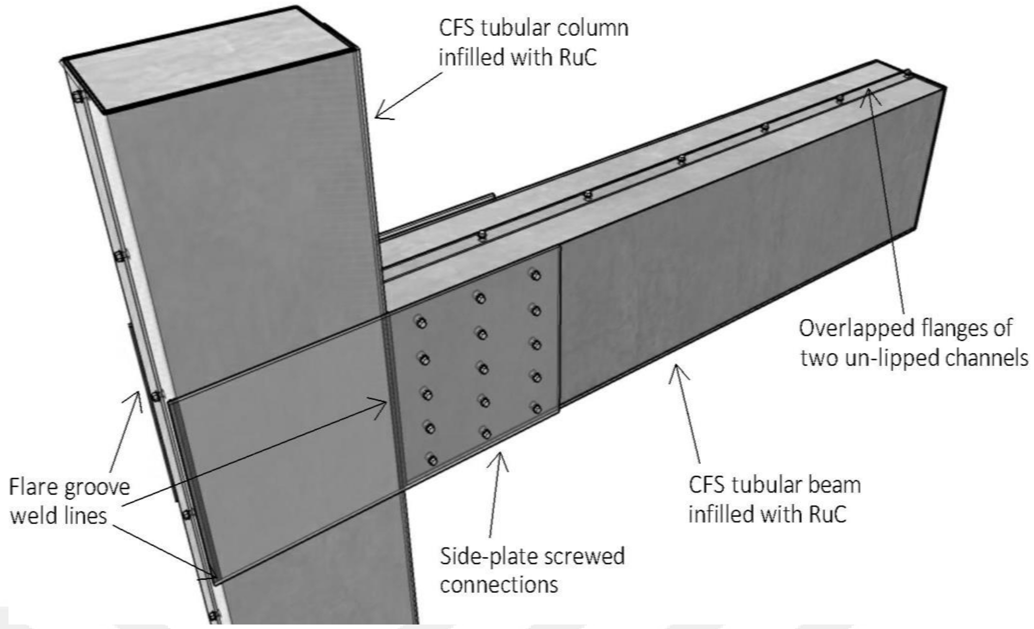

Figure 1-9. Schematic view of the semi-rigid CFS-RuC connection

1.4 Layout of the Thesis

This research is divided into 5 chapters as illustrated in Fig.(1-10). In the first chapter, the background and scope of the study are presented with a focus on moment-resisting connections of cold-formed steel systems and concrete-filled steel tubes structures. Following the introduction, FE analyses of an adopted semi-rigid connection are undertaken and results are discussed, leading to the development of a plastic hinge model to be implemented in chapter 4, where the behaviour assessment of CFS-RuC structures is carried out. Chapter 3 focuses on the alternative design approaches that could be followed in the design of the newly introduced CFS-RuC structures. Different assumptions are made to achieve conservative assignment of sections. The performance chapter aim to assess the lateral load resistance of the semi-rigid connections featured in the CFS-RuC frames through the improved formulation of the capacity spectrum method. The major findings of this study are summarized in the last chapter together with limitations found in this work.

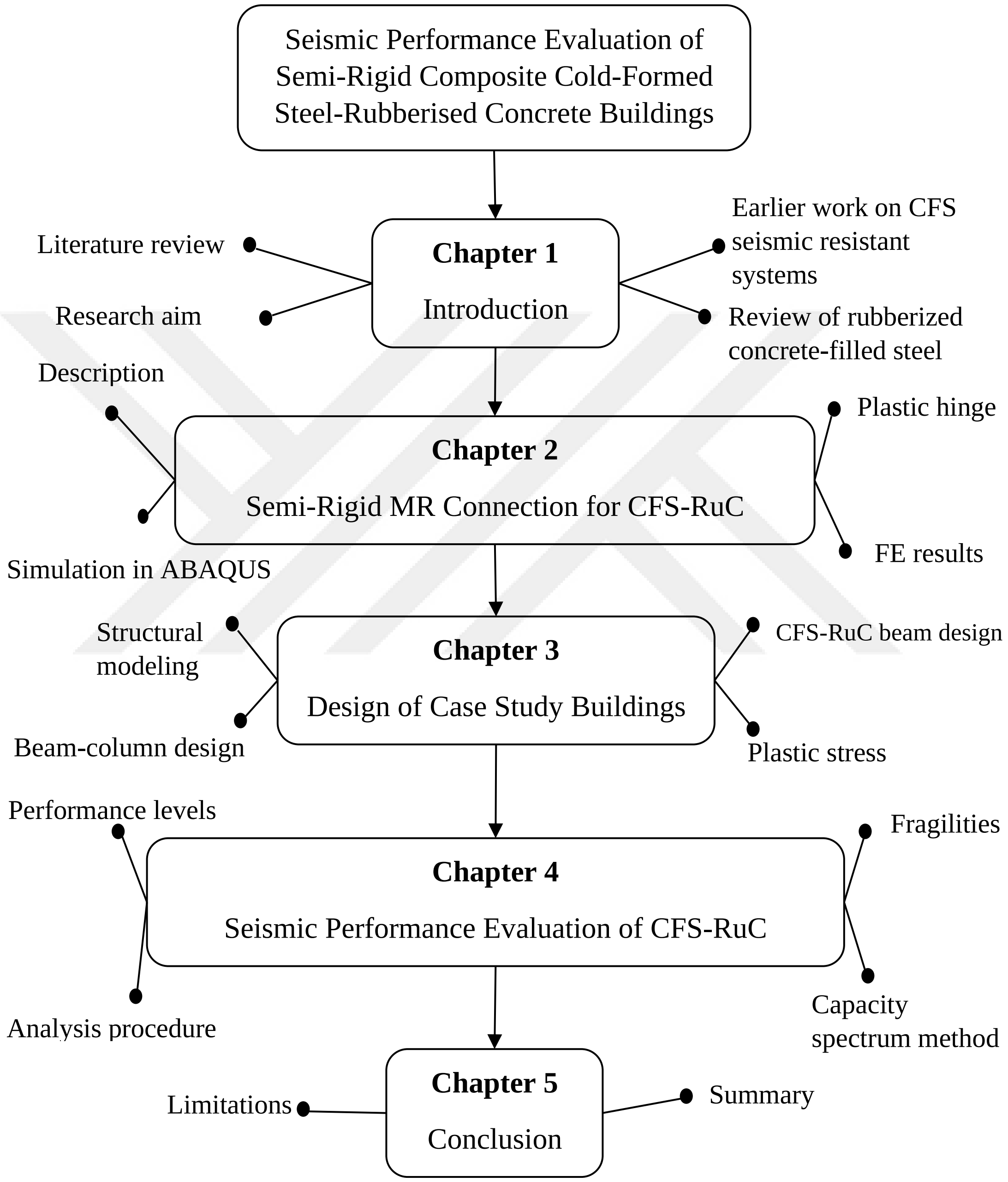

Figure 1-10. Layout of the thesis

CHAPTER II

SEMI-RIGID MOMENT-RESISTING CONNECTION FOR CFS-RUC STRUCTURES

2.1 Overview

Beam-column joints are critical load transmission pathways in a frame system. They are completely responsible for coordinating connection deformations, hence they directly influence the overall seismic performance of a building. Usually, beam-column connections are represented as either simple or moment connections. While simple connections are designed to be flexible pinned joints, which accommodate shear reactions only, moment connections are designated rigid-end joints of restrained beams that resist the combined effects of moment and shear forces. In fact, all connections can be considered as semi-rigid since in reality, it is noticed that actual beam-column joints provide some rigidity even if they are pinned [39].

In steel design, the connection flexibility is expressed in terms of moment-rotation (M-θ) behaviour. The degree of the effective stiffness resulting from this behaviour is very crucial to the structural stability since very flexible connections induce large drifts into the system which in return amplify the P-delta effects. Considering that, connections in moment-resisting frames should be equipped with adequate rotational stiffness and capacity. The classification of connections basing on the rotational stiffness is provided in Eurocode 3 as follows and also depicted in Fig. (2-1) [21].

(a) Simple connection: permit the transfer of internal forces but unable to transfer bending moment.

(b) Semi-rigid connection: doesn't possess enough rigidity (stiffness) to qualify as a rigid connection hence connected members are allowed to slightly rotate. In other words, the rotation of connected members is significant enough to not be ignored while internal forces and moment are still transferred.

(c) Rigid connection: can transfer internal forces and moments without permitting the angles between connected members to change due to its high stiffness.

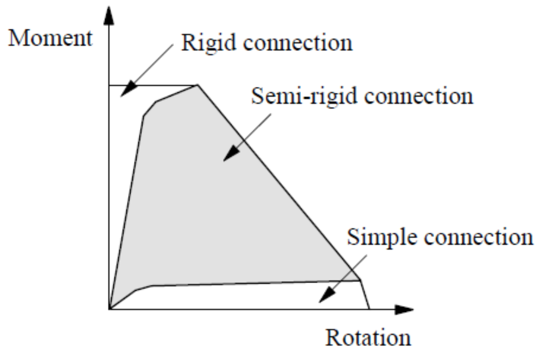

Figure 2-1. Schematic view of the moment-rotation relation for connections

Alternatively, the Eurocode 3 provide a quantitative way to define the type of connections by considering the initial rotational stiffness ($S_{\mathrm{j.\,ini}}$). In the thresholds given below, E is the steel modulus of elasticity, I_b is the beam's moment of inertia and L_b is the beam span:

(a) Rigid connection:

$$S_{\mathrm{j.\,ini}} \geq 8EI_{\mathrm{b}}/L_{\mathrm{b}} \qquad \text{for braced frame}$$

$$S_{\mathrm{j.\,ini}} \geq 25EI_{\mathrm{b}}/L_{\mathrm{b}} \qquad \text{for unbraced frame}$$

(b) Semi-rigid connection:

$$\frac{0.5EI_{\mathrm{b}}}{L_{\mathrm{b}}} < S_{\mathrm{j.\,ini}} \leq \frac{8EI_{\mathrm{b}}}{L_{\mathrm{b}}} \qquad \text{for braced frame}$$

$$\frac{0.5EI_{\mathrm{b}}}{L_{\mathrm{b}}} < S_{\mathrm{j.\,ini}} \leq \frac{25EI_{\mathrm{b}}}{L_{\mathrm{b}}} \qquad \text{for unbraced frame}$$

(c) Pinned connection:

$$S_{\mathrm{j.\,ini}} \leq 0.5EI_{\mathrm{b}}/L_{\mathrm{b}}$$

2.2 Description of CFS-RuC Semi-rigid Connection

The seismic design works on a basis of equipping the building structure with both vertical and lateral force-resisting systems that are suitable for withstanding the design ground motions through energy dissipation and high strength. One way of ensuring this is to assign moment-resisting connections to the system thus fulfilling the ductility requirement. Although many moment-resisting connections for cold-formed steel structures have been proposed in recent years, most of the studies to date have not been able to address the local buckling failure that prevails in thin elements of CFS sections. Therefore, the semi-rigid moment resisting connection adapted herein is set to at least delay the local buckling or even prohibit its formation through the restraining effect provided by the RuC infill. Besides, the RuC infill is a low-carbon material since it is made from recycled tyres rubber crumbs that replace normal aggregates in concrete.

To add to the details of the CFS-RuC connection provided already in the introduction chapter, the configuration shown in Fig. (2-2) is expected to dissipate seismic energy through the plastification of the connected double side-plates. Here, the effort is in attempting to establish connection parts that achieve the side plate plasticity (SPP) and prevent the anticipated critical limit state of shear in screws. Additionally, the flare groove weld lines present at the near and opposite column faces are expected to carry all the moments and shears transferred to the column through coupling forces of those weld lines [37].

In this study, semi-rigid connections featuring the bare CFS members and the ones infilled with RuC are simultaneously compared in order to examine the influence of the RuC infill on the connection behaviour. However, it is already recognized that standard concrete-filled steel (CFST) connections behave similar to their unfilled counterparts [40] besides these few differences resulting from the concrete-filling: increased stiffness, ductility and strength which can also affect the failure modes. Bearing this in mind, such differences are expected to be observed in the behaviour of CFS-RuC connections from the finite element analysis. Proposed finite element models are developed and subjected to monotonic and gravity loading until failure. The effects of side plate thickness, screws configuration, member thickness and the axial compression ratio are studied to understand how they affect the connection performance. Furthermore, as a supplement to the previously conducted research by Alireza et al [17], within this study the effect of different member dimensions on the connection behaviour are investigated.

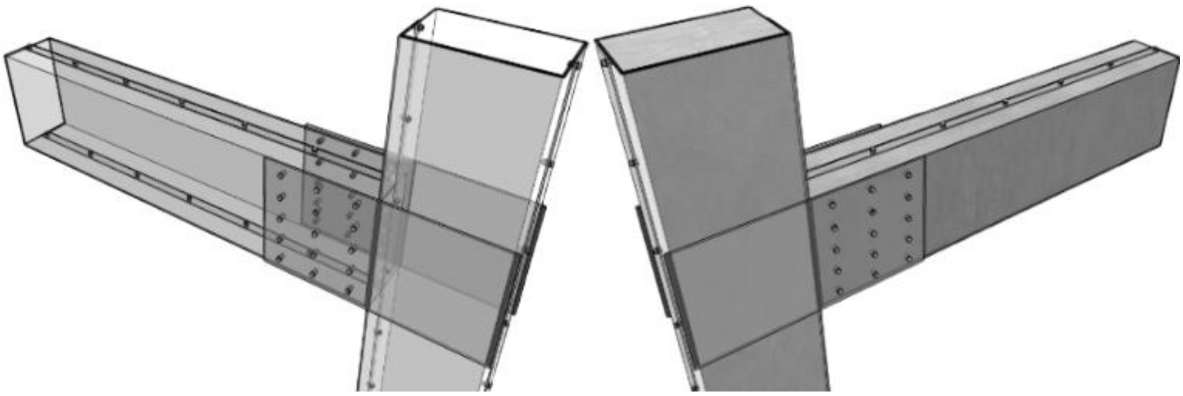

Figure 2-2. Schematic view of the bare and composite connections of the CFS-RuC system.

2.3 Simulation of CFS-RuC Connection in ABAQUS

Finite element analysis employs the finite element method (FEM) to solve complex problems of elasticity in engineering. The concept behind this popular method is that the burden of solving complicated differential equations is removed by simplifying a large system into smaller basic parts in the process called meshing. Eventually, this process results in a system of algebraic equations which is much easier to solve. To accurately assess the actual behaviour of the CFS-RuC semi-rigid connection, implementation of the FEM is required therefore ABAQUS software, which is a prelevant nonlinear finite element analysis software is used to conduct the numerical study.

2.3.1 Finite Element Modelling

As it was previously mentioned, the finite element study delivered in this part was conducted based on the numerical ABAQUS model adapted from the earlier study of Alireza et al [37]. The only primarily difference within this study is that new members with different dimensions are developed in order to expand the library of CFS-RuC semi-rigid connections featuring a variety of member sizes. The FE model properties and assumptions made from the earlier study are maintained, hence they are not covered herein. However, for clarity purpose, a summary of the FE modeling process is presented below.

The CFS C-channel profiles and side plates were modeled using S4R shell element with a mesh of 20 mm x 20 mm. This four-noded shell element has six translational and rotational degrees of freedom per node and reduced integration. For the rubberized concrete, C3D8R deformable solid element with a mesh of 50 x 50 mm was chosen. Geometric nonlinearity was considered to account for any nonlinearity that can results from the second-order effects. Point-based cartesian fasteners were selected to represent the self-drilling screws for the beam-to-side plate screwed connections and for the overlapped beam and column built-up C-sections. Fig. (2-3) shows the load-deformation backbone curve for the #12 steel-to-steel connection and it was utilised to derive the elasticity and plasticity behaviors that were assigned to the cartesian fasteners. Using the elastic-plastic material behaviour provided in ABAQUS, a bilinear stress-strain curve is simulated for all steel components. The first elastic part of the multilinear curve presents the measured modulus of elasticity with a magnitude of E_s= 203500 MPa and poisson's ratio of q_s= 0.33.

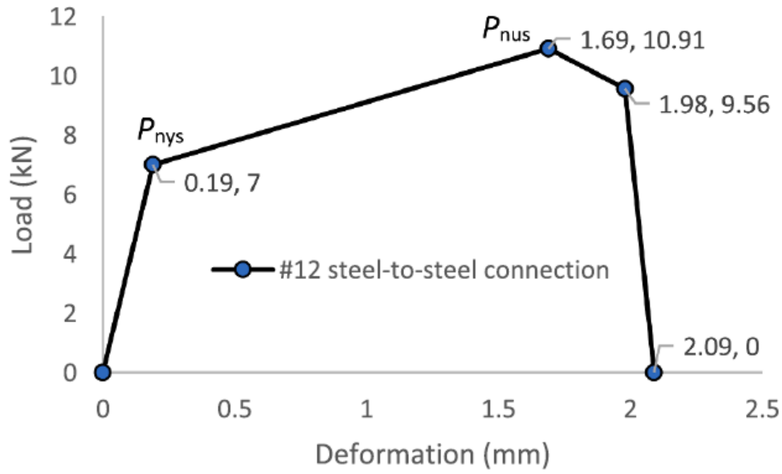

Figure 2-3. Load-deformation backbone curve for #12 steel-to-steel connection [37]

The tangent moduli representing the second modulus is expressed as $E / E_s = 0.01$. Regarding the RuC infill, the mechanical properties were derived from R40-S3 specimen presented in [16], having a rubber content of 40% replacement ratio, elastic modulus of E_{RuC} = 14.6 GPa and compressive strength of F_{RuC}= 21MPa. A nonlinear static analysis is selected for this model. A controlled displacement is monotonically applied at the beam end until failure, while gravity loading is applied at the top of the column. In terms of the interactions between components, interface elements are used to model the contact between the rubberized concrete and steel sections. The tangential behavior with friction coefficient of 0.2 and normal hard contact are also defined. As surface-to-surface contact is usually used for modeling full transfer of the load from one element to another, it is implemented to define interactions between the non-screwed or non-welded parts of the connections. Coupling constraints are selected to define the displacement loading and boundary conditions at the section ends using corresponding reference points, shown in Fig. (2-4). Two reference points on the column ends, RP-1 and RP-2 are made to restrain the translation in Z-direction but released at the RP-3 reference point of the beam-end, while free rotation is allowed about X-direction at all three reference points and restrained in other rotational directions (Y,Z) of the same reference points.

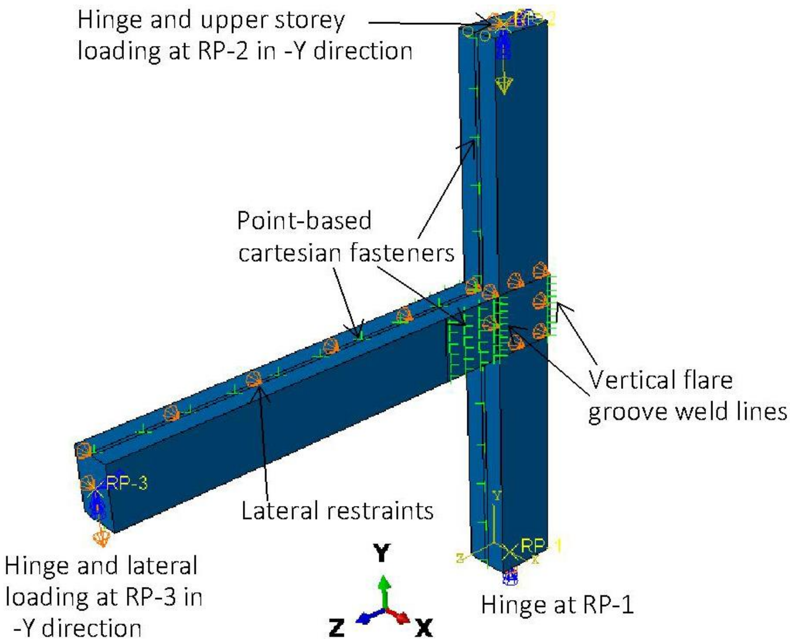

Figure 2-4. Overall view for composite CFS-RuC connection FE model

2.3.2 Discussion of FE Results

Table (2-1) reports the key outputs of the numerical modeling for CFS-RuC connections subjected to bending moment. From Table (2-1), connection configurations are labeled with abbreviations that start with CFS-RuC, meaning a composite connection with RuC infill whereas those starting with CFS are connections employing a bare beam and column. Then, beam and column thicknesses (3, 4, 5 or 6 mm) are written respectively, followed by side plate thicknesses (SP4, 6, or 8 mm) and the number of screw connection arrays (#24, 36 or 42). At the end, corresponding gravity loading (460, 780, 1000 kN) considered in the connection design are added. For example, CFSRuC3-4-SP4#24-460 stands for a CFS-RuC connection with a CFS beam thickness of 3 mm and a CFS column thickness of 4mm, using a side plate thickness of 4mm with 24 screws and

460 kN of gravity loading applied at top of the column. The limits states USS, YSS, BLB and SPP respectively denote ultimate screw shear, yielding screw shear, beam local buckling and side plate plasticity. Moreover, the new overall member sizes introduced in this specific study are a 195x350 and 250x350 sections which are larger than the 175x300 section adopted in the earlier work by Alireza et al. [17]. The purpose for this is to enrich the library of sections that can be used in the case study building design to be done later and it is anticipated that moment-frames require deep sections since they accommodate large moments. While numerical results of all sections are presented in Table 2-1, only those that incorporate the 195x350 sections are discussed in this part. Further FE results of the 250x350 ones are presented in the appendix A and B.

Presented in Fig. (2-5) are the moment-rotation (M-θ) response of the CFSRuC3-4-SP4#36 configuration compared with that of the CFS3-4-SP4#36. For deciding the failure mode of the configurations, the corresponding screw force results (Ps/Pnys-θ) for both the bare and composite configuration are presented too. Here, the nominal bending moment of 3 mm thickness beam, Mn and screw yield force, Pnys values respectively equal to 79.5 kNm and 7 kN. Also, the M in the expression M/Mn is the bending moment obtained from the connection end, while the rotation, θ is determined as the rotation of connection elements calculated at the connection centroid.

Table 2-1. Results of the bare and composite connections (units for section dimensions in mm)

Label	Section dimension (widthxdepth)	M_{Peak}/M_n	θ_{Peak} (mrad)	θ_y (mrad)	θ_u (mrad)	$\mu = \theta_u/\theta_y$	Failure
CFS3-4-SP4#24	195x350	0.83	19.31	7.22	30.55	4.23	USS-SPP
	175x300	0.74	18	4.61	33	7.18	USS-SPP
CFSRuC3-4-SP4#24	195x350	1.00	23.64	7.56	86.24	11.40	SPP
	175x300	0.79	24.00	5.00	29	5.80	USS-SPP
CFSRuC3-4-SP6#24	195x350	1.44	29.24	8.13	31.37	3.86	USS
	175x300	0.83	17.00	4.62	21	4.55	USS
CFS3-4-SP4#36	195x350	0.84	12.83	8.00	30.56	3.82	SPP-BLB
	175x300	0.76	15.00	5.18	36.00	6.95	SPP
CFSRuC3-4-SP4#36	195x350	1.00	30.03	7.42	88.09	11.87	SPP
	175x300	0.79	16.00	5.54	62	11.19	SPP
CFS3-4-SP6#36	195x350	1.14	19.28	9.76	26.86	2.75	USS-BLB
	175x300	1.11	23.00	4.92	27	5.49	USS-SPP-BLB
CFSRuC3-4-SP6#36	195x350	1.47	32.66	8.56	53.86	6.29	USS-SPP
	175x300	1.14	21.00	4.55	27	5.93	USS-SPP
CFSRuC3-4-SP8#36	195x350	1.96	37.52	10.15	39.12	3.85	USS
	175x300	1.08	15.00	4.53	24	5.29	USS
CFSRuC3-4-SP6#42	195x350	1.64	38.62	8.98	61.33	6.83	USS-SPP
	175x300	1.24	29.00	4.53	53	11.70	USS-SPP
CFSRuC3-4-SP8#42	195x350	2.03	42.30	11.17	80.08	7.17	USS-SPP
	175x300	1.25	17.00	4.50	26	5.78	USS
CFSRuC4-6-SP4#24	250x350	0.60	35.47	6.91	70	10.13	SPP
CFSRuC4-6-SP6#24	250x350	0.90	28.05	7.65	30.34	3.97	USS
CFS4-6-SP4#36	250x350	0.70	19.18	9.49	30.56	3.22	BLB
CFSRuC4-6-SP4#36	250x350	0.63	31.69	6.95	79.4	11.42	SPP
CFSRuC4-6-SP6#36	250x350	1.00	29.31	7.99	50.8	6.36	USS-SPP

It can be clearly seen that the composite connection (CFSRuC3-4-SP4#36) successfully attained its nominal flexural moment capacity (it touches the unity dashed line). This can be attributed to its failure mode of SPP which allows uniform distribution of the applied load through the plastification of the side plate (see Fig. (2-6)). On the other hand, the bare connection experienced a BLB failure as indicated by the Ps/Pnys-θ curve where screw shear forces reach the yielding limit (i.e Ps/Pnys=1) but they have not achieved their ultimate force of 10.91kN. The local buckling occurred around Mpeak/Mn= 0.84 which shows that the bare nominal moment capacity is not attained as predicted by the Direct Strength Method (DSM). It is later shown in Fig. (2-6) that this is due to the yielding of the connection at the column side which can be associated to the small thickness (4mm) of the side plate. Contrarily, for the same bare connection but with a side plate of 6 mm thickness, the BLB limit state was also observed at around Mpeak/Mn= 1.14 which agrees with the DSM prediction (see Fig. (2-7)).

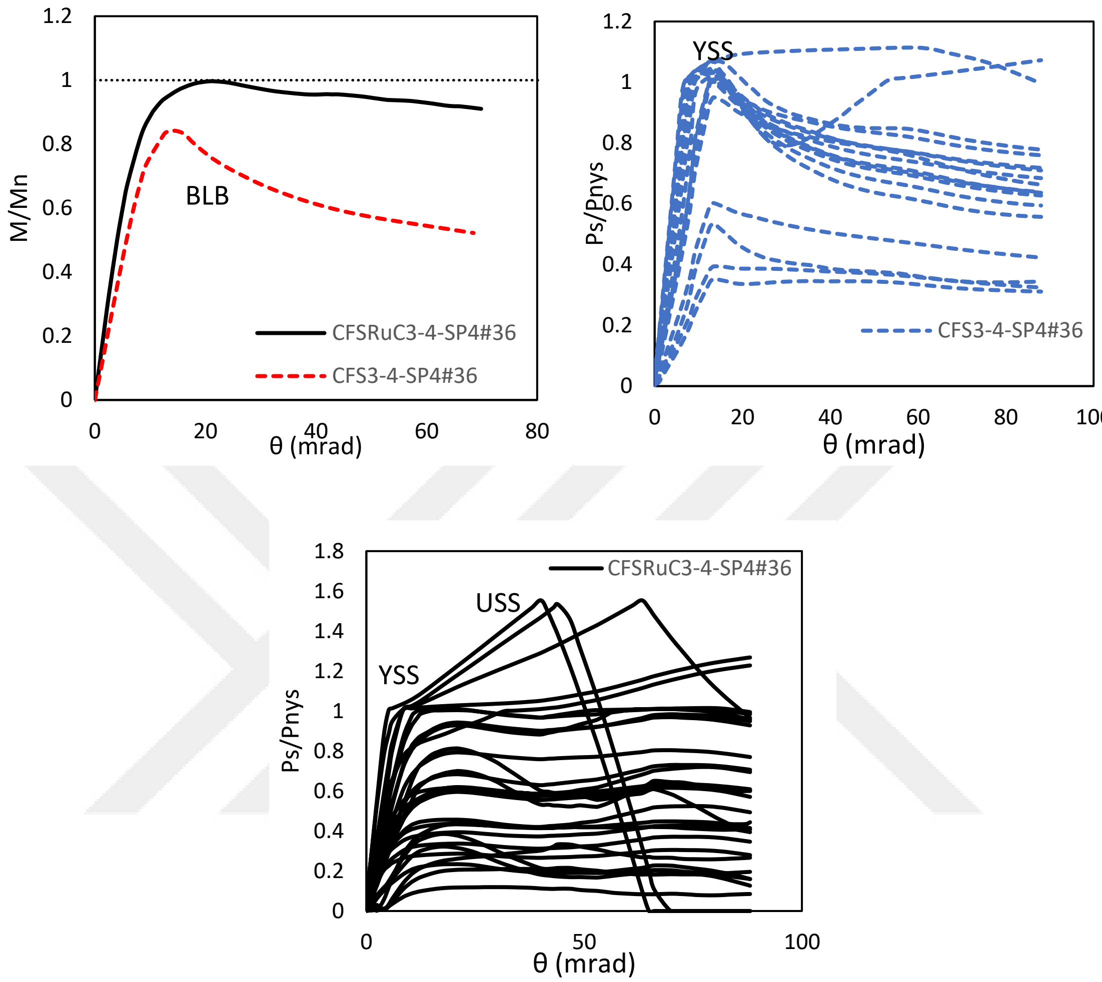

Figure 2-5. Normalized M/Mn- θ and Ps/Pnys- θ curves for the bare and composite connections

Alternatively, as illustrated in Fig.(2-6), the connection response can be shown by the Von-Mises contours at both Mpeak and those at the ultimate rotation. Here areas in the plastic region (with stress exceeding 275 MPa) are symbolized with grey colour.

Notice that the level of stress observed at Mpeak for the composite connection are confined only in the side plates which is still also the case at the ultimate rotation. However, for the bare connection, the stress at Mpeak is shown to have started propagating towards the column side and finally at the ultimate rotation, the resulting local buckling of both beam and column is observed in Fig.(2-6).

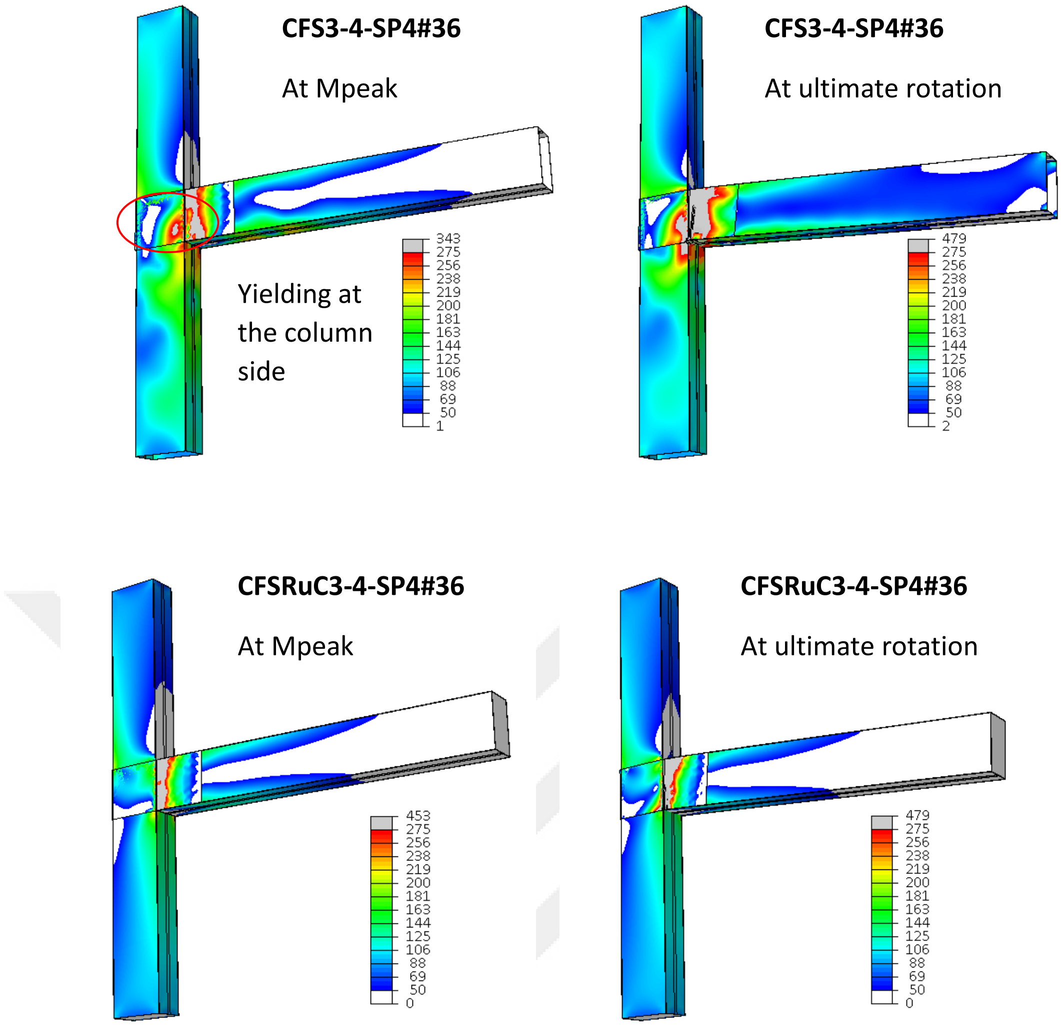

Figure 2-6. Von-Mises stress contours at Mpeak (left) and at the ultimate rotation (right) (units: MPa)

Here again, the role of the RuC infill in removing the unwanted limit state (BLB) and improving the stiffness of the composite connection can be highlighted from the good moment-rotation response that resulted into a high ductility factor of $\mu = 11.87$ whereas its bare counterpart only delivered a low ductility of μ =3.82. The factor, $\mu = \theta u/\theta y$ is used as an indication of ductility.

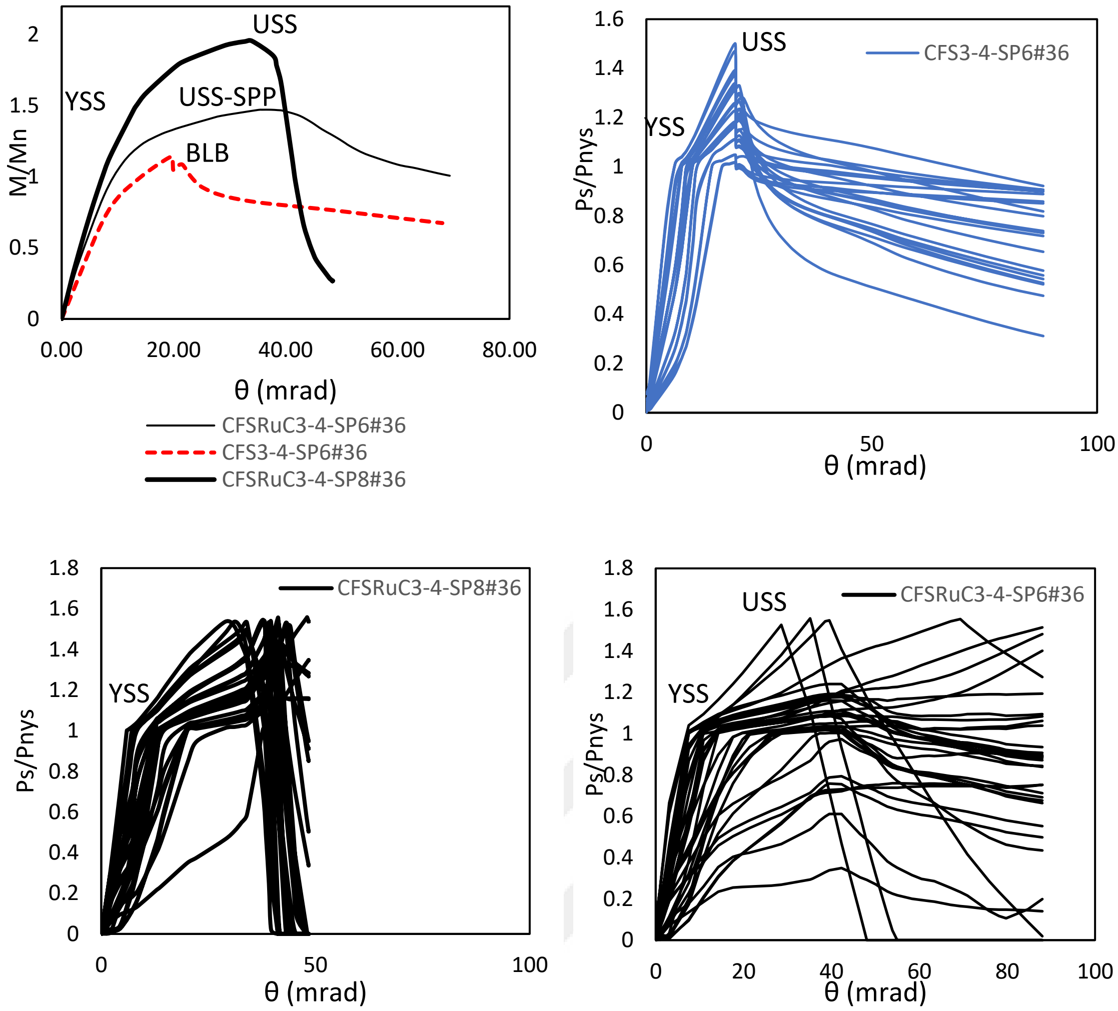

Figure 2-7. Normalized M/Mn- θ and Ps/Pnys- θ curves of bare and composite configuration

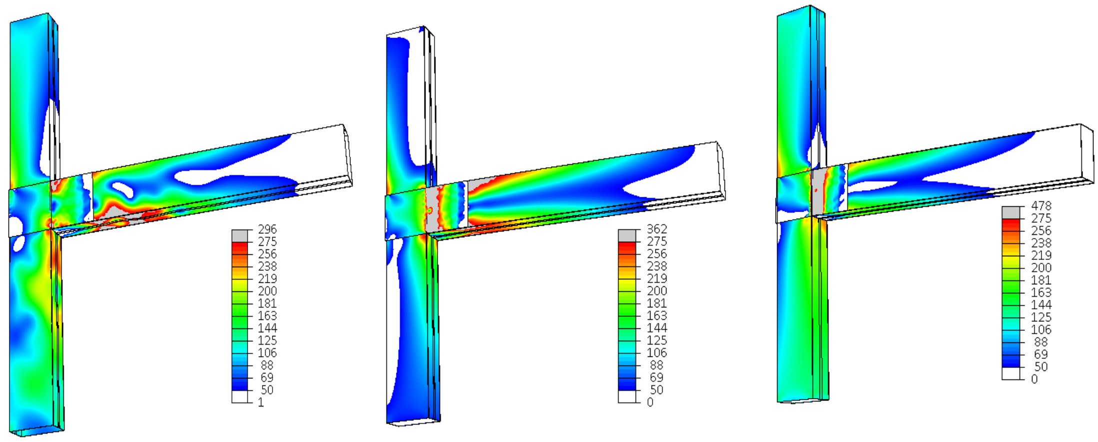

Figure 2-8. Von-Mises stress contours of the CFS3-4-SP6#36, CFSRuC3-4-SP6#36 and CFSRuC3-4-SP8#36 connection configurations (left to right).

Here θy is taken as the rotation at which the screw yielding capacity is reached and θu is accepted as the ultimate rotation calculated when the Mpeak reduce to 80%. Table (2-1) contains all the values of the yield, ultimate rotations and ductility factor obtained for all the connection models. To assess the effect of changing the side plate thickness from 6 to 8mm for the CFSRuC3-4-SP6#36 connection, comparisons are made in Fig. (2-7) between the response from the moment-rotation curves along with their corresponding P/Pnys-θ curves and the stress distribution of von-mises contours.

First, it is noticed that the BLB limit state happened in the bare connection with side plates of 6mm thickness as displayed in Fig.(2-8). This led to a reduced ductility factor of $\mu =$ 2.75. But this time, unlike in the case of the CFS3-4-SP4#36 bare connection where the rigidity of the connection was low hence influencing the occurrence of the local buckling at the column side, here the side plate thickness is 6mm (i.e stiff) that is the reason why the BLB failure is now observed at the beam bottom as expected. Increasing the thickness of the side plate from 6 to 8 mm resulted in an increased Mpeak/Mn of 1.96 at a rotation of $\theta peak$= 37 mrad. Consequently, the controlling limit state predominantly transitioned from USS-SPP to USS, attaining an ultimate rotation of 39 mrad which gives a small ductility factor of $\mu = 3.82$. Besides, the composite connection with a thick side plate of 8mm thickness results into an increased stiffness to the extent that the beam part at the connection end yields (see Fig. (2-8)). This is not a desirable case. Connection configurations should be arranged so that the energy dissipation is done through the plastification of side plates.

2.4 Plastic Hinge Model For CFS-RuC Connections

The finite element (FE) results obtained in the above section provide a basis for justifying the practicality of the infill RuC in eliminating unwanted limit states and improving the moment-rotation response. However, finite element analyses require too much computation effort and hence are not practical to perform frame-level analyses. A plastic hinge model is therefore to be developed through a validation study utilising the corresponding FE results to come up with an applicable modeling protocol that can be used in the frame-level analysis.

A shell type FE model using ABAQUS developed in the numerical study and a corresponding beam type model using SAP2000 developed in this study are shown in Fig. (2-4) and Fig. (2-9), respectively. The models represent a one-way cantilever connection component delineated between the inflection points of a 4 m span moment-frame under unity displacement-controlled loading. In the SAP2000 model (Fig. 2-9), the beam and column composite sections are modeled in the section designer by assuming the unconfined concrete model for the RuC infill. Frame elements are used to model the beams and columns. A hinge model composed of a plastic and an elastic spring element incorporating total moment (M)-rotation(θ) response for the connection is modeled at the beam-column ends using M- θ curve data extracted from the accompanying connection FE results. Both the hinge and elastic spring are assigned with an offset at the end of the connection element, which provides a close estimate of the pushover results as the one from the shell type model for Abaqus. The boundary conditions and gravity loading specifications are set to be the same as of the shell type model.

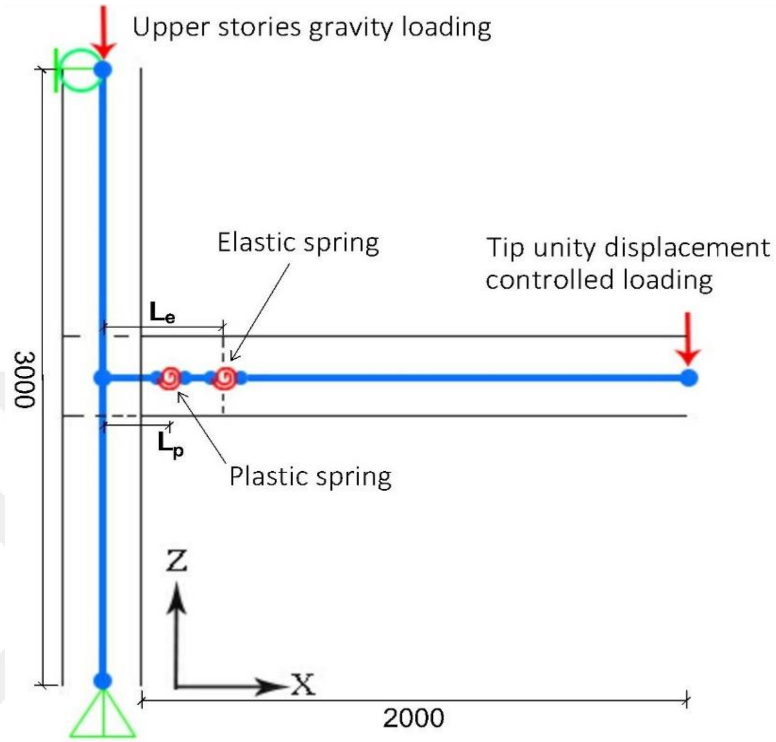

Figure 2-9. Modeling details of a beam model in SAP2000 (units in m)

For a composite CFS-RuC connection (CFSRuC3-4-SP6#36-300), Fig. 2-10a illustrates the moment-rotation (M-θ) curve (dashed line) obtained from the Abaqus results. The linear line (solid line) represents the slope of the elastic portion of the M-θ curve, from which the stiffness of the elastic spring element is deduced and assigned at the beam-end in the SAP2000 model. Further, the remaining portion of the curve (solid line with a star marker) represents plastic rotation data interpolated from M-θ curve to be assigned as a 'plastic' hinge at the beam-end in the SAP2000 model. These properties are very essential for proper definition of the new CFS-RuC system's semi-rigid connection. The hinge overwrite property is assigned in the SAP2000 program to ensure accurate results.

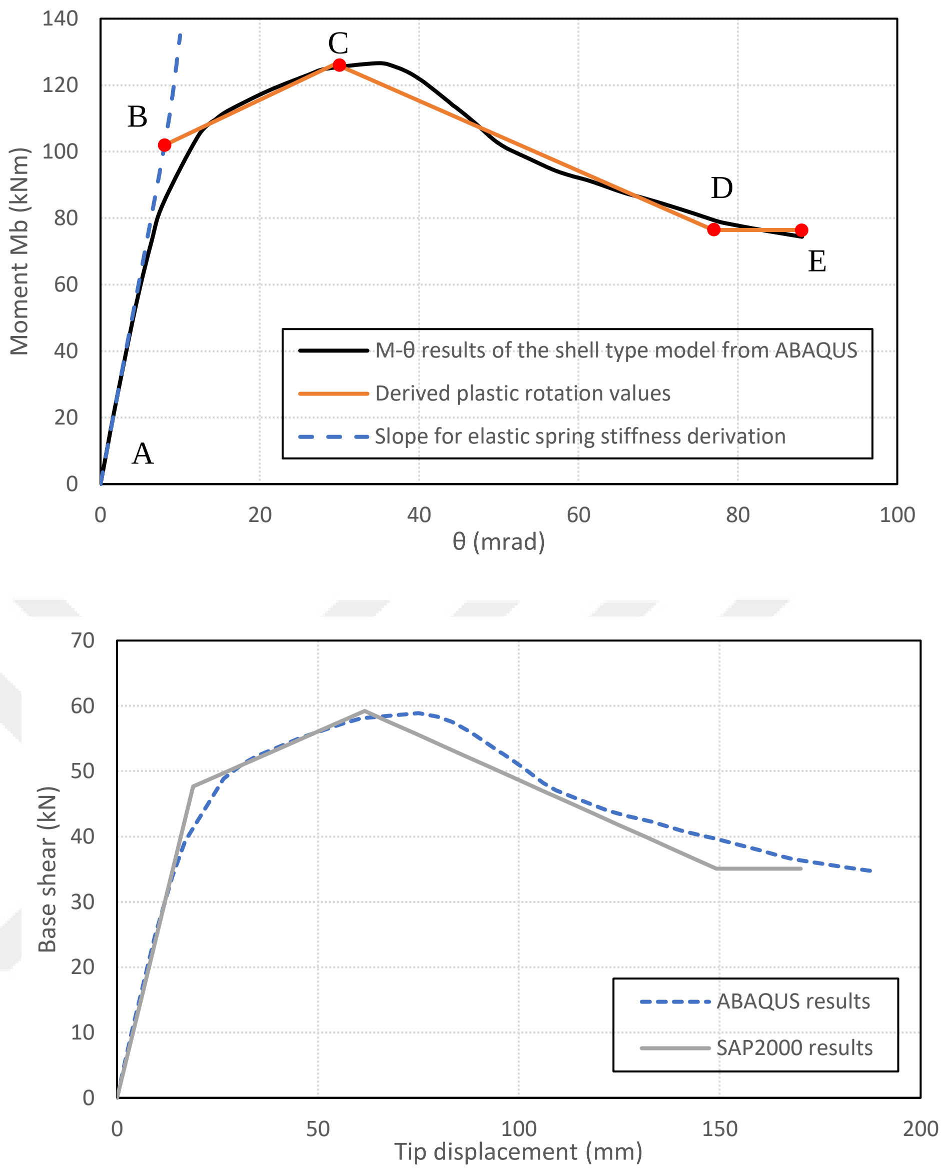

Figure 2-10. For the representative connection configuration CFSRuC3-4-SP6#36-300: (a) elastic spring and moment-rotation curves used in the hinge (top), and (b) pushover results (bottom)

For the same connection, Fig. (2-10b) displays pushover curve results from SAP2000 compared with the corresponding force-displacement curve from ABAQUS results. Matching pushover results as displayed in Fig. (2-10b) are achieved through modifying program parameters such as plastic and elastic spring locations and recording how each property affects the results. Eventually, all optimum modeling properties that ensure close results when compared to Abaqus results for connection configurations featuring 175x300 sections are obtained as reported in Table 2-2 (in terms of elastic stiffness, spring's location from the beam-column joint, and five points A, B, C, D, and E to define moment-rotation behaviour), thus concluding the validation study for the development of a hinge-model. Following the results in the Section, plastic hinge properties of other sections with different dimensions can be derived.

Table 2-2. Plastic hinge and elastic spring assignments to beam-column joints

	Connection Label	Elastic spring stiffness (KNm/rad)	Elastic spring location (m)	Plastic hinge location (m)	Parameters for plastic hinges									
					A		B		C		D		E	
					M/Mn	θ	M/Mn	θ	M/Mn	θ	M/Mn	θ	M/Mn	θ
Based on the 175x300 sections	CFSRuC2-4-SP4#15-60	5643	0.2	0.4	0	0	0.77	0	1.10	0.0073	1.10	0.0117	0.64	0.02
	CFSRuC2-4-SP4#15-300	5643	0.2	0.4	0	0	0.77	0	1.10	0.0073	1.10	0.0119	0.38	0.02
	CFSRuC2-4-SP4#15-600	6250	0.2	0.45	0	0	0.80	0	1.16	0.0089	1.16	0.0103	0.79	0.02
	CFSRuC2-4-SP4#24-60	6610	0.25	0.45	0	0	1.16	0	1.67	0.0109	1.67	0.0216	0.82	0.04
	CFSRuC2-4-SP4#24-300	6082	0.4	0.45	0	0	1.09	0	1.54	0.0114	1.54	0.0209	0.63	0.04
	CFSRuC2-4-SP4#24-600	6610	0.25	0.45	0	0	1.24	0	1.70	0.0125	1.67	0.0217	1.03	0.03
	CFSRuC2-4-SP6#24-60	7000	0.25	0.5	0	0	1.23	0	1.70	0.0085	1.45	0.0150	0.55	0.02
	CFSRuC2-4-SP6#24-300	7500	0.25	0.5	0	0	1.22	0	1.71	0.0098	1.66	0.0133	1.10	0.02
	CFSRuC2-4-SP6#24-600	6981	0.25	0.45	0	0	0.75	0	1.12	0.0097	1.09	0.0128	0.69	0.02
	CFSRuC3-4-SP4#24-300	7773	0.25	0.4	0	0	1.25	0	1.66	0.0130	1.66	0.0203	0.16	0.04
	CFSRuC3-4-SP6#24-300	7885	0.25	0.45	0	0	1.24	0	1.75	0.0083	1.75	0.0107	0.12	0.03
	CFSRuC3-4-SP6#36-300	8714	0.25	0.45	0	0	0.95	0	1.25	0.0118	1.09	0.0184	0.19	0.03
	CFSRuC3-4-SP8#36-300	9000	0.25	0.45	0	0	0.87	0	1.16	0.0067	0.88	0.0181	0.23	0.03
	CFSRuC3-4-SP6#42-300	9000	0.25	0.45	0	0	1.00	0	1.35	0.0154	1.35	0.0284	1.06	0.04
	CFSRuC3-4-SP8#42-300	9560	0.25	0.45	0	0	1.02	0	1.36	0.0077	1.34	0.0148	0.17	0.03

CHAPTER III

DESIGN OF CFS-RUC STRUCTURES

3.1 Introduction

This section briefly describes the modeling and design of the 2-,5-, and 8-story CFS-RuC building frame structures according to provisions of the 2018 Turkish Seismic Code [38]. In general, detailed calculations and analysis results provided in this part are made for the 8-story CFS-RuC building only. Corresponding results for the 2-story and 5-story CFS-RuC buildings are presented in tables where it is relevant for comparison purposes.

3.2 Structural and Load Modeling for the Case Study Buildings

The representative buildings selected here are assumed to be residential and located in a region with high seismicity in Bayrampaşa, a suburb of Istanbul on the European side of the Bosphorus. Three typical structures, namely 2-story, 5-story, and 8-story building systems, were selected to represent the current building stock of Bayrampaşa, mainly consisting of low and mid-rise residential RC buildings. In plan, all structures' footprint is 20m x 20m, with an identical story height of 3.2m for all frame structures. Fig. 3-1 presents the 3D models of structures considered herein. Even though secondary conventional steel beams are included in the 3D models of our frame structures for the purpose of conducting a realistic design i.e., providing a restraining effect to the beams, the focus here is only on the design of composite cold-formed steel rubberised concrete (CFS-RuC) beams and columns.

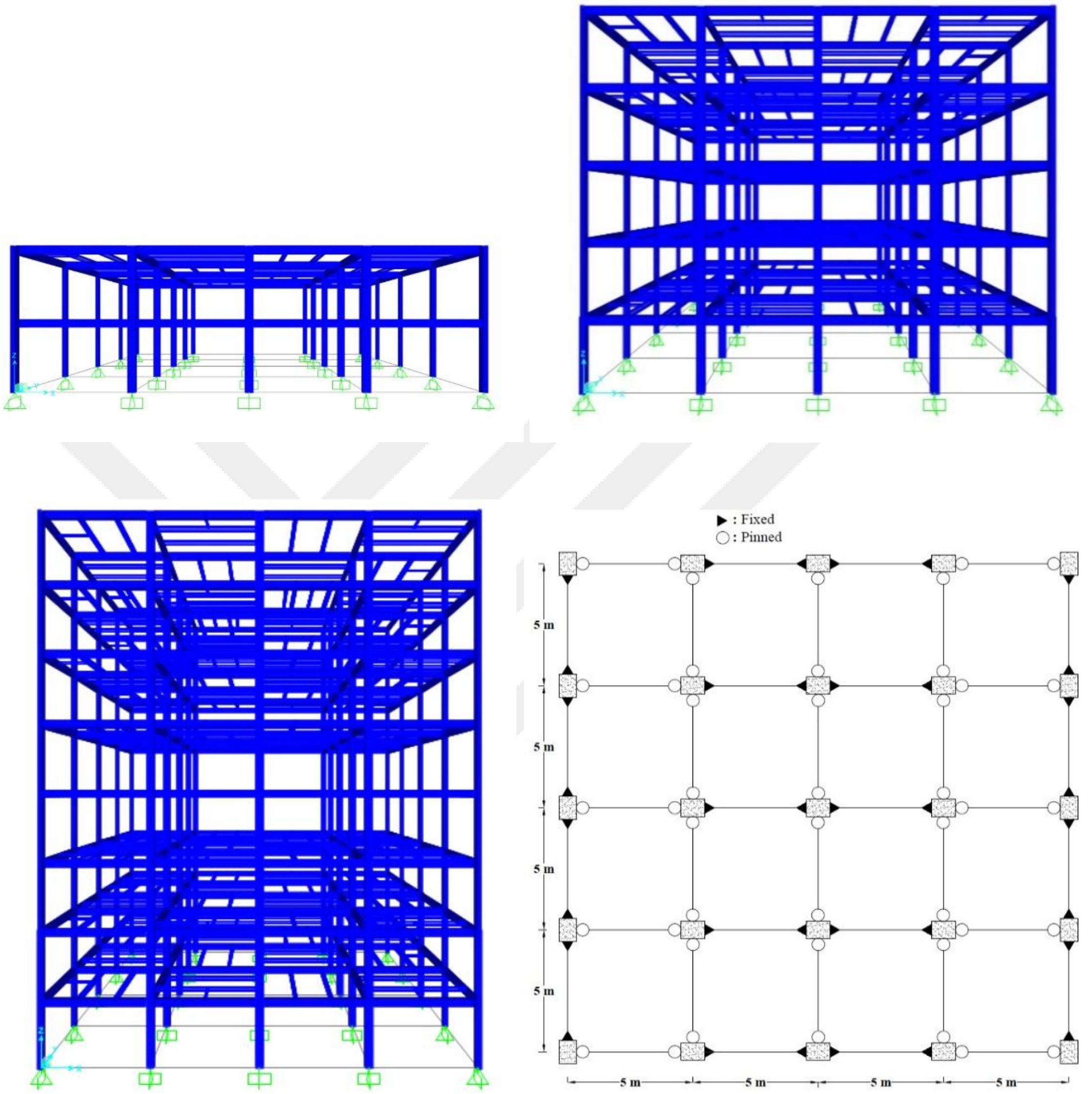

Figure 3-1. Building models of the 2-, 5- and 8-story building

Given that this composite system is newly introduced, to avoid the complexity of bracing systems and the lack of appropriate design parameters such as the response factor R for the CFS-RuC system, all X- and Y-direction lateral load bearing systems of all building structures are assumed to be moment-resisting frames. The dimensioning of composite CFS-RuC columns and beams of the load-bearing system is done by developing first the sections in CUFSM tool [47] , where the finite strip analysis is carried out and load factor are obtained together with their buckling modes and eventuallly estimation of their actual capacities using the Direct Strength Method (DSM) is carried out.

3.2.1 Material Specifications

As presented in Table 2.1A of the Turkish Code for Steel Construction (TCSC2016), the properties of the S275 structural steel have been adopted for the build-up channel sections. Regarding the RuC infill, the mechanical properties were derived from R40-S3 specimen presented in [16], having a rubber content of 40% replacement ratio, elastic modulus of E_{ruc}= 14.6 GPA and compressive strength of F_{ruc}= 21Mpa. The resulting stress-strain curves for both S275 and RuC infill are shown in Fig. 3-2.

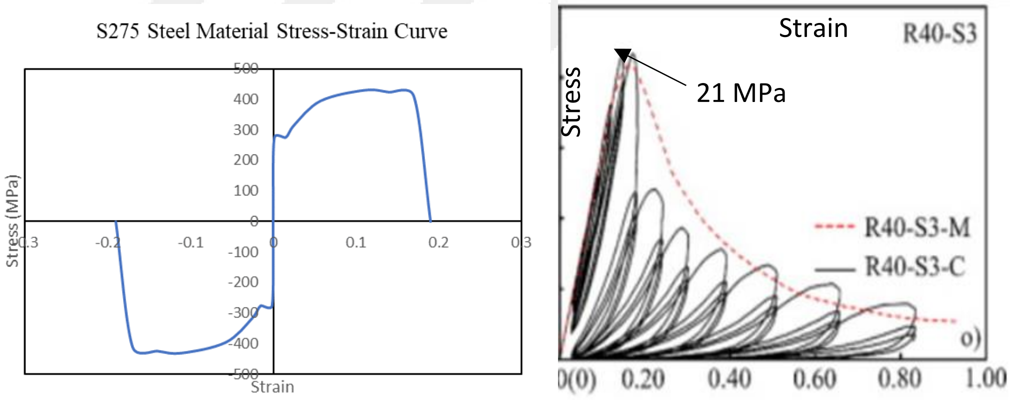

Figure 3-2. Stress-strain curve for steel (left) and rubberised concrete materials [17] (right)

3.2.2 Loads Considered for the Case Studies

In this section, all types of loads that are anticipated to act on the case study buildings are estimated. Among those include dead, live, snow, wind and earthquake loads. However, in most cases especially in this specific study where the building height is not significant, earthquake loads induce larger lateral forces into the system in comparison to wind loads. Hence wind loads will be ignored in this work.

3.2.3 Dead and Live Loads

Estimated gravity loads that act on the building floors are given below. CFS-RuC columns and beams have custom sections and consequently, this complicates the self-weight estimation of these members, therefore their self-weight are calculated automatically by the analysis software by considering their weights in the load combinations.

Roof floor level	:	flooring		0.5 kN/m^2
		insulation		0.4 kN/m^2
		corrugated steel deck sheet + RC slab		2.1 kN/m^2
		ceiling + utilities		0.5 kN/m^2
		steel construction (secondary beams)		0.2 kN/m^2
		total dead loads	G	= 3.7 kN/m^2
		live loads	Q_r	= 2.0 kN/m^2
		snow loads	S	= 1.3 kN/m^2
		parapet	G_d	= 2.0 kN/m

The snow loads estimated here are based on the meteorological data about Istanbul. The general maximum snow level is approximately 75 cm. Therefore, assuming the uniform distribution of the snow load, 2 kN/m^3 unit weight of the snow from TS EN 1991-1-3 [41] gives approximately 1.3 kN/m^2 as shown above. It is also assumed that the dead and live loads at the stairs and elevator area are equal to the dead and live loads in other areas of the floor.

Normal floor level	:	flooring		0.5 kN/m^2
		corrugated steel deck sheet + RC slab		2.1 kN/m^2
		ceiling + utilities		0.5 kN/m^2
		partition walls		1.0 kN/m^2
		steel construction (secondary beams)		0.2 kN/m^2
		total dead loads	G	= 4.3 kN/m^2
		live loads	Q	= 2.0 kN/m^2
		perimeter walls	G_d	= 3.0 kN/m

3.2.4 Earthquake Loads

In this part, relevant sections of the current Turkish Seismic Code (TSC 2018) that apply to the seismic design of CFS-RuC structures are briefly discussed.

Soil Properties

According to the nature of the soil profile at the location of the case study buildings, which is Bayrampaşa district (Istanbul), an appropriate soil class is assumed to continue with earthquake load calculations. For this particular region, it is witnessed from the Istanbul soil classification map [42] that sites with both ZB and ZC soil properties are the majority. Therefore, a moderate ZB soil class is assumed within this study for defining seismic design parameters. ZB is defined as a less weathered, rocky soil.

Earthquake Ground Motion Level

As per TSC 2018 Section 2.2.2 [38], the DD-2 standard design earthquake ground motion level is recommended for the case study CFS-RuC buildings (residential buildings). The DD-2 ground motion level can be interpreted as a ground motion that has a 10% probability of exceedance in 50 years, i.e return period of 475 years.

Building Occupancy Category (BOC) and Importance Factor (I)

The representative buildings are chosen to be residential, therefore according TBEC 2018 Table 3.1, the building occupancy category is determined to be BOC = 3 and the corresponding importance factor I = 1.

Seismic Design Category (SDC)

The AFAD interactive website (https://tdth.afad.gov.tr) is used to extract site-specific seismic ground motion values of the case study buildings in Bayrampaşa. The site class of ZB and DD-2 standard earthquake ground motion level are chosen with the purpose of determining the seismic design category. Fig. 3-3 illustrates ground motion values and horizontal design spectrum parameters obtained from the AFAD website.

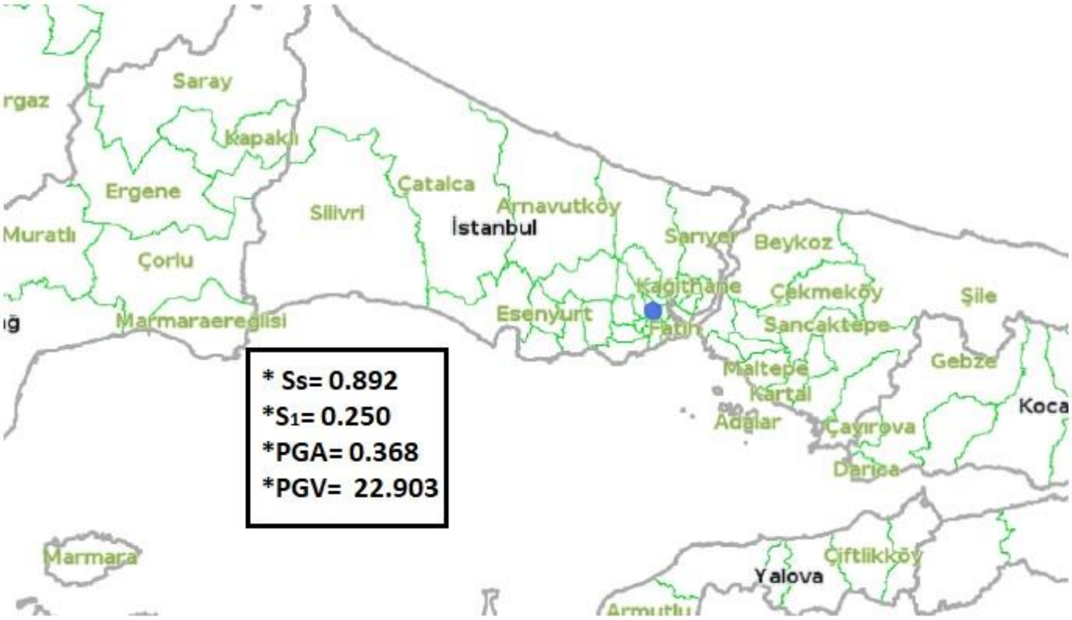

Figure 3-3. Horizontal elastic spectrum parameters obtained for Bayrampaşa

The AFAD website provides the values for the mapped spectral acceleration at short periods, S_s = 0.892, and the mapped spectral acceleration at a period of 1s, S_1 = 0.250, which imply from Table 2-1 and 2-2 of TBEC2018 that the site coefficients are F_s = 0.9 and F_1 = 0.8. Therefore, design base spectral acceleration parameters S_{DS} and S_{D1} can be calculated using the Equations (3-1) and (3-2) as shown below.

$$S_{DS} = S_S F_S = (0.892)(0.9) = 0.803 \tag{3-1}$$

$$S_{D1} = S_1 F_1 = (0.25)(0.8) = 0.2 \tag{3-2}$$

Finally, based on the building occupancy category being, BOC = 3 and the determined design spectral acceleration parameter at short period being, S_{DS}= 0.803, the seismic design category is selected as SDC = 1 since it satisfies the criteria S_{DS} > 0.75 of the TSC 2018 Table 3.2.

All parts of the horizontal elastic spectrum have corresponding formulas to define the spectral values as indicated in Section 2.3.4 of TSC 2018. First, T_A and T_B values are calculated, and then by replacing S_{D1}, T_A, T_B, S_{DS}, and T_L values into Equations (3-3) and (3-4), the horizontal elastic spectrum S_{ae} is obtained as displayed in Fig. (3-4). Here S_{D1}, T_A, T_B, S_{DS}, and T_L respectively denote design spectral response acceleration parameter for a period of 1 second, horizontal elastic design acceleration spectrum corner periods A,B, design earthquake spectral response acceleration parameter at short periods and transition period to constant displacement region in the horizontal elastic design spectrum.

$T_A = 0.05s \qquad T_B = 0.249s \qquad T_L = 6s$

$$S_{ae}(T) = \left(0.4 + 0.6\frac{T}{T_A}\right)S_{DS} \quad (0 \leq T \leq T_A); \;\; S_{ae}(T) = S_{DS} \quad (T_A \leq T \leq T_B) \qquad (3\text{-}3)$$

$$S_{ae}(T) = \frac{S_{D1}}{T} \quad (T_B \leq T \leq T_L); \qquad S_{ae}(T) = \frac{S_{D1}T_L}{T^2} \qquad (T_L \leq T) \qquad (3\text{-}4)$$

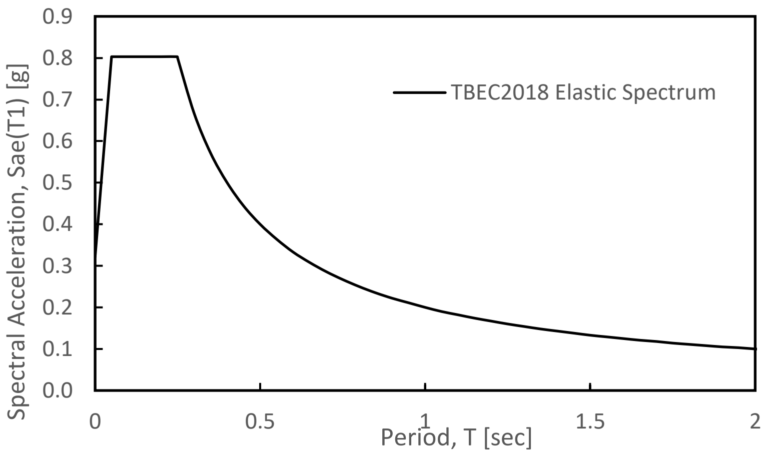

Figure 3-4. Horizontal elastic spectrum

Building Height Class (BHC)

For regular buildings as in the case studies, the building height H_N is the measured height from the base level, which is H_N= 3.2x8 = 25.6 m for the 8-story building. In this instance, according to TSC 2018 Table 3.3, for a building with SDC = 1 and falling in the range 17.5m < H_N = 25.6m < 28m, the building height class of this particular building is set to be BHC = 5.

Building Performance Level (BPL) and analysis approach

According to Table 3-1 shown below, a building to be designed with seismic design category SDC = 1 and a standard earthquake ground motion level DD-2 is prescribed to meet the normal performance level of controlled damage (CD) i.e., life safety (LS), and the evaluation/design approach advised to follow is the strength design method. Controlled damage performance level is defined as the level at which certain damages in the structural elements are allowable, but all damages should be restricted to this level and life safety should be guaranteed. The basis of the strength design method is to allocate structural members such that the factored loads applied on members do not exceed the member design capacity.

Table 3-1. Performance levels and analysis approaches

Earthquake Ground Motion Level (DD)	$\text{SDC} = 1{,}1\text{a}^{(1)}, 2{,}2\text{a}^{(1)}, 3{,}3\text{a}, 4{,}4\text{a}$		$\text{SDC} = 1\text{a}^{(2)}, 2\text{a}^{(2)}$	
	Normal Performance Target	Evaluation/Design Approach	Advanced Performance Target	Evaluation/Design Approach
DD-3	–	–	LD (Limited damage)	Nonlinear
DD-2	Controlled Damage (CD)	Strength	CD	Strength
DD-1	–	–	CD	Nonlinear

Analysis Procedure Selection for Earthquake Loads

The selection of the analysis procedure to be followed during structural analysis of the case study buildings is carried out in accordance with the requirements of TSC2018 Section 4.6.2. According to TSC2018 Section 4.6.2, the response spectrum analysis and the equivalent lateral force (ELF) methods are the two linear analysis methods fit for earthquake loads calculation. Within this study, the ELF method is deemed appropriate due to the fact that the CFS-RuC buildings are situated in BHC=5 and SDC=1 (see Table 3-2).

Table 3-2. Types of buildings that are appropriate for ELF method

Building Type	Allowable building height class	
	SDC = 1,1a, 2,2a	SDC = 3,3a, 4,4a
Buildings where the torsional irregularity coefficient at each floor meets the condition $\eta_{bi} \leq 2.0$ and also without B2 type irregularity	BHC ≥ 4	BHC ≥ 5
All other buildings	BHC ≥ 5	BHC ≥ 6

Calculation for the Fundamental Periods

Observation shows that the representative CFS-RuC buildings can be designed by following a strength design approach, and the equivalent lateral force method can be implemented in the analysis phase. According to TSC 2018 Section 4.7.3.1, the procedures of the equivalent lateral force method state that, in case no other exact calculations are done for the fundamental periods of the first mode, Equation (3-5) will be used for period estimation. Alternatively, these periods can be generated automatically from the modal analysis runned by SAP2000 analysis software. Both calculations by the analysis software and Equation (3-5) are computed and compared to each other. First, the mass of the building is estimated by using the Equation (3-6) and second, fictitious forces, F_{fi} and their corresponding lateral floor displacements, d_{fi} are computed in SAP2000. For demonstration purposes, the mass of a normal floor, m_i is calculated and result of the total building weight is presented below in Table (3-3).

$$T_p^{(x)} = 2\pi \left(\frac{\sum_{i=1}^{N} m_i d_{fi}^{(x)2}}{\sum_{i=1}^{N} F_{fi}^{(x)} d_{fi}^{(X)}} \right)^{1/2} \tag{3-5}$$

$$\begin{aligned} m_i = \frac{w_i}{g} = \frac{1}{g}[G_i + n(Q_i)] \\ &= \frac{1}{9.81}[(20 \times 20) \times (4.3 + 0.3 \times 2.0) + 4 \times 20 \times 3.0 + 549.25] \\ &= 280 \text{ kN} - \text{s}^2/\text{m} \end{aligned} \tag{3-6}$$

Table 3-3. Story weights and masses for the 8-story building

Story	w_i (kN)	m_i (kN-s^2/m)
8	2429.25	248
7	2749.25	280
6	2749.25	280
5	2749.25	280
4	2749.25	280
3	2749.25	280
2	2749.25	280
1	2749.25	280
Σ	21674	2208

In these equations, w_i, G_i, Q_i represent total floor weight, dead and live loads, respectively and n is live load mass participation ratio, which is taken from TSC2018 Table 4.3 as n=0.3. The self-weight of a single storey was calculated as 549.25 kN (including weights of beams and columns).

The fictitious forces, F_{fi} in Equation (3-7), TSC2018 formula 4.26 are proportional to the storey weight and storey height. They are calculated as presented in Table (3-4) from the formula below and Fo = 1000 kN is assumed in this case to be distributed among the stories as follows:

$$F_{\mathrm{fi}} = F_{\mathrm{o}} \frac{m_{\mathrm{i}} H_{\mathrm{i}}}{\sum_{\mathrm{j}=1}^{\mathrm{N}} m_{\mathrm{j}} H_{\mathrm{j}}} \tag{3-7}$$

Table 3-4. Lateral floor displacements in the x-direction resulting from fictitious loadings

Story	F_{fi} (kN)	d_{fi} (m)	m_i	$m_i d_{fi}^2$	$F_{fi} d_{fi}$
8	202	0.0448	248	0.4977	9.036398
7	200	0.0426	280	0.5091	8.507268
6	171	0.0389	280	0.4245	6.658903
5	143	0.0338	280	0.3192	4.811965
4	114	0.0274	280	0.2098	3.120719
3	86	0.0200	280	0.1121	1.710921
2	57	0.0124	280	0.0431	0.707181
1	29	0.0060	280	0.0100	0.169951
Σ	1000			2.1254	34.72331

Therefore, the fundamental period in the x-direction can be calculated as follows:

$$T_{\mathrm{p}}^{(\mathrm{x})} = 2\pi \left(\frac{\sum_{\mathrm{i}=1}^{\mathrm{N}} m_{\mathrm{i}} d_{\mathrm{fi}}^{(\mathrm{x})2}}{\sum_{\mathrm{i}=1}^{\mathrm{N}} F_{\mathrm{fi}}^{(\mathrm{x})} d_{\mathrm{fi}}^{(\mathrm{X})}} \right)^{1/2} = 2\pi \left(\frac{2.1254}{34.7233} \right)^{1/2} = 1.554\ s$$

Similarly, the fundamental period in the y-direction is found to be $T_{\mathrm{p}}^{(\mathrm{y})} = 1.72\ s$. Table (3-5) presents the modal analysis results of the 8-story building. As shown the fundamental modes of vibration are given with the periods in the x- and y-directions being 1.54s and 1.70s respectively. Both SAP2000-generated and hand-calculated period results agree reasonably as there is less than 1% difference in the value of the periods estimated.

Table 3-5. Lateral floor displacements in the x-direction resulting from fictitious loading

Mode	Period (s)	UX	UY	SumUX	SumUY
1	1.706	0	**0.8200**	0	0.82
2	1.540	**0.8100**	0	0.81	0.83
3	1.297	0	0	0.81	0.83
4	0.571	0	0.1100	0.81	0.93
5	0.517	0.1100	0	0.93	0.93
6	0.435	0	0	0.93	0.93
7	0.340	0	0.0380	0.93	0.97
8	0.308	0.0404	0	0.97	0.97
9	0.260	0	0	0.97	0.97
10	0.240	0	0.0149	0.97	0.99
11	0.227	0	0	0.97	0.99
12	0.227	0	0	0.97	0.99

However, Section 4.7.3.2 of TSC 2018 restricts the period obtained using Equation (3-7) such that it can’t be larger than 1.4 times the period value obtained using Equation (3-8) below. As mentioned by Section4.7.3.4, for the CFS-RuC buildings, which are not steel or RC structures, C_t factor can be taken as 0.07. Hence the criteria in Section4.7.3.2 is checked as shown below and the periods given by the empirical Equation (3-8) are selected to be used for further calculations.

$$T_{\mathrm{pA}} = C_{\mathrm{t}} H_{\mathrm{N}}^{3/4} \tag{3-8}$$

$$T_{\mathrm{p}}^{(\mathrm{X})} = 1.554\ \mathrm{s} > T_{\mathrm{pA}}^{(\mathrm{X})} = 1.4 C_{\mathrm{t}} H_{\mathrm{N}}^{3/4} = 1.4(0.07)(25.6)^{\frac{3}{4}} = 1.115\ \mathrm{s}$$

$$T_{\mathrm{p}}^{(\mathrm{y})} = 1.70\ \mathrm{s} > T_{\mathrm{pA}}^{(\mathrm{y})} = 1.4 C_{\mathrm{t}} H_{\mathrm{N}}^{3/4} = 1.4(0.07)(25.6)^{\frac{3}{4}} = 1.115\ \mathrm{s}$$

Therefore the modified fundamental period in both X- and Y-directions is T= 1.115 s

Earthquake Load Reduction Factor

Considering that the concept of CFS-RuC buildings is newly introduced, there is no plausible way of obtaining the true behavior factor for such buildings other than carrying out experimental studies or other long studies explicity made for the behavior factor estimation. Otherwise, reduction factors of systems that resemble the CFS-RuC buildings in terms of seismic behavior should be embraced. For instance, the library of seismic load reduction factors presented in Table 4.1 of TSC2018 do not cover the case study buildings. Fortunately, the rich library of ASCE7-22 Table 12.2-1 [43] can be consulted to select a reasonable reduction factor for our particular buildings. For our case, since the CFS-RuC buildings are composite structures and features semi-rigid (partially restrained) connections, the reduction factor R=6 and the overstrength factor D=3 dedicated for 'steel and concrete composite partially restrained moment frames' are adopted from the ASCE7-22 Table 12.2-1 to be used in the seismic design. Additionally, a close value of R=6.5 adopted from Eurocode 8 [44], was used in the study by [45] for a building system composed of CFST columns and steel beams. This further increases the confidence in the assumption made for the reduction factor of the CFS-RuC buildings.

For both x- and y-directions, the actual reduction factor, $R_a(T)$ will be calculated using Equation (3-9) since $T_\mathrm{p}^{(\mathrm{X})} = T_\mathrm{p}^{(\mathrm{Y})} = 1.115\ \mathrm{s} > T_\mathrm{B} = 0.249\ \mathrm{s}$. Also, by using Equations (3-9) and (3-10) the variation of the reduction factor in respect to all period values can be obtained. Finally, for every calculated value of $R_a(T)$, the corresponding reduced spectral acceleration S_{aR} can be obtained using Equation (3-11) which eventually generates the reduced design spectrum as illustrated in Fig.(3-5).

$$R_\mathrm{a}(T) = \frac{R}{I} \qquad\qquad T > T_B \qquad\qquad (3\text{-}9)$$

$$R_{\mathrm{a}}(T) = D + \left[\frac{R}{I} - D\right]\frac{T}{T_B} \qquad T \leq T_B \tag{3-10}$$

$$= R_{\mathrm{a}}\left(T_{\mathrm{p}}^{(\mathrm{X})}\right) = R_{\mathrm{a}}\left(T_{\mathrm{p}}^{(\mathrm{Y})}\right) = \frac{R^{(\mathrm{X})}}{I} = \frac{R^{(\mathrm{Y})}}{I} = \frac{6}{1} = 6$$

$$S_{\mathrm{aR}}(T) = \frac{S_{\mathrm{ae}}(T)}{R_{\mathrm{a}}(T)} \tag{3-11}$$

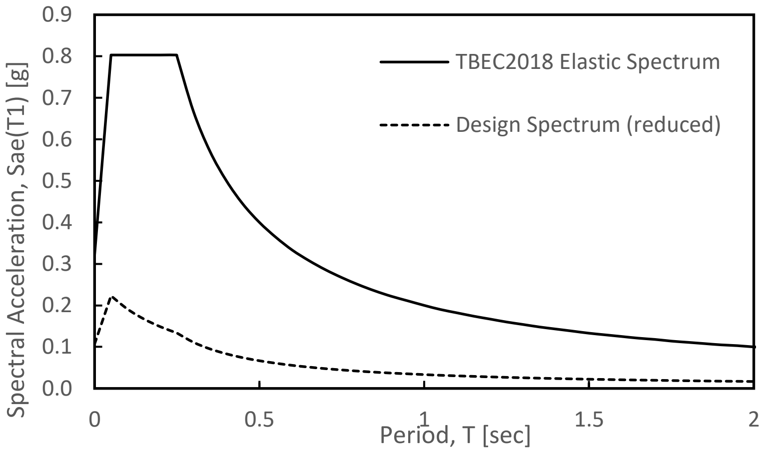

Figure 3-5. The reduced response spectrum for seismic design

Calculation for the Equivalent Lateral Force (Base Shear)

The total lateral force acting on the 8-story CFS-RuC building is computed using Equation (3-12) based on the TSC2018. The reduced spectral acceleration, $S_{\mathrm{aR}}(T)$ corresponding to the period, T=1.115s of the case study building is obtained first from Fig.(3-5) above and then replaced in Equation (3-12). Since the period is the same for both x- and y-directions, calculations are computed for only one direction.

$$V_{\mathrm{tE}}^{(\mathrm{X})} = m_{\mathrm{t}} S_{\mathrm{aR}}\left(T_{\mathrm{p}}^{(\mathrm{X})}\right) \geq 0.04 m_{\mathrm{t}} I S_{\mathrm{DS}} g \tag{3-12}$$

The total seismic mass, m_t in Equation 3-6 has been estimated before in Table (3-3). Therefore that mass is based on to derive equivalent lateral forces of individual stories as depicted in Table (3-6).

$$V_{\mathrm{tE}}^{(\mathrm{X})} = 2208 \times 0.0299g \geq 0.04 \times 2208 \times 1.0 \times 0.803g$$

$$V_{\mathrm{tE}}^{(\mathrm{X})} = 648\ \mathrm{kN} < 695\ \mathrm{kN}$$

Given that the minimum acceptable base shear, V_{tE}= 695 kN is larger than the principal base shear, it will control. In order to be able to determine the internal forces and moments of structural members later in the design part, the total base shear V_{tE} needs to be distributed proportionally to individual floor heights and weights using the Equation (3-13) shown below. The expression, $\Delta F_{\mathrm{NE}}^{(\mathrm{X})}$, which stands for the additional fictious load at the top floor, is obtained with the help of Equation (3-14) and all results of the procedure are summarized in Table (3-6).

$$F_{\mathrm{iE}}^{(\mathrm{X})} = \left(V_{\mathrm{tE}}^{(\mathrm{X})} - \Delta F_{\mathrm{NE}}^{(\mathrm{X})}\right) \frac{m_{\mathrm{i}} H_{\mathrm{i}}}{\sum_{\mathrm{j=1}}^{\mathrm{N}} m_{\mathrm{j}} H_{\mathrm{j}}} \tag{3-13}$$

$$\Delta F_{\mathrm{NE}}^{(\mathrm{X})} = 0.0075 N V_{\mathrm{tE}}^{(\mathrm{X})} = 0.0075(8)(695) = 41.7\ \mathrm{kN} \tag{3-14}$$

Table 3-6. Equivalent lateral forces acting on individual storey

Story	H_i	m_i (kN-s^2/m)	m_iH_i	$m_iH_i/\Sigma m_jH_j$	F_{iE} (kN)
8	25.6	248	6339	0.2016	173
7	22.4	280	6278	0.1996	130
6	19.2	280	5381	0.1711	112
5	16	280	4484	0.1426	93
4	12.8	280	3587	0.1141	75
3	9.6	280	2690	0.0855	56
2	6.4	280	1794	0.0570	37
1	3.2	280	897	0.0285	19
Σ		2208	31449.7	1	695

3.2.5 Structural Irregularities

Based on the standards outlined in TSC 2018 Section 3.6, structures are either be categorized as regular or irregular. Vertical and horizontal configurations shall serve as the basis for such classification. The 8-story CFS-RuC building situation is examined in this section by controlling the irregularities found in this building to be within the limits set by the code.

Horizontal Irregularities (A2, A3)

There are no A2 or A3 horizontal irregularities in the plan owing to the absence of overhangs in the building floor plans, and also thanks to the absence of floor (slab) discontinuities. It is also due to the regular placement of the lateral load-bearing system in the plan. The A2 irregularity is generally identified in buildings where the sum of all openings present at a given floor is larger than a third of the total gross floor area.

Vertical Irregularities (B1, B3)

Similarly, since there are no discontinuities and sudden stiffness reduction in the vertical members of the CFS-RuC structural system, and the story masses do not change along the height of the building, there are no B3 vertical irregularities. The B1 irregularity check is only imposed for reinforced-concrete buildings as per Section 3.6 of TSC 2018, so such check is not be carried out in this study.

Torsional (A1) and Stiffness (Soft Story; B2) Irregularities

Based on criteria of Section 3.6 of TSC 2018 and Equation (3-15), for any given direction of the earthquake at any given floor, the ratio, $\eta_{\mathrm{bi},}$ of the maximum and average interstorey drifts should not surpass 1.2 or else the building has the A1 irregularity.

$$\eta_{\mathrm{bi}} = \left(\Delta_{\mathrm{i}}^{(\mathrm{X})}\right)_{max} / \left(\Delta_{\mathrm{i}}^{(\mathrm{X})}\right)_{\mathrm{avg}} > 1.2 \tag{3-15}$$

Table 3-7. Checks conducted for the A1-type irregularity in the 8-story building

Story	$d_{i(min)}$	$d_{i(max)}$	$\left(\Delta_i^{(X)}\right)_{max}$ (mm)	$\left(\Delta_i^{(X)}\right)_{avg}$ (mm)	$\eta_{bi}^{(X)}$	Condition
8	17.58	21.08	1.08	0.995	1.085427	≤ 1.2
7	16.67	20	1.8	1.675	1.074627	≤ 1.2
6	15.12	18.2	2.6	2.375	1.094737	≤ 1.2
5	12.97	15.6	3.08	2.815	1.094139	≤ 1.2
4	10.42	12.52	2.92	2.67	1.093633	≤ 1.2
3	8	9.6	3.2	2.925	1.094017	≤ 1.2
2	5.35	6.4	3.3	3.025	1.090909	≤ 1.2
1	2.6	3.1	3.1	2.85	1.087719	≤ 1.2

By fulfilling the condition in Equation (3-16), the B2 irregularity is also calculated and presented in Table (3-8) below.

$$\eta_{\mathrm{ki}} = \left(\Delta_{\mathrm{i}}^{(x)}/h_{\mathrm{i}}\right)_{\mathrm{avg}} / \left(\Delta_{\mathrm{i}\pm1}^{(x)}/h_{\mathrm{i}\pm1}\right)_{\mathrm{avg}} > 2.0 \tag{3-16}$$

Table 3-8. B2 type stiffness-soft story irregularity condition check

Story	$\left(\Delta_{\mathrm{i}}^{(X)}/\mathrm{h_i}\right)_{\mathrm{avg}}$	$\left(\Delta_{\mathrm{i-1}}^{(X)}/\mathrm{h_{i-1}}\right)_{\mathrm{avg}}$	$\eta_{\mathrm{ki}}^{(X)}$	Condition
8-7	0.000311	-	-	≤ 2.0
7-6	0.000523	0.000523	1.683417	≤ 2.0
6-5	0.000742	0.000742	1.41791	≤ 2.0
5-4	0.00088	0.00088	1.185263	≤ 2.0
4-3	0.000834	0.000834	0.94849	≤ 2.0
3-2	0.000914	0.000914	1.095506	≤ 2.0
2-1	-	0.000945	1.034188	≤ 2.0

The displacement values given in the tables above are the values obtained as a result of the analysis of the system carried out after the final design of the CFS-RuC structural system members is completed. As displayed in Table (3-7) and Table (3-8), it is seen that the A1 type torsional irregularity coefficient of the building on each floor satisfies the condition [nbi < 1.2], and there is also no B2 type stiffness-soft story irregularity in the building. This shows that the examined system meets the conditions in the first line of TSC 2018 Table 4.4, and hence the equivalent lateral force method (ELF) can be undoubtedly applied in the seismic analysis of the CFS-RuC structures.

3.2.6 Effective Interstory Drift Determination and Control

Prior to estimating the effective interstory drift between two consecutive stories, the story displacement, Δ at the centers of mass at the top and bottom of the story being examined is determined first as demonstrated in Equation (3-17). The lateral floor displacements, $u_{\mathrm{i}}^{(\mathrm{X})}$ and $u_{\mathrm{i-1}}^{(\mathrm{X})}$ are extracted at the column ends, which are subjected to the reduced earthquake loads.

$$\Delta_{\mathrm{i}}^{(\mathrm{X})} = u_{\mathrm{i}}^{(\mathrm{X})} - u_{\mathrm{i-1}}^{(\mathrm{X})} \tag{3-17}$$

$$\delta_{\mathrm{i}}^{(\mathrm{X})} = \frac{R}{I} \Delta_{\mathrm{i}}^{(\mathrm{X})} \tag{3-18}$$

The actual expression to control the effective interstory drift is given below in Equation (3-19). The λ and κ factors used in the drift calculation are specified observing the criteria 4.9.1.4 of the TSC2018. In this particular case, in order to compute the factor, λ as displayed in Equation (3-20), the spectral acceleration according to the DD-3 earthquake ground level is obtained as $S_{\mathrm{ae}}(T_{\mathrm{p}})_{\mathrm{DD-3}} = 0.0717$ in advance by following the same procedure used for the DD-2 case. The factor, κ is assumed to be 0.5 since the CFS-RuC buildings employ connections made from steel.

$$\lambda \frac{\delta_{i,max}^{(\mathrm{X})}}{h_{\mathrm{i}}} \leq 0.016\kappa \tag{3-19}$$

$$\lambda = \frac{S_{\mathrm{ae}}(T_{\mathrm{p}})_{\mathrm{DD-3}}}{S_{\mathrm{ae}}(T_{\mathrm{p}})_{\mathrm{DD-2}}} = \frac{0.0717}{0.1794} = 0.4 \tag{3-20}$$

Table 3-9. Calculations of the effective interstory drifts in the x-direction

Story	h_{i} (m)	$u_{\mathrm{i}}^{(\mathrm{X})}$ (mm)	$u_{\mathrm{i-1}}^{(\mathrm{X})}$ (mm)	$\Delta_{\mathrm{i}}^{(\mathrm{X})}$ (mm)	$\delta_{\mathrm{i}}^{(\mathrm{X})} = \frac{R}{I}\Delta_{\mathrm{i}}^{(\mathrm{X})}$	$\lambda\frac{\delta_{\mathrm{i}}^{(\mathrm{X})}}{h_{\mathrm{i}}}$
8	3.2	22.66	21.6	1.06	6.36	0.00079
7	3.2	21.6	19.73	1.87	11.22	0.0014
6	3.2	19.73	17.14	2.59	15.54	0.00194
5	3.2	17.14	13.93	3.21	19.26	0.00241
4	3.2	13.93	10.24	3.69	22.14	0.00277
3	3.2	10.24	6.37	3.87	23.22	**0.0029**
2	3.2	6.37	3.06	3.31	19.86	0.00248
1	3.2	3.06	-	3.06	18.36	0.0023

As an example, check for the maximum drift value obtained for the 3rd floor in Table (3-15) is performed, as follows:

$$\lambda\frac{\delta_{i,max}^{(x)}}{h_i} = 0.4 \times \frac{23.22}{3200} = 0.0029 \leq 0.008 = 0.016\kappa \qquad \text{OK}$$

3.2.7 Second-order Effects

TSC 2018 Section 4.9.2 is taken into account for second-order effect checks. These effects induce extra story shears, moments and internal member forces. Therefore, it is recommended to consider them within the analysis. Their significance increases when the stability coefficient, $\theta_{\mathrm{II,i}}^{(\mathrm{X})}$ given by Equation (3-21) is equal to or larger than, $\theta_{\mathrm{II,max}}^{(\mathrm{X})}$ determined following Equation (3-22). In case the obtained stability coefficient is below the maximum value, their effects can be ignored. Contrarily, if the maximum value is exceeded, the second-order amplification factor, $\beta_{\mathrm{II}}^{(\mathrm{X})}$ defined in Section4.9.2.3 of TSC 2018 is determined to be multiplied to the internal forces. Otherwise, the other alternative is to increase either the structural stiffness of the building or the strength and then repeat the seismic analysis.

$$\theta_{\mathrm{II,i}}^{(\mathrm{X})} = \frac{\left(\Delta_{\mathrm{i}}^{(\mathrm{X})}\right)_{\mathrm{avg}} \sum_{\mathrm{k=i}}^{\mathrm{N}} w_{\mathrm{k}}}{V_{\mathrm{i}}^{(\mathrm{X})} h_{\mathrm{i}}} \tag{3-21}$$

$$\theta_{\mathrm{II\,max}}^{(\mathrm{X})} \leq 0.12\,\frac{D}{C_{\mathrm{h}} R} \tag{3-22}$$

In the equations above, V_i/Δ_i is the story stiffness. The value of the expressions, total weight w_{k} at given floor, the reduction factor R, and overstrength factor D are determined in the sections above whereas the C_h empirical factor related to the nonlinear hysteretic behaviour of the system is to be obtained from Section 4.9.2.2 as C_h=1 for composite structures. As Table (3-10) below illustrates it, the $\theta_{\mathrm{II,max}}^{(\mathrm{X})}$ is not exceeded hence second-order effects arenot be taken into account in the analysis.

Table 3-10. Check for the second-order effects in the x-direction

Story	Hi(mm)	Δi_{avg} (mm)	$\sum W_k$(kN)	V_i(kN)	$\theta_{ll,i}$	$\theta_{ll,\,max}$
8	3200	0.995	2429	173	0.00437	0.06
7	3200	1.675	5179	303	0.00893	0.06
6	3200	2.375	7928	415	0.01417	0.06
5	3200	2.815	10677	508	0.01848	0.06
4	3200	2.67	13426	583	0.01922	0.06
3	3200	2.925	16176	639	0.02315	0.06
2	3200	3.025	18925	676	0.02646	0.06
1	3200	2.85	21674	695	0.02779	0.06

3.2.8 Load Combinations

The ambiguity present in the determination of loads that are likely to cause failure to the structure leads to the implementation of load combinations. Load combinations assist in assessing all possible scenarios of critical load arrangements so that the building design process generates a robust structure. Both load combination recommendations from Turkish Steel Code TCSC 2016 Section 5.3.1 [46] and Turkish Seismic Code TSC

2018 Section 9.2.5 [38] are taken into accounts and the resulting combinations are shown in Equations (3-24). Also, by following the criteria 4.4.3 of TSC 2018 that impose the representation of the effects of the vertical component of the earthquake, $E_{\mathrm{d}}^{(\mathrm{Z})}$. It is done by integrating the, $E_{\mathrm{d}}^{(\mathrm{Z})}$ given by Equation (3-23) into Equations (3-24) and (3-25) as shown below. G represents the dead loads, while Q, S and H respectively are the live, snow and lateral soil effect loads.

$$\begin{aligned} E_{\mathrm{d}}^{(\mathrm{Z})} &\approx \left(\frac{2}{3}\right) S_{\mathrm{DS}} G \\ &= \frac{2}{3} \times 0.803 \times G \\ &= 0.535G \end{aligned} \tag{3-23}$$

$$\begin{aligned} &1.2\,G + 0.5Q + 0.2S + E_{\mathrm{d}}^{(\mathrm{H})} + 0.3E_{\mathrm{d}}^{(\mathrm{Z})} \\ &\quad = (1.2\,G + 0.3 \times 0.535G) + 0.5Q + 0.2S + E_{\mathrm{d}}^{(\mathrm{H})} \\ &\quad = 1.361G + 0.5Q + 0.2S + E_{\mathrm{d}}^{(\mathrm{H})} \end{aligned} \tag{3-24}$$

$$\begin{aligned} &0.9G + H + E_{\mathrm{d}}^{(\mathrm{H})} - 0.3E_{\mathrm{d}}^{(\mathrm{Z})} \\ &= (0.9G - 0.3 \times 0.535G) + H + E_{\mathrm{d}}^{(\mathrm{H})} \\ &= 0.74G + H + E_{\mathrm{d}}^{(\mathrm{H})} \end{aligned} \tag{3-25}$$

The condition 4.4.2.1 of TSC 2018, which proposes the superposition of the x- and y-components of the horizontal components of the earthquake, is accounted for as indicated in Equations (3-26) and (3-27) below.

$$E_{\mathrm{d}}^{(\mathrm{H})} = \pm E_{\mathrm{d}}^{(\mathrm{X})} \pm 0.3E_{\mathrm{d}}^{(\mathrm{Y})} \tag{3-26}$$

$$E_{\mathrm{d}}^{(\mathrm{H})} = \pm 0.3E_{\mathrm{d}}^{(\mathrm{X})} \pm E_{\mathrm{d}}^{(\mathrm{Y})} \tag{3-27}$$

For all gravity loads, their corresponding notional loads, $N_{\mathrm{i}} = 0.002\alpha Y_{\mathrm{i}}$ are calculated as well and are added into the load combinations to account for geometric imperfections in member sections. All LRFD load combinations that participate in the member design calculations are, as follows:

- $1.4G$
- $1.2G + 1.6Q$
- $1.2G + 1.6S$
- $1.2G + 1.6Q + 0.5Q_{\mathrm{r}}$
- $1.2G + 1.6Q + 0.5S$
- $1.2G + 1.6Q_{\mathrm{r}} + 0.5Q$
- $1.361G + 0.5Q + 0.2S \pm E_{\mathrm{d}}^{(\mathrm{X})} \pm 0.3E_{\mathrm{d}}^{(\mathrm{Y})}$
- $1.361G + 0.5Q + 0.2S \pm 0.3E_{\mathrm{d}}^{(\mathrm{X})} \pm E_{\mathrm{d}}^{(\mathrm{Y})}$
- $0.74G \pm E_{\mathrm{d}}^{(\mathrm{X})} \pm 0.3E_{\mathrm{d}}^{(\mathrm{Y})}$
- $0.74G \pm 0.3E_{\mathrm{d}}^{(\mathrm{X})} \pm E_{\mathrm{d}}^{(\mathrm{Y})}$

3.3 Member Design

Design of CFS-RuC members entails ensuring the selection of an appropriate composite cross-section that has both adequate strength and fulfill the code requirements. Throughout the beam and column design process, to be on a conservative side, the contribution of the RuC infill to the flexural moment capacity of the composite section is ignored. So, CFS-RuC beam members are treated as typical built-up cold-formed members. That's why the DSM method is implemented as well as the finite strip analysis in the CUFSM [47] program. However, during calculations of the axial compression capacity of columns, the contribution of RuC infill is incorporated in the total compressive strength. In fact, the slender steel elements alone can not meet the high axial compression demand present in multi-story buildings, and the compressive capacity of

RuC must be relied on to meet such demand. Additionally, current design approaches of concrete-filled steel columns presented in Turkish Steel Code (TCSC 2016) is adopted in the design of CFS-RuC beam-columns. With the limited number sections available to be integrated in the design of CFS-RuC structures, for all members at a given story only one CFS-RuC beam and column section is designed.

3.3.1 Beam Design

The required strengths of CFS-RuC beams are computed with the help of SAP2000 analysis software. At the end of the analysis, internal forces resulting from the load combination that provide the most unfavorable case are based on for the design. On the other hand, a bare shape of the CFS-RuC section is selected in order to determine its flexural bending capacity and then the shear resistance is checked. If the selected bare shape doesn't meet the strength requirement, a different shape is tried until the requirement is fulfilled. The controlling load combination and corresponding required moment and shear obtained for the beams at the first floor are given below.

$$1.361G + 0.5Q + 0.2S \pm E_{\mathrm{d}}^{(\mathrm{X})} \pm 0.3E_{\mathrm{d}}^{(\mathrm{Y})}$$

$$M_{\mathrm{r}} = -103.72 \text{ kNm} \quad V_{\mathrm{r}} = -99 \text{ kN}$$

Flexural Strength Calculation

This section shows the flexural strength calculations performed for the beam section B-4-250-350, with the properties given below in Table 3-11.

Table 3-11.Geometric properties of the beam section B-4-250-350

Bare section: B-4-250-350	
A = 5122.03 mm^2 Zcg = 177 mm Ix = 9.97x10^7 mm^4 J = 27780 mm^4 Iz = 5.51x10^7 mm^4 b = 250 mm Xcg = 126 mm h = 350 mm t = 4mm Note: t is thickness; b and h are member's width and height; Ix,Iz are the moment of inertia in the strong and weak direction of the section, while A and X, Zcg are the area and centers of gravity. J is the torsional moment of inertia.	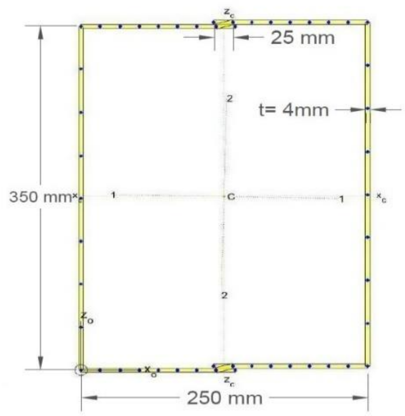

The flexural strength, M_n of the B-4-250-350 bare beam section is the minimum of M_{ne}, M_{nl}, M_{nd}, where M_{ne}, M_{nl}, and M_{nd} are the nominal flexural strengths for lateral-torsional buckling, local buckling, and distortional buckling respectively, and M_{cre}, M_{crl}, M_{crd} are their corresponding critical elastic buckling moments. First the finite strip analysis of the section in pure bending is conducted in the CUFSM software [47] and load factors are obtained as follows in Fig. (3-6).

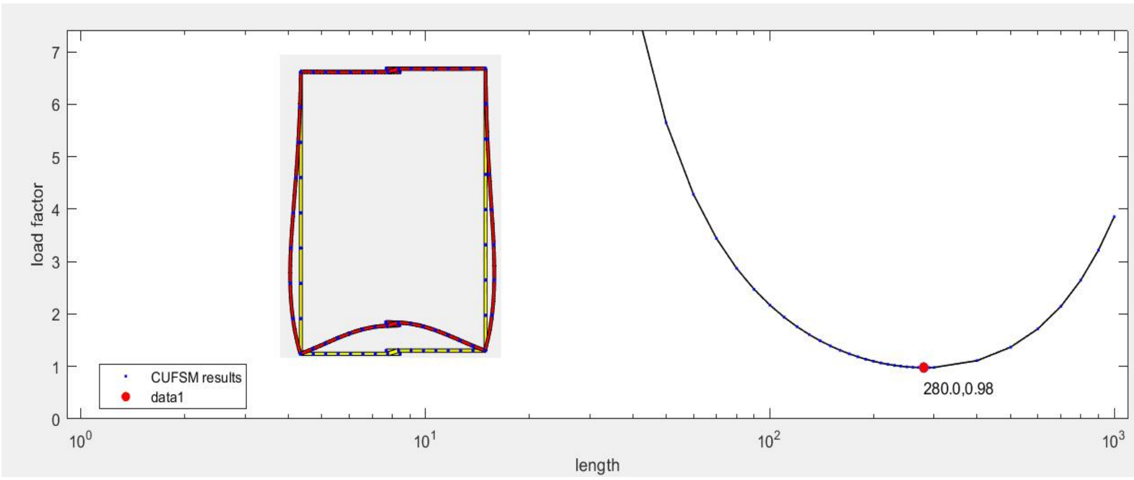

Figure 3-6. Signature curve and elastic buckling mode under pure bending

Finite strip analysis results include:

The yield moment $M_y = 152.65$ kNm

$M_{cr\ell}/M_y = 0.98$ $M_{cre}/M_y \approx \infty$ $M_{crd}/M_y \approx \infty$

The obtained signature curve suggests that this type of section is only susceptible to local buckling failure. Lateral-torsional and distortional buckling failures happen at a larger load factor close to infinity. As a result, both buckling modes don't exist and don't appear on the signature curve. Therefore, their nominal flexural strengths are directly equal to the member yield strength as demonstrated below.

Lateral-torsional buckling strength:

$M_{cre}/M_y \approx \infty$ $M_{cre} \approx \infty$

For $M_{cre} > 2.78M_y$ $\infty > 2.78M_y$

$M_{ne} = M_y$ $M_{ne} = 152.65\ kNm$

Distortional buckling strength:

$M_{crd}/M_y \approx \infty$ $M_{crd} \approx \infty$

$$\lambda_d = \sqrt{M_y/M_{crd}} = \sqrt{\frac{152.65}{\infty}} = 0$$

For $\lambda_d \leq 0.673$ $0 \leq 0.673$

$M_{nd} = M_y$ $M_{nd} = 152.65\ kNm$

Local buckling strength:

$M_{cr\ell} = 150$ kNm

$$\lambda_\ell = \sqrt{M_{ne}/M_{cr\ell}} = \sqrt{\frac{152.65}{150}} = 1.009$$

For $\lambda_\ell > 0.776$ $1.009 > 0.776$

$$M_{n\ell} = \left(1 - 0.15\left(\frac{M_{cr\ell}}{M_{ne}}\right)^{0.4}\right)\left(\frac{M_{cr\ell}}{M_{ne}}\right)^{0.4} M_{ne}$$

$$\mathrm{M_{n\ell}} = \left(1 - 0.15\left(\frac{150}{152.65}\right)^{0.4}\right)\left(\frac{150}{152.65}\right)^{0.4} 152.65 = 129\ kNm$$

Predicted flexural strength:

$$M_\mathrm{n} = min\left(\mathrm{M_{ne,}M_{nl,}M_{nd}}\right)$$

$$M_\mathrm{n} = min(152.65,129,152.65)$$

$$M_\mathrm{n} = 129\ kNm$$

Based on LRFD, material strength factor for bending: $\phi_\mathrm{b} = 0.9$

$$\frac{M_\mathrm{r}}{\phi_\mathrm{b} M_\mathrm{n}} = \frac{103.72}{116.1} = 0.89 \leq 1.0 \quad \boldsymbol{OK}$$

Shear Resistance

The obtained maximum shear buckling force, $V_r = 99$ kN.

Therefore the yield shear strength V_y of the section depends on area Aw and yield strength Fy, as follows:

$$V_y = 0.6\mathrm{A_W F_y} = 0.6 \times 2(350 \times 4) \times 275 = 462\ kN$$

$$\frac{V_r}{V_\mathrm{y}} = \frac{99}{462} = 0.214 \leq 1.0 \quad \boldsymbol{OK}$$

3.3.2 Beam-Column Design

Unlike the beam design that uses the DSM method, the design of conventional CFS beam-column members follows the methodology of the main specification, AISI-S100 [48]. However, the DSM method is used to calculate the basic beam (Mn) and column strengths (Pn) to be used in the LRFD interaction equation. Also, for the design of CFS-RuC beam-columns, the same methodology is used but the interaction equation is modified to account for the RuC contribution to the compressive strength. Here, demonstration for the design of columns at the third floor is carried out. The required strengths are determined using the first order elastic analysis as recommended by

SectionC5.2.2 of AISI-S100. The additional requirements of the first order analysis are fulfilled by including in the load combinations additional lateral load, $N_i = 0.0042Y_i$ and the nonsway amplification factor was assumed to be B_1=1 since CFS-RuC beam-columns are not subjected to transverse loads. As a result the required moment, Mr and compressive strength, Pr are obtained as shown below:

$M_{1\mathrm{r}} = 90\ kNm$ $\qquad$ $P_{1\mathrm{r}} = 741\ kN$

$M_{2\mathrm{r}} = 67\ kNm$ $\qquad$ $P_{1\mathrm{r}} = 1242\ kN$

The C-5-195-350 composite section is selected and its properties are given below in Table 3-12.

Table 3-12. Geometric properties of the beam-column section C-5-195-350

Composite section:	C-5-195-350	
As = 5750 mm^2	Zcg = 177 mm	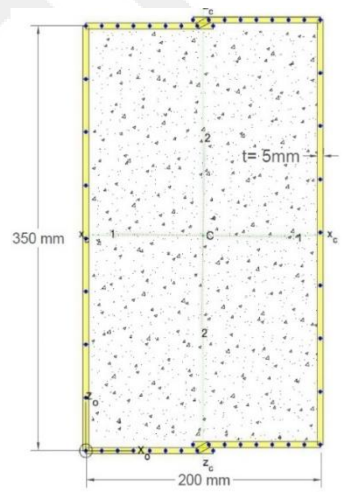
Ac= 64578.55 mm^2	J = 48431 mm^4	
Ix = 1.065×10^8 mm^4	b = 195 mm	
Iz = 4.28×10^7 mm^4	h = 350 mm	
Xcg = 101.25 mm	t = 5mm	

Basic Flexural Strength Calculation of the Beam-column

Following the same steps used in Section (3.2.1) for the beam design, the flexural strength, $\phi_b M_n$ was obtained.

M_y = 163.5 kNm

$M_{cr\ell}/M_y$ = 2.19 $\qquad$ $M_{cre}/M_y \approx \infty$ $\qquad$ $M_{crd}/M_y \approx \infty$

$M_n = \mathrm{My} = 163.5\ kNm$

Based on LRFD $\phi_b = 0.9$ $\phi_b M_n = 147\ kNm$ (3-44)

Basic Compressive Strength Calculation of the Beam-column

The nominal axial strength, Pn, is determined as the minimum of Pne, Pnl and Pnd. From Fig. (3-7), that shows the buckling mode and the signature curve of the composite section, it can be seen that the webs experience outward buckling under compressive stress whereas the deformations in the flanges are inward. The obtained finite strip analysis results are as follows.

$P_y = 1598.24$ kN

$P_{cr\ell}/P_y = 0.7$ $P_{cre}/P_y \approx \infty$ $P_{crd}/P_y \approx \infty$

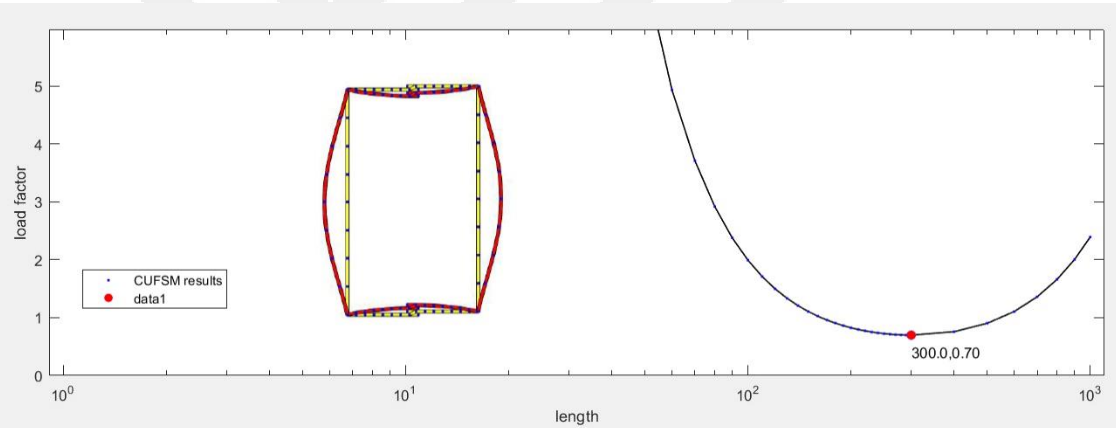

Figure 3-7. Signature curve and elastic buckling mode under axial compression

Flexural-torsional buckling axial strength:

$P_{cre}/P_y \approx \infty$ $P_{cre} \approx \infty$

$$\lambda_c = \sqrt{P_y/P_{cre}} = \sqrt{\frac{1598.24}{\infty}} = 0$$

For $\lambda_c \leq 1.5$ $0 \leq 1.5$

$$P_{ne} = \left(0.658^{\lambda_c^2}\right)P_y = \ (0.658^0)1598.24 = 1598.24\ \text{kN}$$

Local buckling axial strength:

$P_{cr\ell}/P_y = 0.7$ $\quad\quad$ $P_{cr\ell} = 1118.77$ kN

$$\lambda_\ell = \sqrt{P_{ne}/P_{cr\ell}} = \sqrt{\frac{1598.24}{1118.77}} = 1.195$$

For $\lambda_\ell > 0.776$ $\quad\quad$ $P_{n\ell} = \left[1 - 0.15\left(\frac{P_{cr\ell}}{P_{ne}}\right)^{0.4}\right]\left(\frac{P_{cr\ell}}{P_{ne}}\right)^{0.4} P_{ne}$

$1.195 > 0.776$ $\quad\quad$ $P_{n\ell} = \left[1 - 0.15\left(\frac{1118.77}{1598.24}\right)^{0.4}\right]\left(\frac{1118.77}{1598.24}\right)^{0.4} 1598.24 = 1206.84$ kN

Distortional buckling axial strength:

Similarly, $\lambda_d = 0$ hence $P_{nd} = P_y = 1598.24$ kN

Predicted axial strength of the bare CFS section:

$P_n = min(P_{ne,}P_{nl,}P_{nd})$ $\quad\quad$ $P_n = min(1598.24, 1206.84, 1598.24)$

$P_n = 1206.84\ kN$

Based on LRFD: $\quad\quad$ $\phi_c = 0.85$ $\quad$ $\phi_c * P_n = 1025.81\ kN$

Axial strength of the rubberized concrete:

$A_c = 64578.55\ mm^2$

$P_{n,RuC} = 0.85 \times f_{ck} \times A_c = 0.85 \times 21 \times 64578.55 = 1153.11\ kN$

Interaction Equations

In the interaction equation below, the C_{mx}, and α_x coefficients are estimated to be equal to 1. C_{mx} is the end moment coefficient and α_x is the magnification factor.

$$\frac{P}{\phi_c P_{n,CFS} + P_{n,RuC}} + \frac{C_{mx} M_x}{\phi_b M_{nx} \alpha_x} + \frac{C_{my} M_y}{\phi_b M_{ny} \alpha_y} \leq 1.0$$

$$\frac{741}{1025.81 + 1153.11} + \frac{90}{147} + 0 = 0.95 \leq 1.0$$ **OK**

3.4 The Plastic Stress Distribution Approach

In order to compare the design results for CFS-RuC columns obtained in Section 3.3 above, an alternative design approach usually applied to conventional concrete-filled rectangular steel (CFST) sections is adopted. Since the nature of CFS-RuC columns can also be deemed similar to that of CFST members, this approach can be implemented for comparison purpose only. The interaction curves are constructed in accordance with the Turkish Steel Code TCSC 2016 specification. The composite member in consideration, C5-195-350 was first classified as a non-compact section for pure compression following criteria in Table 12.1A of TCSC 2016. Table 12.1B was based on for local buckling classification due to flexure and it was determined that the member is compact for flexure. The plastic strength equations provided in TCSC 2016 are used to construct a piecewise-linear interaction curve of the composite section. Fig. (3-8) presents procedure of the plastic stress distribution method used to create the interaction curve. Referring to Fig.(3-8), the nominal strengths represented by A, B, C, D, E are determined using formulas provided in the Table 12.4 of TCSC 2016 and are calculated as shown below.

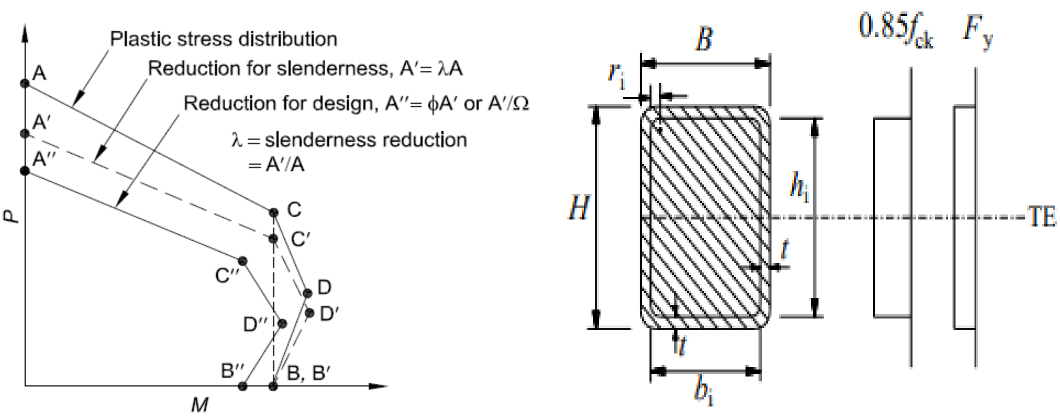

Figure 3-8. Interaction curve for composite columns [46]

and details of a typical composite section

Pure axial compression, at point A in Fig. (3-8):

$$P_{\mathrm{A}} = A_{\mathrm{s}}F_{\mathrm{y}} + 0.85 f_{\mathrm{ck}} A_{\mathrm{c}}$$

$$= [(5750)(275) + 0.85(21)(64578.55)] \times 10^{-3} = 2734\ kN$$

$$M_{\mathrm{A}} = 0$$

Maximum nominal moment strength at D:

$$P_{\mathrm{D}} = \frac{0.85 f_{\mathrm{ck}} A_{\mathrm{c}}}{2}$$

$$= \frac{0.85(21)(64578.55)}{2 \times 10^{3}} = 576.36\ kN$$

The section modulus of the steel hollow section Wpx and Wc for concrete infill is calculated as follows,

$$W_{\mathrm{px}} = 600360\ mm^{3}$$

$$W_{\mathrm{c}} = \frac{b_{\mathrm{i}} h_{\mathrm{i}}^{2}}{4} - 0.192 r_{\mathrm{i}}^{3}$$

$$= \frac{(190\ )(340)^{2}}{4} - 0.192(5\ )^{3} = 5490976\ mm^{3}$$

$$M_{\mathrm{D}} = W_{\mathrm{px}} F_{\mathrm{y}} + \frac{W_{\mathrm{c}}}{2}(0.85 f_{\mathrm{ck}})$$

$$= \left[(600360)(275) + \frac{0.85(21)(5490976)}{2}\right] \times 10^{-6} = 214.11\ kNm$$

Pure bending, B:

$$P_{\mathrm{B}} = 0$$

The effective height h_n for the calculation of nominal strengths at point B,

$$h_{\mathrm{n}} = \frac{0.85 f_{\mathrm{ck}} A_{\mathrm{c}}}{2[0.85 f_{\mathrm{ck}} b_{i} + 4 t F_{\mathrm{y}}]} \le \frac{h_{\mathrm{i}}}{2}$$

$$= \frac{0.85(21)(64578.55)}{2[0.85(21)(190) + 4(5)(275)]} \leq \frac{340}{2}$$

$$= 64.822\ mm\ < 170\ mm$$

$$W_{\mathrm{sn}} = 2th_n^2 = 2 \times 5 \times 64.822^2 = 42018.73\ mm^3$$

$$W_{\mathrm{cn}} = b_i h_n^2 = 190 \times 64.822^2 = 798355.9\ mm^3$$

$$M_{\mathrm{B}} = M_{\mathrm{D}} - W_{\mathrm{sn}} F_{\mathrm{y}} - \tfrac{1}{2} W_{\mathrm{cn}}(0.85 f_{\mathrm{ck}})$$

$$= 214.11 - \left[(42018.73)(275) + 0.85(21)\left(\frac{798355.9}{2}\right)\right] \times 10^{-6} = 195.42\ kNm$$

Intermediate point, C:

$$P_{\mathrm{C}} = 0.85 f_{\mathrm{ck}} A_{\mathrm{c}} = 0.85 \times 21 \times 64578.55 \times 10^{-3} = 1152.73\ kN$$

$$M_{\mathrm{C}} = M_{\mathrm{B}} = 195.42\ kNm$$

Optional point, E

The effective height, h_E at the optional point E is determined,

$$h_{\mathrm{E}} = \frac{h_{\mathrm{n}}}{2} + \frac{H}{4} = \frac{64.822}{2} + \frac{350}{4} = 119.91\ mm$$

$$P_{\mathrm{E}} = \tfrac{0.85 f_{\mathrm{ck}} A_{\mathrm{c}}}{2} + 0.85 f_{\mathrm{ck}} b_{\mathrm{i}} h_{\mathrm{E}} + 4 F_{\mathrm{y}} t h_{\mathrm{E}}$$

$$= \frac{0.85(21)(64578.55)}{2} + 0.85(21)(190)(119.91) + 4(275)(5)(119.91)$$

$$= 1642.55\ kN$$

$$W_{\mathrm{sE}} = 2th_E^2 = 2 \times 5 \times 119.91^2 = 143786.3\ mm^3$$

$$W_{\mathrm{cE}} = b_i h_E^2 = 190 \times 119.91^2 = 2731940\ mm^3$$

$$M_E = M_{\mathrm{D}} - F_{\mathrm{y}} W_{\mathrm{sE}} - \tfrac{1}{2} W_{\mathrm{cE}}(0.85 f_{\mathrm{ck}})$$

$$= 214.11 - \left[(275)(143786.3) + \frac{0.85(21)(2731940)}{2} \right] \times 10^{-6} = 150.18\ kNm$$

By using the obtained five points above, an interaction surface of the composite section is plotted using the calculated nominal strengths as illustrated in Fig.(3-9) below.

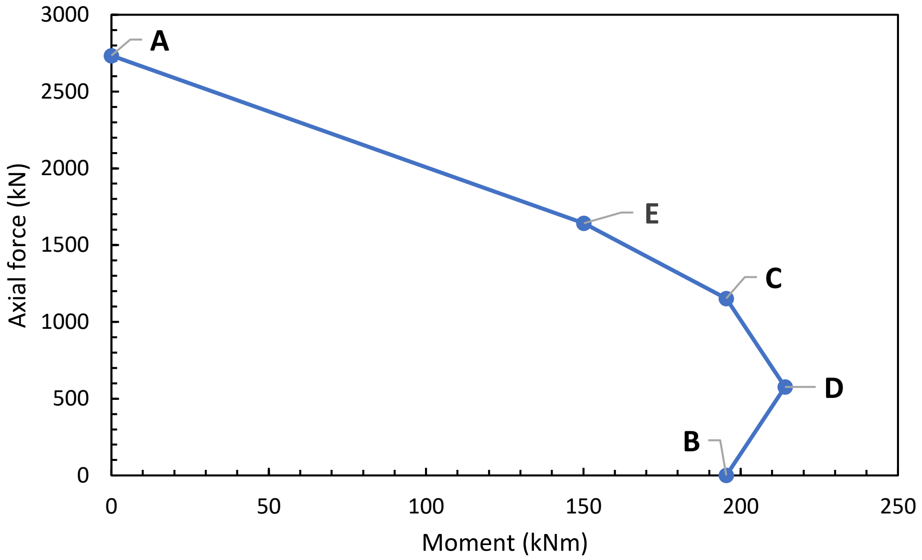

Figure 3-9. Interaction surface for nominal strengths (no length effects)

The curve in Fig.(3-9) is a general representative of the C5-195-350 member strength without taking into account the length effects, that's why a slenderness reduction factor, λ is determined and applied to each point for length effects consideration.

$$\lambda = \frac{P_n}{P_{no}}$$

Let's first determine the axial strengths, Pn and Pno in order to calculate the slenderness reduction factor. $P_{\mathrm{p}}, P_{\mathrm{y}}, \lambda, \lambda_{\mathrm{p}}, and\ \lambda_{\mathrm{r}}$ values are calculated ahead. C_2 value is chosen to be 0.85 since rectangular composite section are used.

$$P_{\mathrm{p}} = F_{\mathrm{y}} A_{\mathrm{s}} + C_2 f_{\mathrm{ck}} \left(A_{\mathrm{c}} + A_{\mathrm{sr}} \frac{E_{\mathrm{s}}}{E_c} \right)$$

$$= 275 \times 5750 + 0.85 \times 21 \times (64578.55 + 0) = 2734\ kN$$

$\lambda = \frac{b}{t} = \frac{350}{5} = 70$ $\lambda_p = 2.26 \times \sqrt{\frac{E}{F_y}} = 2.26 \times \sqrt{\frac{200000}{275}} = 60.94$

$\lambda_r = 3 \times \sqrt{\frac{E}{F_y}} = 3 \times \sqrt{\frac{200000}{275}} = 80.904$

$$P_{\mathrm{y}} = F_{\mathrm{y}} A_{\mathrm{s}} + 0.7 f_{\mathrm{ck}} \left(A_{\mathrm{c}} + A_{\mathrm{sr}} \frac{E_{\mathrm{s}}}{E_{\mathrm{c}}} \right)$$

$$P_{\mathrm{y}} = 275 \times 5750 + 0.7 \times 21 \times (64578.55 + 0) = 2530.55\ kN$$

By replacing the obtained values in the above steps, Pno is found as follows.

$$P_{\mathrm{no}} = P_{\mathrm{p}} - \frac{(\lambda - \lambda_{\mathrm{p}})^2}{(\lambda_{\mathrm{r}} - \lambda_{\mathrm{p}})^2} (P_{\mathrm{p}} - P_{\mathrm{y}})$$

$$= 2734 - \frac{(70 - 60.94)^2}{(80.904 - 60.94)^2} (2734 - 2530.55) = 2692.12\ kN$$

Now let's find C_1, Pe, EI_{eff} values to be used in the computation of Pn.

$$C_1 = 0.25 + 3 \left(\frac{A_s + A_{sr}}{A_g} \right) \leq 0.7 = 0.25 + 3 \left(\frac{5750 + 0}{70000} \right) \leq 0.7 = 0.496 \leq 0.7$$

$$EI_{\mathrm{ef}} = E_{\mathrm{s}} I_{\mathrm{s}} + E_{\mathrm{s}} I_{\mathrm{sr}} + C_1 E_{\mathrm{c}} I_{\mathrm{c}}$$

$$= (200000)(1.065x\ 10^8) + 0.496(14600)(6.223x\ 10^8) = 2.582x10^{13} Nmm^2$$

$$P_e = \frac{\pi^2 (EI_{\mathrm{ef}})}{(Lc)^2} = \frac{\pi^2 (2.582 \times 10^{13})}{(3200)^2 \times 10^{-3}} = 24863.95\ kN$$

$$\frac{P_{no}}{P_e} = \frac{2734}{24863.95} = 0.11 \leq 2.25$$

$$P_n = P_{no} \left(0.658^{\frac{P_{no}}{P_e}} \right) = 2734(0.658^{0.11}) = 2611\ kN$$

$$\lambda = \frac{P_n}{P_{no}} = \frac{2611}{2692.12} = 0.97$$

Corresponding interaction diagrams for other composite column members used in the case study buildings are calculated as well and are presented in Fig.(3-10) , (3-11) and (3-12). Section design results for the case studies are also presented below in Table 3-13.

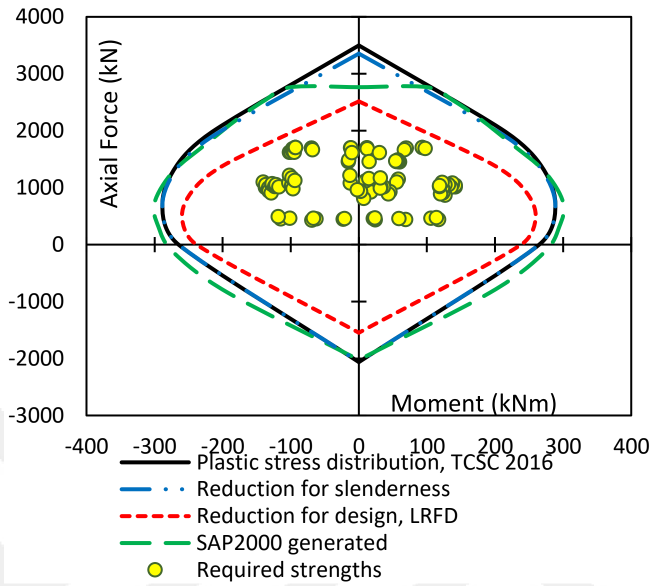

Figure 3-10. Interaction diagram for the CFSRuC4-6#36-6 (250x350) (left) and section design results (right)

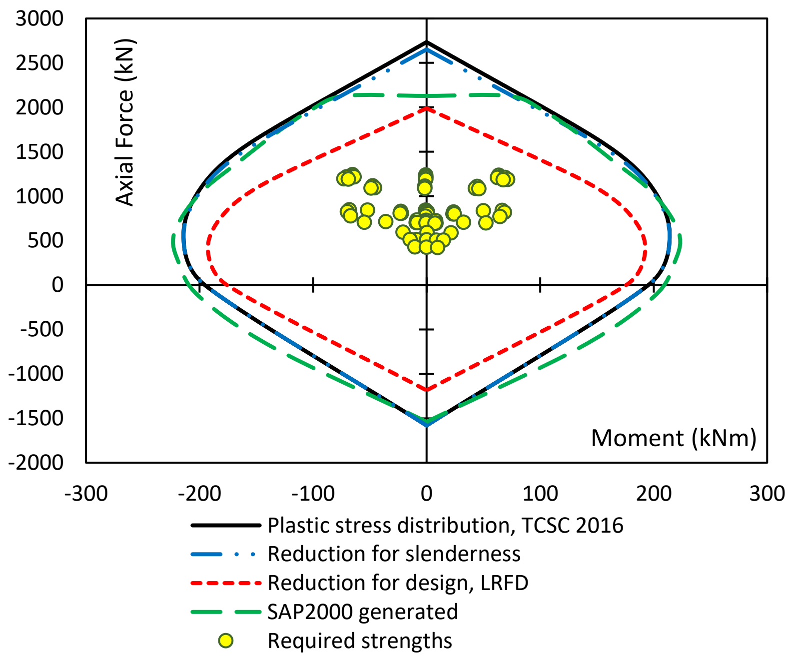

Figure 3-11. Interaction diagram for the CFSRuC4-5#36-6 (195x350)

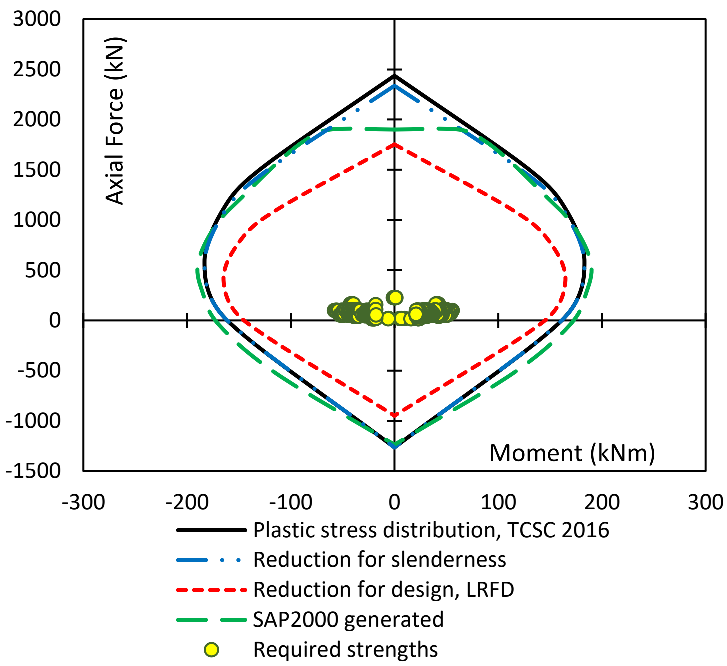

Figure 3-12. Interaction diagram for the CFSRuC3-4#36-6 (195x350)

Table 3-13. Assigned sections from the design and featured connection configurations

Story	Beam	Column	Connection configuration	Elastic stiffness (kN/m)	
1	B4-195-350	C5-195-350	CFSRuC4-5-SP6#36	11641	2-story
2	B3-195-350	C4-195-350	CFSRuC3-4-SP5#36	9844	
1	B4-250-350	C6-250-350	CFSRuC4-6-SP6#36	13850	5-story
2	B4-195-350	C5-195-350	CFSRuC4-5-SP6#36	11641	
3	B4-195-350	C5-195-350	CFSRuC4-5-SP6#36	11641	
4	B4-195-350	C5-195-350	CFSRuC4-5-SP6#36	11641	
5	B3-195-350	C4-195-350	CFSRuC3-4-SP5#36	9844	
1	B4-250-350	C6-250-350	CFSRuC4-6-SP6#36	13850	8-story
2	B4-250-350	C6-250-350	CFSRuC4-6-SP6#36	13850	
3	B4-195-350	C5-195-350	CFSRuC4-5-SP6#36	11641	
4	B4-195-350	C5-195-350	CFSRuC4-5-SP6#36	11641	
5	B4-195-350	C5-195-350	CFSRuC4-5-SP6#36	11641	
6	B4-195-350	C5-195-350	CFSRuC4-5-SP6#36	11641	
7	B4-195-350	C5-195-350	CFSRuC4-5-SP6#36	11641	
8	B3-195-350	C4-195-350	CFSRuC3-4-SP5#36	9844	

CHAPTER IV

PERFORMANCE EVALUATION OF THE CFS-RUC SYSTEMS

4.1 Introduction

Although building codes may impose linear elastic methods for the seismic design of new buildings, in reality, during an event of severe earthquake, buildings undergo large deformations beyond the elastic limit [49]. So, this implies that their evaluation should incorporate nonlinear analysis methods to assess the actual level of the earthquake-induced damages in the system. Such damages are indicated by the formation of plastic hinges in sections. Therefore, the distribution of those section damages throughout the building reveals the performance level of that building. In other words, the performance of a building can be defined as the measure of the damage expected to occur in the structure in case an earthquake happens [50].

Efforts to mitigate life and property losses caused by the earthquakes have led to the development of the Performance-Based Earthquake Engineering (PBEE) framework [51]. In a broad sense, the performance-based design has its origins in the early 20th century. To name some of the early provisions that covered this framework: in 1996, 'Seismic Evaluation and Retrofit of Concrete Buildings' provision from the Applied Technology council (ATC-40) [50] and then in 1997, FEMA-273 [52] together with FEMA-356 [53] released in 2000. All these provisions focused on the rehabilitation of existing structures and constitute most comprehensive guidelines for the PBEE available today. Performance based design deals with choosing the appropriate structural system, provide adequate dimensions of elements that compose the structural bearing system, guaranteeing the service life of the structure and ensuring that the damages that the building might endure during its lifetime do not exceed the predetermined targets. In the study on developing methodologies for PBEE by Chopra and Goel [54], it was highlighted that methods like pushover analysis apart from estimating the overall capacity and inelastic deformations of the building system, they are not sufficient alone. Rather, it was proposed that the earthquake demand should also be determined and compared with the deformation capacity from the pushover analysis in order to obtain the performance of the building.

4.2 Determination of Performance Levels and Objectives

In this part, performance levels for the CFS-RuC case study buildings are specified in accordance with TSC 2018 Section 3.4. The discrete structural performance levels are: Immediate Occupancy (IO), Limited Damage (LD), Controlled Damage or Life Safety (LS) and Collapse Prevention (CP). FEMA 274, 1997 [55] offers a clear perspective on what these performance levels represent, as shown in Fig. (4-1), which presents a load-deformation graph of a ductile structure and the performance levels are indicated by discrete points. As shown, the damage is not significant at the Immediate Occupancy level. At the Life Safety level, the structure has sustained considerable damage and it is noticed that its initial rigidity has notably decreased. Lastly, at the Collapse Prevention level, the structure have endured severe damage and beyond this point, the structure is susceptible to structural instability or collapse.

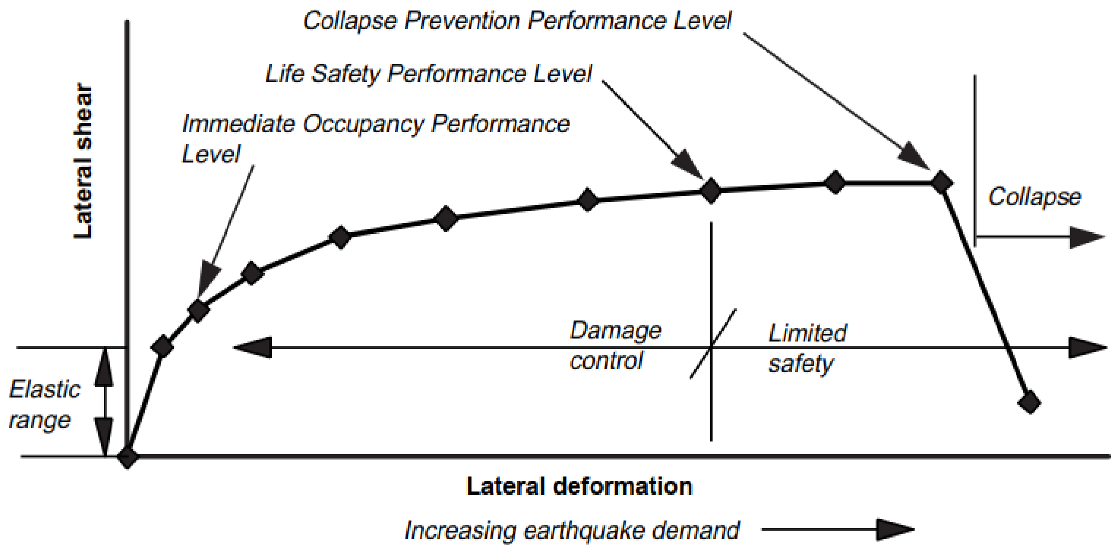

Figure 4-1. Performance and structural deformation demand for ductile structures [55]

Considering that the structure behaves in a ductile manner, Section15.3 of TSC 2018 describes corresponding damage conditions of the above-mentioned performance levels at the section level and these are Limited Damage (LD), Controlled Damage (CD), and Pre-collapse Damage (PD) conditions. Consequently, these damage conditions produce four different damage regions (limited damage region, distinctive damage region, extensive damage region, and collapse region) which are illustrated in Fig.(4-2).

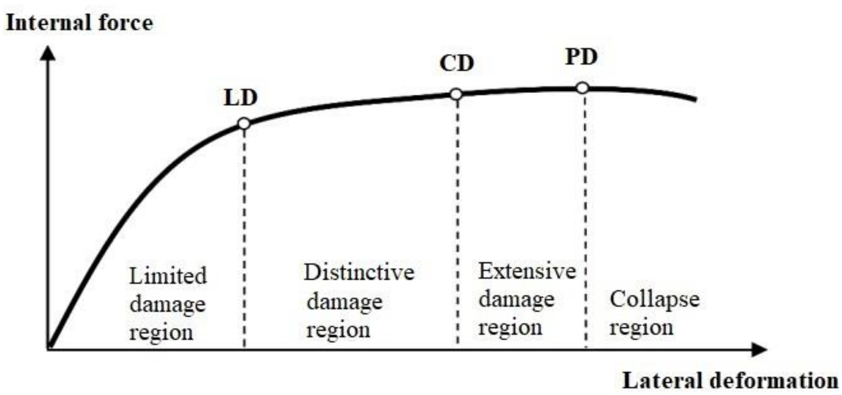

Figure 4-2. Damage conditions and regions [38]

Immediate Occupancy Structural Performance Level: the post-earthquake state in which very negligible structural damage has occurred. The pre-earthquake strength and stiffness of both lateral- and vertical-force bearing systems are assumed to remain intact in this performance level.

Limited Damage Structural Performance Level: This performance level is defined as the post-earthquake damage in which limited structural damages are present in the structure. In other words, the non-linear behavior is limited. It is usually preferred over the IO performance level for economic reasons. The damage distribution allowed for the LD performance level is subsequently detailed as follows.

'For any given storey in a building, in the results of an assessment performed for any earthquake direction in consideration, at most 20% of the beams are allowed to be situated in the Distinctive Damage region, but all other structural elements are to remain in the Limited Damage region. [38]'

Controlled Damage or Life Safety Structural Performance Level: This performance level corresponds to the post-earthquake state in which structural damages significantly occur but structural components are not heavily damaged to the level of causing life-threatening injury. Structural repair is possible to ensure life safety before reoccupancy. Similarly, the damage distribution is given in this way.

'For any given storey in a building, in the results of an assessment performed for any earthquake direction in consideration, apart from secondary beams that don't participate in the lateral force resisting system, maximum 35% of the beams are allowed to be situated in the Extensive Damage region. The level of vertical members that can be allowed in the Extensive Damage region can be deduced as explained in the paragraph below. [38]'

'The total contribution of the vertical elements in the Extensive Damage region to the shear force carried by the vertical elements at each floor should be below 20%. The ratio of the sum of the shear forces of the vertical elements in the Extensive Damage region on the top floor to the sum of the shear forces of all the vertical elements on that floor can be at most 40%. [38]'

Collapse Prevention Structural Performance Level: This level is the pre-collapse state where severe damage (permanent deformation) to the structural elements occurs, but the structure is still able to support gravity loads. Partial or total collapse of the building is prevented while notable strength and stiffness degradation is observed. Again, the damage distribution is explained as follows.

'For any given storey in a building, in the results of an assessment performed for any earthquake direction in consideration, apart from secondary beams that don't participate in the lateral force resisting system, maximum 20% of the beams are allowed to be situated in the Collapse region. Other components are allowed to be situated in the lower damage regions of Limited Damage, Distinctive Damage and Extensive Damage.'

As already discussed in Section 3.2 of this work, the CFS-RuC buildings are prescribed to meet the normal performance level of controlled damage (CD). Since this type of buildings are assumed to be residential, they can be assessed following the basic objective as recommended from TSC 2018 and SEAOC, 1995 [56]. Fig. (4-3) shows the relationship between seismic hazard and performance levels which permits the establishment of performance objectives. The objectives are classified according to the level of severity or impact a certain facility has if damaged. For example, facilities that handles toxic material are classified as a safety critical objective because of the impact they are likely to cause. Residential and commercial buildings are hence classified as basic objective.

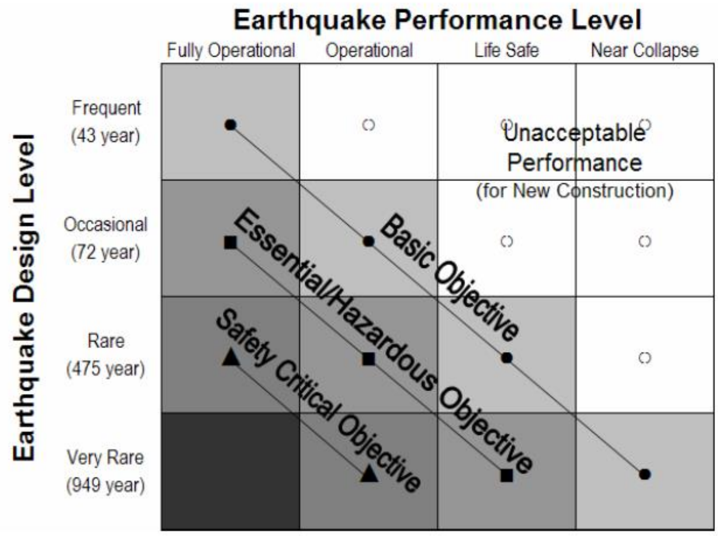

Figure 4-3. Recommended seismic performance objectives for buildings [56]

4.3 Analysis Procedure Selection

According to Section 5.5.2.1 of TSC 2018, for buildings with building height class, BHC ≥ 5, implementation of the nonlinear static pushover method is permitted for the seismic evaluation. Therefore, as already determined in Section 3.2 that the 8-story CFS-RuC building falls into the building height class of 5, the pushover method can easily be applied. Also, earlier in Section 3.2, it was demonstrated that no torsional irregularity was found in the 8-story building which fulfills the other condition, $\eta_{\mathrm{bi}} < 1.4$ from Section 5.6.2.2 of TSC 2018 for the applicability of pushover analysis method. Lastly, the modal participating mass ratio of dominant (first) mode of vibration was found to be greater than 0.7 from Table (3-5) and this satisfies the last condition required.

4.4 Nonlinear Static Pushover Analysis

Pushover analysis entails subjecting monotonically increasing lateral loads to a mathematical model of a building which has predefined nonlinear load-deformation characteristics of all components consisting the lateral force resisting system [50]. In this procedure, the results are obtained in terms of base shear force and lateral displacement of the control node which is usually selected as the mass center of the top floor. The lateral loads are proportionally applied at each floor diaphragm in respect to the mass distribution along the height of the building. This distribution needs to be also proportional to the shape of the dominant mode of vibration in the considered direction. The purpose of pushover analysis is to assess the seismic performance of a structural system in the inelastic range by predicting its strength and deformation demands. The assessment is based on different performance parameters, including overall drift, inter-story drift, inelastic element deformation, etc.

The static pushover analysis is an approximate method based on the theory that the response of the structure can be correlated to the response of an equivalent single degree-of-freedom (SDOF) system. It is assumed that the response is controlled by a single mode with a shape of mode maintained throughout the time history response. Although such assumptions may not be accurate, it has been demonstrated that they successfully predict the maximum seismic response of multi degree-of-freedom (MDOF) structures, given that a single mode dominates their behavior [57]. The equivalent SDOF system is not expressed in a unique way, however, the basic underlying assumption common to all approaches is that the deflected shape of the MDOF system can be represented by a shape vector $\{\Phi\}$ that doesn't change throughout the time history, irrespective of the deformation level. The governing differential equation of an MDOF system can be written as:

$$M\{\Phi\}\ddot{X}_t + C\{\Phi\}\dot{X}_t + Q = -M\{1\}\ddot{X}_g \tag{4-1}$$

Where M and C are the mass and damping matrices, Q denotes the story force vector, and $\ddot{X}_g$ is the ground acceleration.

Several analysis methods have been developed to alternatively estimate the displacement demand of the equivalent SDOF system resulting from the above shown differential Equation(4-1). The nonlinear time history analysis is the most basic method among various nonlinear analysis methods available for the analysis of existing buildings, however it is overly complex and impractical to use. Other simplified nonlinear analysis methods such as the capacity spectrum method and the displacement coefficient method are often preferred for their simplicity. However, the TSC 2018 code promote the implementation of the capacity spectrum method and provide modified procedures for it and they are briefly discussed in the following section.

4.5 Capacity Spectrum Method

The Capacity Spectrum Method (CSM) was first introduced in the work of Freeman (1978, SEAOC), where the possibility of expressing the spectral demands as a function of spectral displacement in place of period was examined. The capacity spectrum is a graphical method that uses the intersection of the capacity (pushover) curve and a response spectrum to estimate the maximum displacement. The general process of CSM method is extensively detailed in ATC 40 but it can be graphically summarized as shown in Fig. (4-4) which illustrates the estimation of the inelastic displacement from the capacity diagram and the spectra curve. The steps involved in the estimation of the inelastic displacement are as follows [58]:

1. The relationship between the base shear $\mathrm{V}_{\mathrm{tx1}}$ and the top displacement $u_{\mathrm{Nx1}}^{(\mathrm{X,k})}$, which defines the capacity (pushover) curve, is established.
2. The pushover curve is converted to the capacity diagram using Equation(4-2):

$$\mathrm{a}_1^{(X,\mathrm{k})} = \frac{\mathrm{V}_{\mathrm{tx1}}^{(X,\mathrm{k})}}{\mathrm{m}_{\mathrm{tx1}}^{(X,\mathrm{k})}} \quad , \quad d_1^{(\mathrm{X,k})} = \frac{u_{\mathrm{Nx1}}^{(\mathrm{X,k})}}{\Phi_{\mathrm{Nx1}}^{(1)}\Gamma_1^{(\mathrm{X,1})}} \; , \; and \;\; \Gamma_1^{(X,1)} = \frac{\mathrm{L}_{x1}}{\mathrm{M}_1} \tag{4-2}$$

where m_{tx1}= lumped mass at the i-th floor level, $\Phi_{N\times1}^{(1)}$ is the Nth-floor element (amplitude) of the first mode $\Phi_1^{(1)}$, N is the number of floors, and M_1 is the effective modal mass for the fundamental mode of vibration. $\Gamma_1^{(X,1)}$ is the modal participating ratio of the constant mode shape. a_1 and d_1 are spectral acceleration and displacement.

$$L_{x1} = \sum m_i \Phi_{N\times1}^{(1)} \quad \& \quad M_1 = \sum m_i \Phi_{Nx1}^{(1)}{}^2 \tag{4-3}$$

3. The standard format of the elastic response spectrum (Sae versus T_n) is converted to the $a_1 - d_1$ format and d_1 is the deformation spectrum ordinate used for the demand diagram derivation.
4. The capacity and demand diagrams obtained from the conversions of pushover and response spectrum curves are plotted together and the displacement demand is determined.
5. The obtained displacement demand is converted to global displacement and deformations of individual components. These values are then checked to ensure that they fall in the limits of the specified performance goals in Section 4.2.

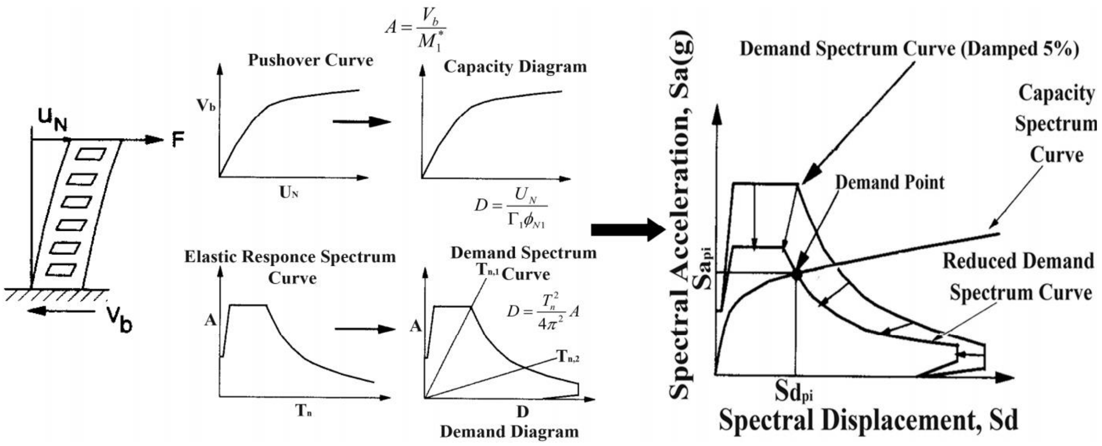

Figure 4-4. Procedure of determination of target point in the capacity spectrum method based on the acceleration-displacement response spectrum (ADRS) format [58]

4.6 Pushover Analysis in SAP2000

The modelling for nonlinear analysis procedures in SAP2000 [59] follows recommendations from TSC 2018 Section 5.4.1. Although it is advised in TSC 2018 to run the nonlinear procedures with 3D models, 2D models can still be used according to ASCE 41-17 Section 7.2.3 given that the building has rigid diaphragms and torsion effects are negligible. For the case study buildings both conditions are met. Therefore, the performance is conducted on a 2D frame moment-resisting frame (MRF), selected as the one within the red dashed rectangle in Fig. (4-5). This isolation is valid as only the selected frame and the last MRF on the opposite grid are wholly responsible for withstanding all the lateral force acting in the x-direction. So each of the two frame is expected to resist half the seismic response acting in the x-direction. It is also emphasized in ASCE 41-17 [60] that the connection which is weaker than or less ductile than the connected members are explicitly modeled in the analysis model. This explains again the purpose of the plastic hinge model developed in Chapter 2 that incorporates the elastic spring to account for the lower stiffness of the CFS-RuC semi-rigid connection.

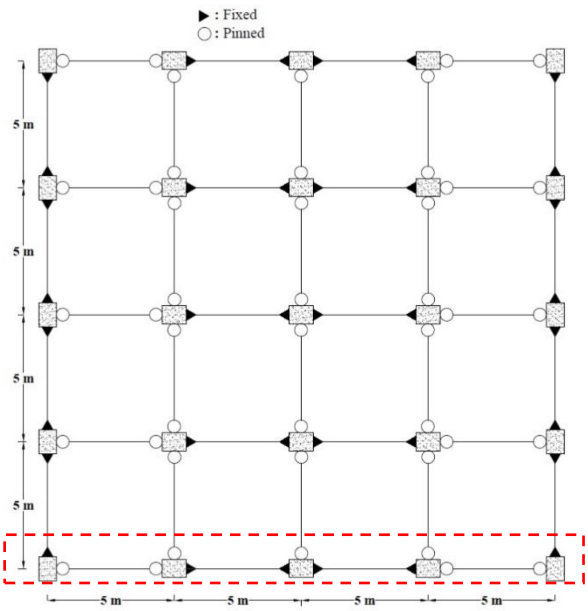

Figure 4-5. The selected 2D frame for nonlinear static procedures

Additionally, it is indicated that the second-order effects are to be accounted for in the analysis and here, they are simulated by introducing into the system leaning columns and applying all the gravity loading of the isolated system to them. Using the modelling parameters proposed for the connection configurations in the validation study (Chapter 2), both plastic and elastic spring properties are derived from Table (2-2) and are assigned to the indicated locations at the beam-ends. The plastic hinges of the beams are assigned as M3 hinges and the corresponding elastic spring is assigned using the end-release property available in SAP2000, where the connections initial rotational stiffness is entered. Fig. (4-6) shows an example of a M3 hinge created in SAP2000 for the CFSRuC-4-6#36-6-1250 connection. The component performance targets (IO, LS and CP) shown in this figure are developed following the suggestions of ASCE 41-13 Section7.6 [61] which provides alternative modeling parameters and acceptance criteria for elements that are not conventional (steel or RC) like in our case.

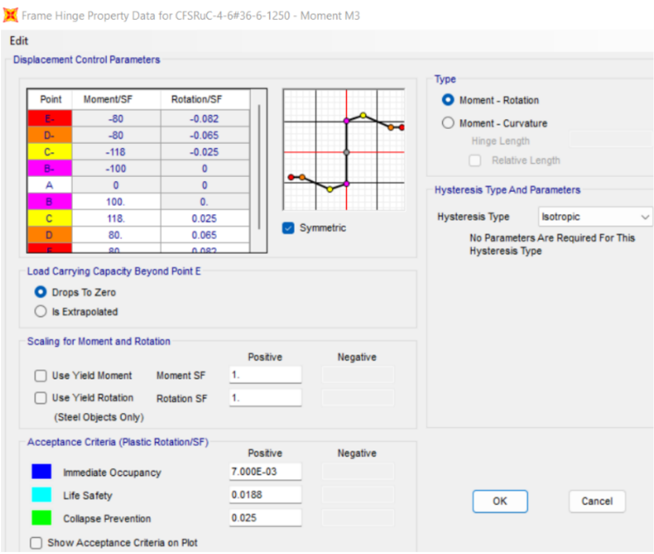

Figure 4-6. Frame hinge property data for CFSRuC-4-6#36SP6 beam

Considering that the moment-rotation responses used here are obtained from monotonic loading in ABAQUS, it is important to note that they may overestimate the strength and inelastic deformation capacity of the connection since in-cycle strength degradation often considered in cyclic procedures is not taken into account in monotonic loading. Despite that, ASCE 41-13 still permits using data from monotonic loading if they are the only ones available (which is the case in this study) but warns on their implications. From Fig. (4-6), according to Section C7.6.3 of ASCE 41-13, the derivation of deformations for the acceptance criteria shown for the three performance levels (IO, LS and CP) are described as follows: deformation for IO is taken as 0.67 times the deformation limit for life safety (LS). For life safety, it is taken as 0.75 times the deformation at point E or at collapse prevention. Finally, the deformation at CP is directly taken as the deformation at point E on the curve (see Fig.(4-7)). For column hinges, the appropriate approach to derive hinge properties for such new composite columns which are not covered in the literature is to opt for P-M3 fiber hinges, which consider the axial load-moment interaction and define the load-deformation characteristics of the section directly from its material definition and section dimensions.

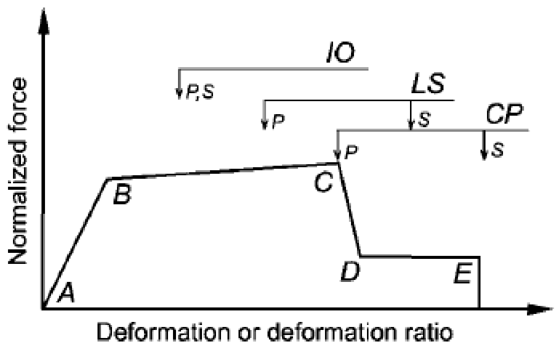

Figure 4-7. Acceptance criteria illustration [60]

Referring to procedures indicated for the nonlinear pushover analysis in TSC 2018, first the gravity loads of the system are incrementally applied to the system. The deformed shape and internal forces resulting from the first loading are used at the start of the nonlinear pushover load case. The gravity load case is determined according to the Equation (4-4). The integration of the vertical component of the earthquake in Equation (4-5) has been discussed before in chapter 3.

$$G + n\mathrm{Q} + 0.3E_{\mathrm{d}}^{(\mathrm{z})} \qquad \& \qquad E_{\mathrm{d}}^{(\mathrm{Z})} \approx \left(\frac{2}{3}\right) S_{\mathrm{DS}} G \tag{4-4}$$

Given that $S_{\mathrm{DS}} = 0.803$, the Equation(4-2) becomes

$$1.161G + 0.3\mathrm{Q} \tag{4-5}$$

After applying gravity loading represented by the final Equation (4-5) in the first nonlinear static case, a load pattern proportional to the fundamental mode of vibration is applied in the nonlinear pushover case and resulting pushover curves for all three case study building 2D-frames are presented in Figs. (4-8 to 4-10). To compare seismic performance of the proposed composite frame, bare versions of the composite CFS-RuC frames without RuC infill are also created. The sole purpose of incorporating the bare CFS 2D frames is to examine how the presence or absence of RuC infill affects the overall CFS-RuC system's behaviour.

The nonlinear static pushover analysis results can be used to evaluate lateral resistant capacities of all frames considered herein and also be used to estimate the potential ductility of CFS-RuC structures. As expected, all capacity curves of composite frames display a ductile behavior, meaning the systems underwent reasonable deformations without necessarily losing their strength. One can also argue that, for example the pushover curve of the 5- or 8-story bare frame also displays a ductile behavior, however this ductility is achieved because bare frames feature same steel connection elements (plate and number of screws) as the composite frames, hence similarity to a certain degree is to be observed in their seismic responses. Notice that all curves portray a deteriorating part, which indicates failure. This is due to the assignment of hinge overwrites property being assigned, which meshes the frame element around the hinge and so ensures good results. Moreover, considering the P-delta effects in the analyses might stimulate such behaviour too.

Comparing the results between the CFS-RuC frame and bare CFS steel frame in Fig. (4-8 to 4-10) is very crucial to understand the effect of the presence of rubberised concrete infill in the cold-formed steel tubes. As anticipated, the base shear capacities of CFS bare frames are low due to the lack of infill RuC that would restrain the outer steel section from local buckling and would allow the system to attain its full base shear capacity. This again shows how well the new composite system is equipped with desirable properties for seismic-resistant building design. This is proven by maintaining a good balance between high base shear capacity and adequate ductility. Moreover, less rigid initial stiffnesses from the pushover curves of bare frames are observed in comparison to their composite counterparts. This again can be associated with the lack of the RuC infill that has significant contribution to the overall rigidity of the semi-rigid connections. Again, this behavior of low rigidity for bare frames have been previously highlighted at the connection level analysis in Chapter 2. Graphically, it is also remarked that the difference in initial stiffnesses of composite and bare frames becomes very significant as the number of stories increases.

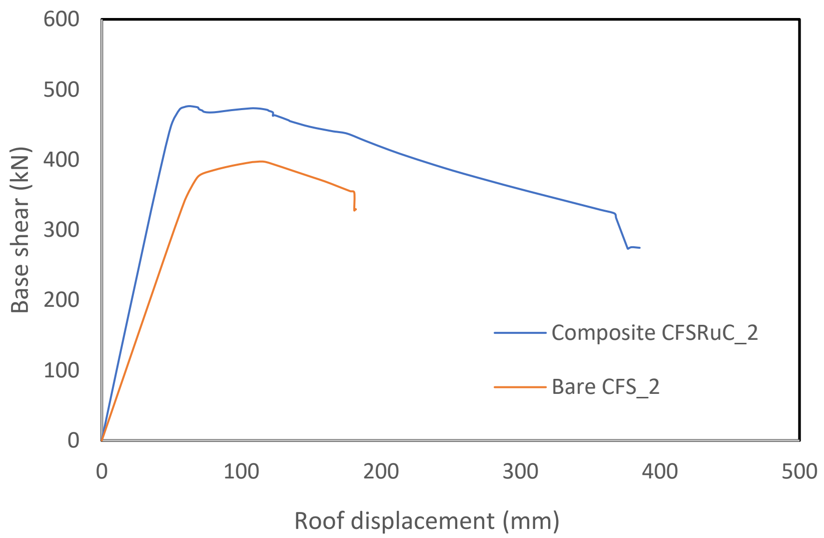

Figure 4-8. Pushover curves of the 2-story composite and bare frames

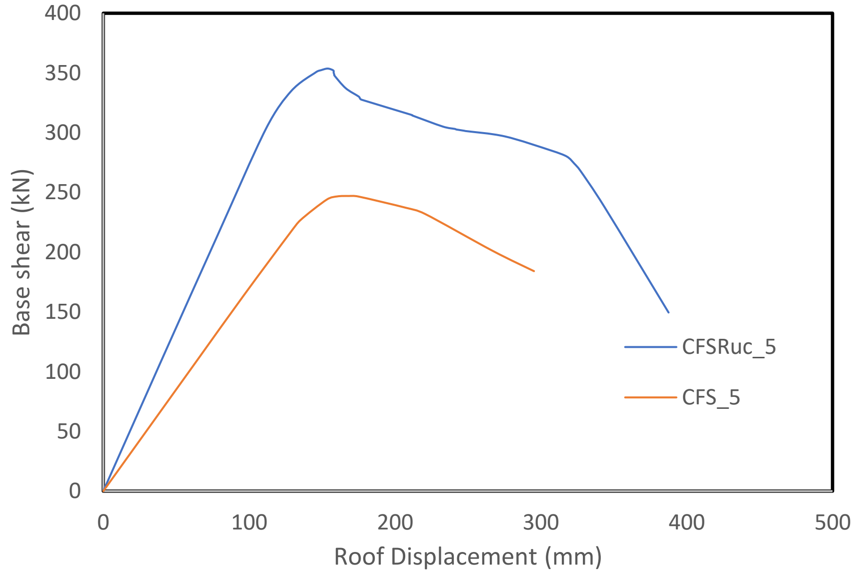

Figure 4-9. Pushover curves of the 5-story composite and bare frames

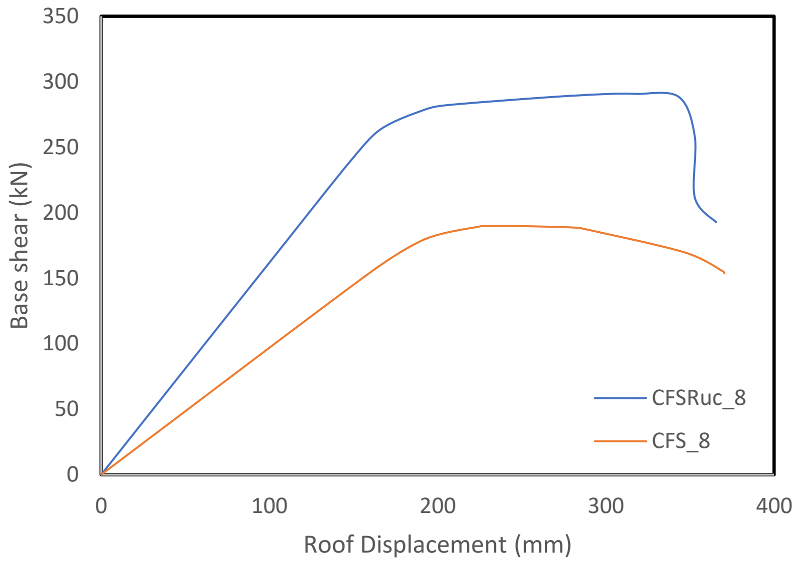

Figure 4-10. Pushover curves of the 8-story composite and bare frames

4.7 Estimation of the Target Displacement

The estimation of the target displacement follows steps already described in Section 4.1 and it is to be carried out only for the composite CFS-RuC frames. The capacity diagram is obtained by applying the Equations (4-2) and (4-3) to the pushover curve results and other required parameters to obtain the ADRS format are calculated and recorded in Table (4-1) accordingly.

Table 4-1. Parameters required for estimation of the target displacement

Floor	Weight (kN)	m_i	$\Phi_{Nx1}^{(1)}(m)$	$m_i\Phi_{N\times1}^{(1)}$	L_{x1}	$m_i\Phi_{Nx1}^{(1)\ 2}$	M_1	$\Gamma_1^{(X,1)}$
8	1214.75	123.83	0.00154	0.19	1.031	2.94E-04	0.0012	844.8
7	1374.625	140.12	0.00146	0.20		2.99E-04		
6	1374.625	140.12	0.00133	0.19		2.48E-04		
5	1374.625	140.12	0.00115	0.16		1.85E-04		
4	1374.625	140.12	0.00091	0.13		1.16E-04		
3	1374.625	140.12	0.00064	0.09		5.74E-05		
2	1374.625	140.12	0.00037	0.05		1.92E-05		
1	1374.625	140.12	0.00014	0.02		2.75E-06		

By drawing a tangent to the initial slope of the modal capacity diagram, its intersection with the demand spectrum is designated as the spectral displacement, Sde. Fig. (4-11), (4-12) and (4-13) summarize this process for the 2-, 5-, and 8-story frames. Alternatively, it can be obtained using Equation (4-6). Here the computation is done for the 8-story composite frame. The converting factor, Cr is taken as 1 since the period of the frame is greater than $T_{B,}$ corner period on the response spectrum. To convert back to the pushover curve format, the Equation(4-7) is applied and the actual target displacement, $u_{\mathrm{Nx1}}^{(\mathrm{X,k})}$ is obtained as shown.

$$d_{1,max}^{(X)} = S_{di}(T_1) = S_{de}(T_1) = \frac{T_1^2}{4\pi^2} g S_{ae}(T_1) = 0.206\, m \tag{4-6}$$

$$u_{\mathrm{Nx1}}^{(\mathrm{X,k})} = \Phi_{\mathrm{Nx1}}^{(1)} \Gamma_1^{(\mathrm{X,1})} d_{1,max}^{(\mathrm{X,k})} = 0.00154 \times 844.8 \times 0.206 = 0.268\, m \tag{4-7}$$

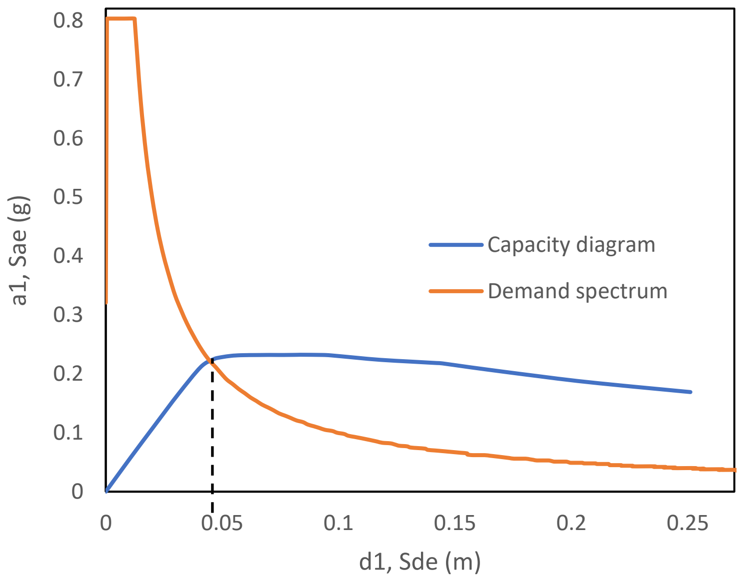

Figure 4-11. Determination of the target displacement for the 2-story frame

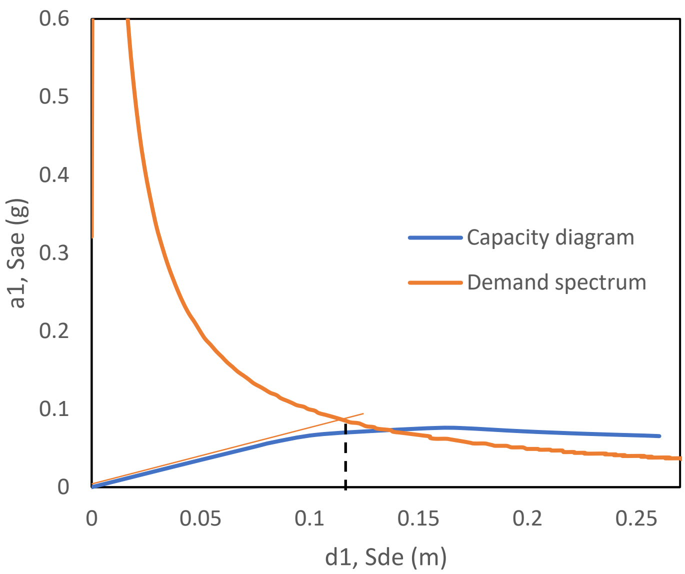

Figure 4-12. Determination of the target displacement for the 5-story frame

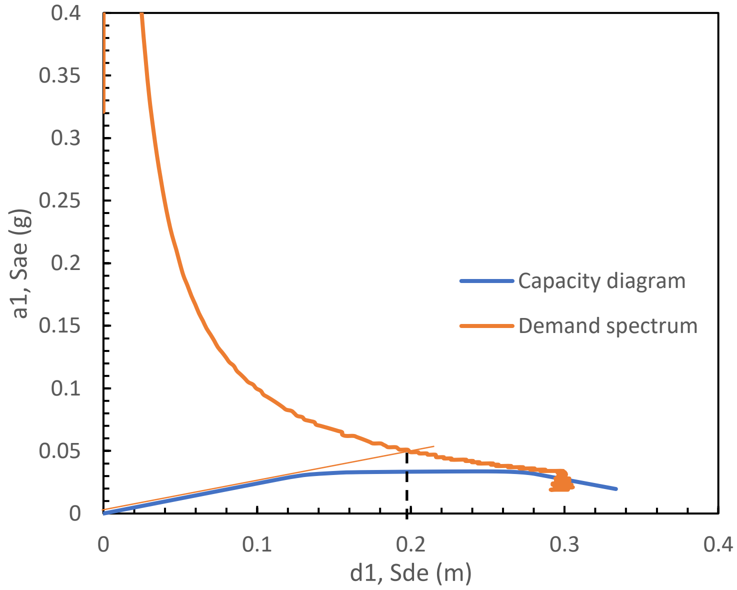

Figure 4-13. Determination of the target displacement for the 8-story frame

4.8 Performance-based Evaluation

Table (4-2) presents the target displacements calculated for all three composite frames and include parameters used for converting back from the ADRS format to the V_{tx}-u format (base shear vs roof displacement format). Figs. (4-14), (4-15) and (4-16) also show the plastic hinge distribution depicted when the pushover steps reach the estimated target displacements. It is recommended that evaluation of individual component deformations should be conducted at this stage thereby determine the performance of the frame systems according to the structural performance levels defined in Section (4.2). Thanks to the strong column-weak connection philosophy followed in the design of the frames, no damages observed for column members, therefore the performance assessment is done considering deformation of CFS-RuC beams only. Considering these frames under assessment are assumed to be residential buildings, they are required to meet the criteria of the controlled damage (CD) performance level which impose that in any given story, at most 35% of the beams are allowed to be situated in the Extensive Damage region (between LS-CP). In Fig. (4-14 to 4-16), all three composite frames do not show any beam member situated in the extensive damage region, all beam members deformations are constrained in the limited damage and distinctive damage regions which are accepted in the controlled damage performance level. Therefore, it is concluded that the composite CFS-RuC buildings designed for the Bayrampaşa case study fulfill the prescribed CD performance level.

Table 4-2. Estimation of the target displacement for all three frames

Frame	$S_{de}(T_1)(m)$	$d_{1,max}^{(X)}(m)$	$\Phi_{Nx1}^{(1)}$	$\Gamma_1^{(X)}$	$u_{\mathrm{Nx1}}^{(\mathrm{X})}(\mathrm{m})$
2-story	0.044	0.044	0.003	410	0.05412
5-story	0.117	0.117	0.0019	680	0.151164
8-story	0.206	0.206	0.00154	844.8	0.268004

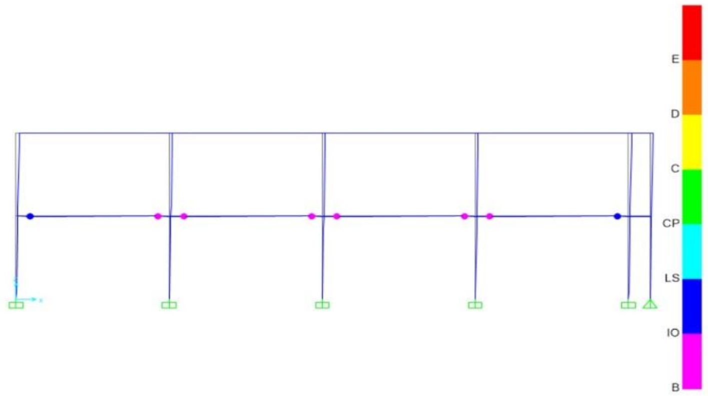

Figure 4-14. Progressive occurrence of plastic hinges at the target displacement for the 2-story frame

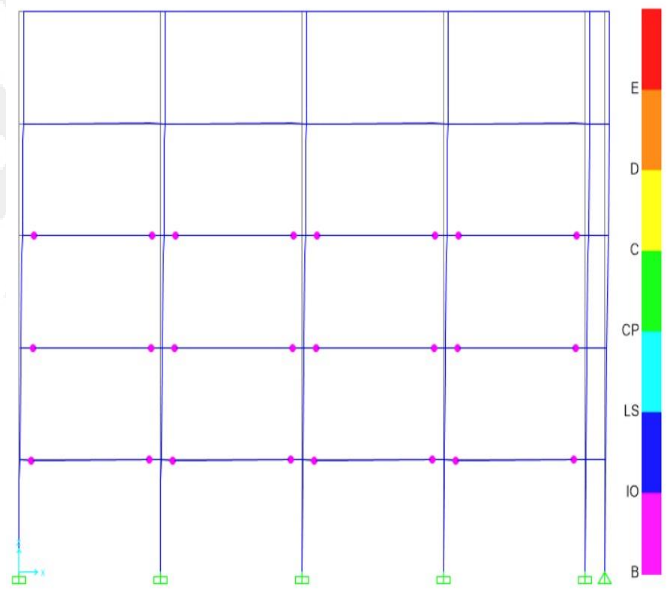

Figure 4-15. Progressive occurrence of plastic hinges at the target displacement for the 5-story frame

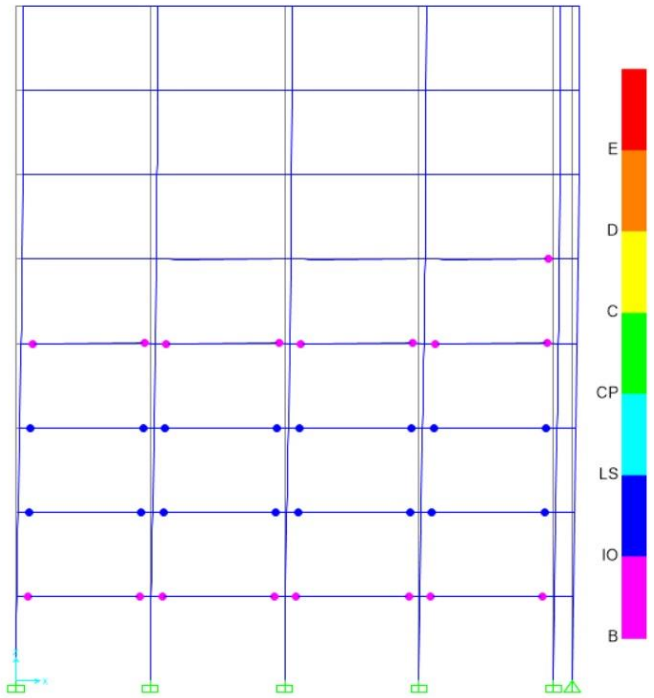

Figure 4-16. Progressive occurrence of plastic hinges at the target displacement for the 8-story frame

4.9 Pushover-Based Fragilities

In this part, a probabilistic approach to estimate the damage states of the CFS-RuC frames is employed. SPO2FRAG tool developed recently by [62], is adopted herein to produce fragilities of the case study buildings since it can provide pushover-based fragility curves for each limit-state basing on the pushover curve results inserted in the software. The features of the software permit direct input of the pushover curve values of the MDOF model, which is reported to a SDOF oscillator through a quadrilinear backbone normalization executed in the second step. The generated curve is subsequently the input of the SPO2IDA tool [63], which in return produces the IDA(Incremental Dynamic Analysis) curves for the 16, 50 and 84% fractiles [64].

Given the level of uncertainty associated with the ground motions used in the computation of IDAs, here a Gaussian probability distribution is implemented to calculate the mean and standard deviation of the CFS-RuC systems structural capacity. In the last step, MDOF effects in terms of non-linear behaviour and higher mode effects are accounted for in order to convert back to the initial model. These effects are represented in terms of fragility curves for each limit state, in the plane of intensity measure (IM) vs. engineering demand parameter (EDP) [64]. The results are identified in terms of median (Sa,50) and standard deviation (β), which are the fundamental parameters for tracking the fragility curves. In our case, the procedure has been applied to each pushover curve of the composite CFS-RuC frames. The limit-states and EDP values are derived directly on the pushover curve. While the EDP are well-defined, it is necessary to declare the IM parameter. In this case, according to the default IM parameter assumed by SPO2FRAG, the fragility curves have been obtained in terms of spectral acceleration of the SDOF oscillator period Sa(T*), where the T* completely relies on the approximation made on the SDOF pushover curve inserted to the software in the first step.

As reported in [62] a secant stiffness is embraced in the estimation of T* by considering the elastic portion of the pushover curve and it is configured to the 5–10% of the maximum base shear. In addition, the value of the MDOF effects inserted in the SPO2FRAG are estimated based on the sophistication level of the numerical models. The fragility curves obtained are shown in Fig. (4-17 to 4-19). The damage states DS1, DS2, DS3, and DS4 respectively stand for slight, moderate, severe and complete damage states derived according to formulas by Barbat et al [65]. With these fragility curves generated, they serve as a stochastic way to characterize the expected structural damages for any given level of seismic hazard. For example, it can be inferred from Fig. (4-17) that spectral accelerations between 0 and 0.5g for the 2-story frame do not impose severe damages to the structure.

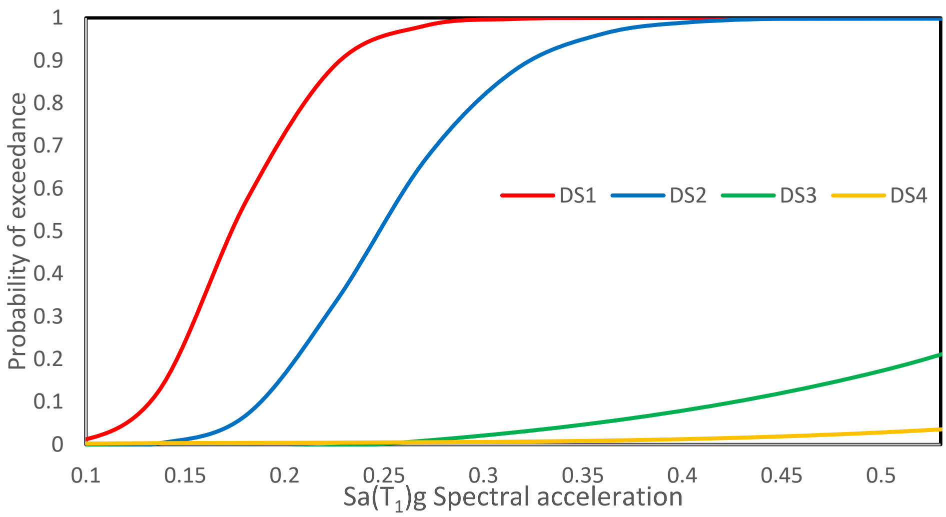

Figure 4-17. Fragility curves for the 2-Story CFS-RuC frame

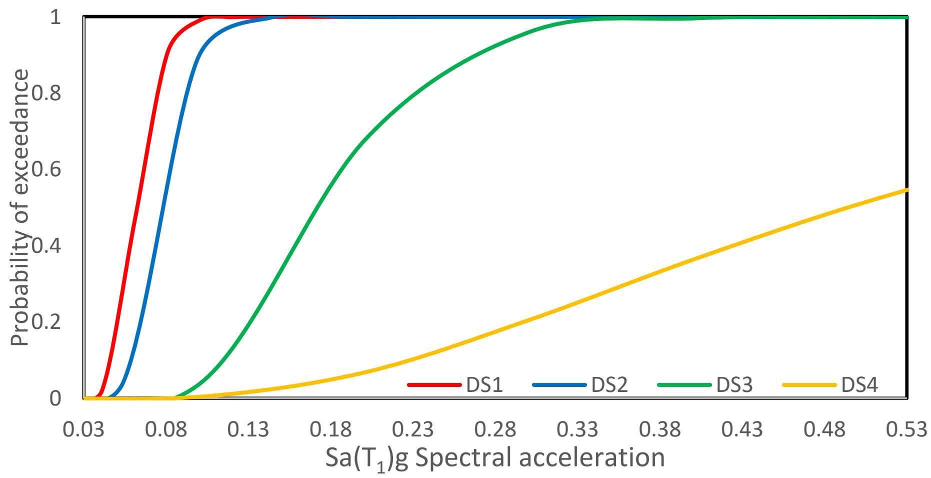

Figure 4-18. Fragility curves for the 5-Story CFS-RuC frame

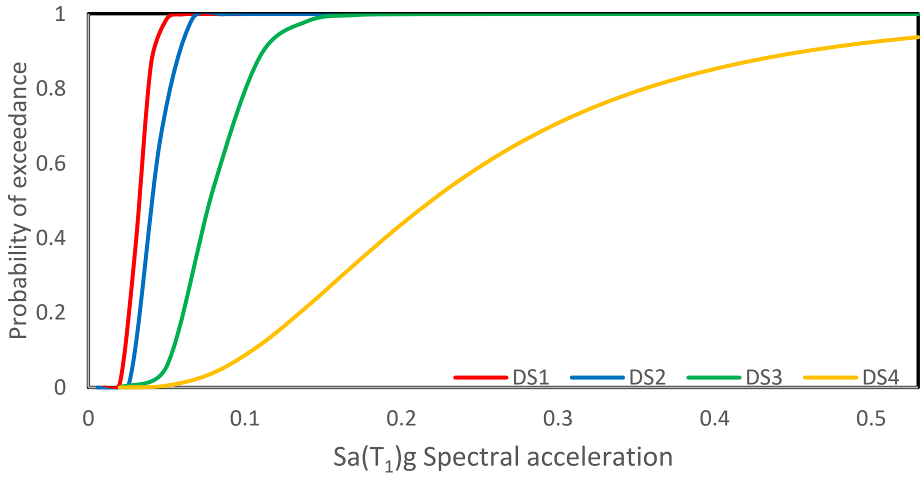

Figure 4-19. Fragility curves for the 8-Story CFS-RuC frame

CHAPTER V

SUMMARY AND CONCLUSION

This study performs numerical studies on a newly developed semi-rigid composite (cold formed steel and rubberized concrete) connection with the purpose of investigating the influence of various size of members on the connection response. In order to come up with a practical modeling protocol for frame-level analysis, a validation study is carried out by developing a plastic hinge model. Three case study composite buildings with different number of storeys (i.e 2, 5, and 8) are designed by fulfilling requirements of TSC 2018 and AISI-S100. Two configurations are used to assess the seismic performance of the case study buildings (i.e both bare and composite version of the CFS-RuC buildings). Nonlinear static pushover analyses are undertaken and the resulting capacity curves are used as input in the capacity spectrum method, which was implemented to evaluate the performance of the composite buildings at target displacement. Alternatively, SPO2FRAG tool that utilizes pushover curve to generate pushover-based fragility curves is employed. The following conclusions can be drawn:

1) The seismic behavior of the composite buildings featuring semi-rigid connections is adequate, as shown by the performance level of limited damage achieved by all three case study buildings.
2) The role played by side plates of the new connections in dissipating seismic energy is very crucial. So, connection configuration should limit damages to these plates in order to avoid unwanted limit states of ultimate and yield screw shear.
3) The practicality of RuC infill in eliminating or delaying unwanted local buckling limit state of the CFS members was vital to the moment-rotation response of the

semi-rigid connection.

4) The assessment of the connection rigidity has shown that all connections undertaken herein fall in the semi-rigid region of the Eurocode classification, with the composite connections exhibiting higher connection stiffness in comparison to their corresponding bare steel connections. This enhanced the energy dissipation capacity of composite CFS-RuC frames, while frames with bare connections experienced also a ductile behavior but with reduced lateral strength.
5) Unlike the capacity spectrum method that assess the building up to the target displacement, fragility curves from SPO2FRAG tool allows stochastic assessment of damage states of the composite buildings up to collapse.

Limitations

This study on a new composite CFS-RuC system employing semi-rigid connections is a preliminary study that attempts to highlight the potential of embracing the usage of RuC infill as a remedy to the premature local buckling of CFS elements through the restraining effect and while also contributing to the axial compressive capacity of the slender CFS sections. Moreover, the seismic behaviour of the semi-rigid moment resisting connection resulting from the integration of the composite column and beam is examined. Given that this composite system is newly introduced, very crucial parameters required in the performance assessment of such systems are not covered in the literature, hence too many assumptions had to be made and in most of the cases, conservative approaches were picked. Overall, limitations and items that restricted the scope of this study are as follows:

- The member level load-deformation characteristics used in the nonlinear static procedure were derived from FE analysis employing ‘monotonic’ loading, which does not account for cyclic strength deterioration as the cyclic loading does.

Consequently, the results from this seismic performance assessment should be used carefully considering this limitation.

- Apart from the above-stated, results from the numerical FE study were used to define the moment-rotation properties of the joints due to lack of enough experimental results to derive from. The proper way of deriving such properties is to base on the backbone curve of cyclic experiments.
- It is noteworthy that obtaining the falling parts of the connection response during the FE analyses was impractical for some connection configurations and mostly it was due to exceeding the allowable values of plastic deformations in shear force direction.
- As already mentioned, the lack of appropriate reduction factor, R for CFS-RuC systems was one of the biggest drawbacks. That is why an R factor from existing systems that could possess same behaviour as the one for CFS-RuC systems was assumed.
- For the design of composite CFS-RuC beams, the conservative side was chosen by ignoring the moment contribution of the RuC infill, however, for composite column design, RuC infill was relied on in axial compressive capacity calculations and this led to a simplified design of the column members. Studies that develop design procedures of the CFS-RuC columns are encouraged.
- Too much difficulty was faced in attempting to estimate the actual demand of this type of composite structure, since they neither have exactly the same demand as conventional steel nor as cold-formed steel structures. In other words, given that the CFS-RuC system features slender steel sections, the total axial load assigned for each column should be kept low (or add intermediate stud columns). However, in our case, this system was treated as conventional steel structure for dead load

estimation and eventually, high dead loads were assigned to be on the conservative side. As a result, deep sections had to be developed.

- Since the nature of the CFS-RuC section is rectangular, their connection design is complex. For example, at any given connection, both attaching column and beam sections should have the same width in order to achieve the semi-rigid connection adapted herein.
- Moreover, the demand of this composite CFS-RuC system is higher in comparison to that of typical CFS and much closer to the one of conventional steel or CFST structures. Thus approaches specific to the seismic design of this type of composite structures should be developed. In other words, CFS-RuC systems carry characteristics of both conventional CFS and those of CFST structures, so new design methods accounting for those different behavior should be implemented.

APPENDIX

A. FE Moment-rotation Curves for Joints with 195x350 Members

Due to the convergence issues encountered in the FE analyses of CFS-RuC connections, only successful M-tetha curves of the 195x350 sections are displayed in Fig.(A-1).

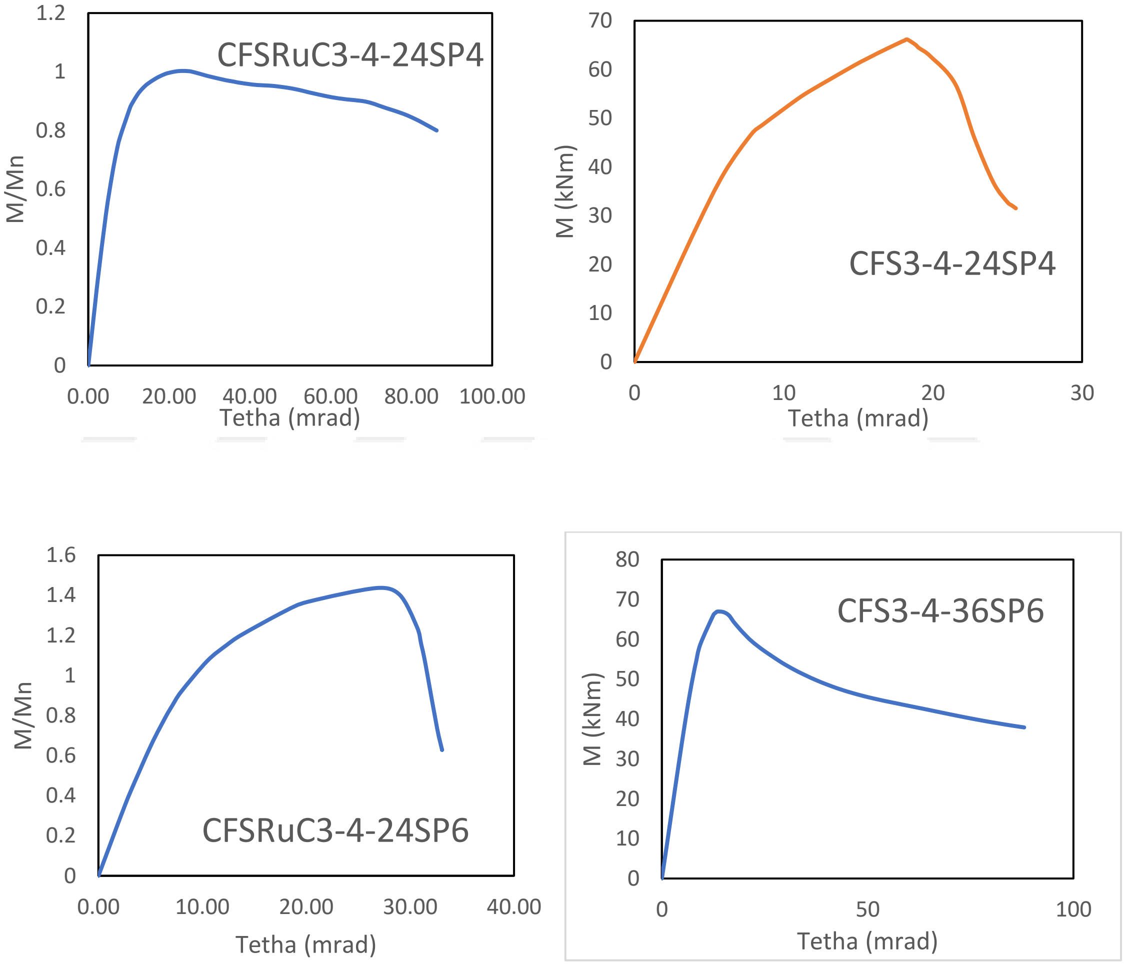

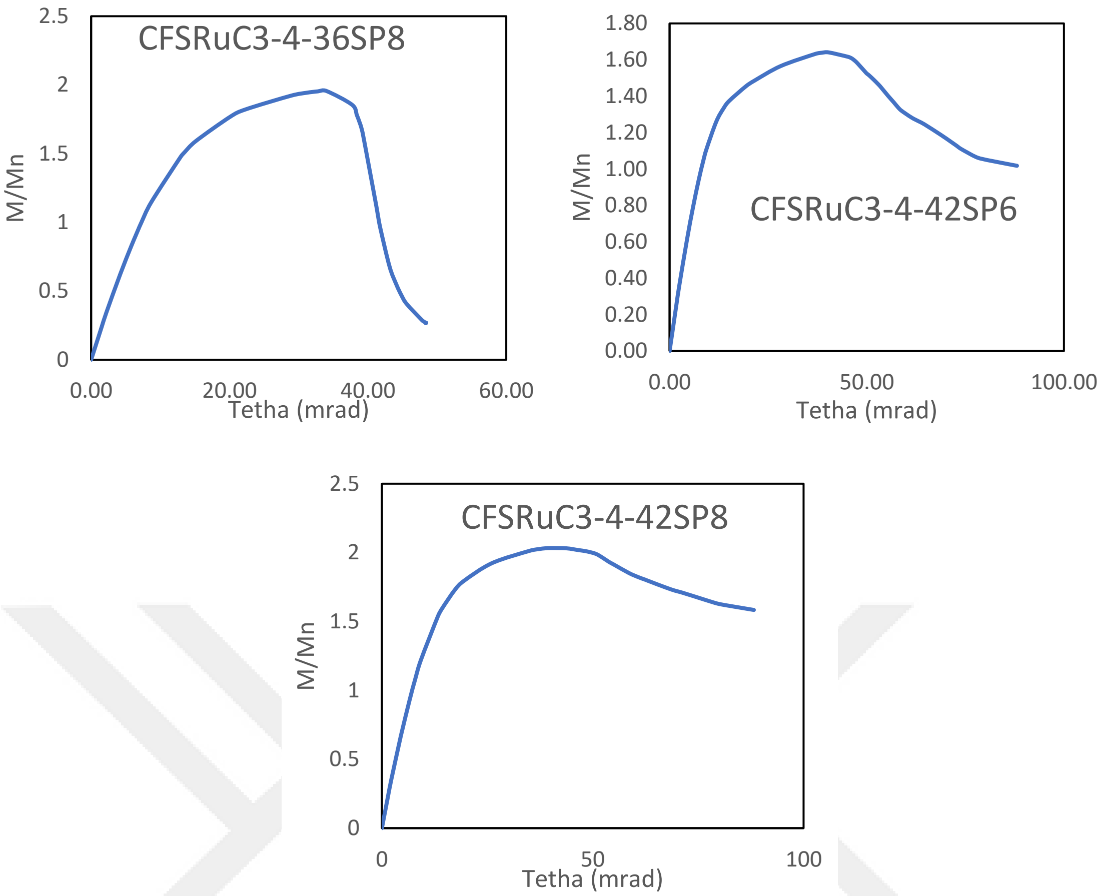

Figure A- 1 Moment-rotation curves from the parametric study of the 195x350 section

B. FE Moment-rotation Curves for Joints with 250x350 Members

It is noteworthy to highlight that the moment strength of M-tetha curves presented in Fig. (B-1) are not significantly larger than those of the 195x350 section since the connection moment is largely governed by the connection elements such as sideplate thickness and number of screws rather than the large dimensions.

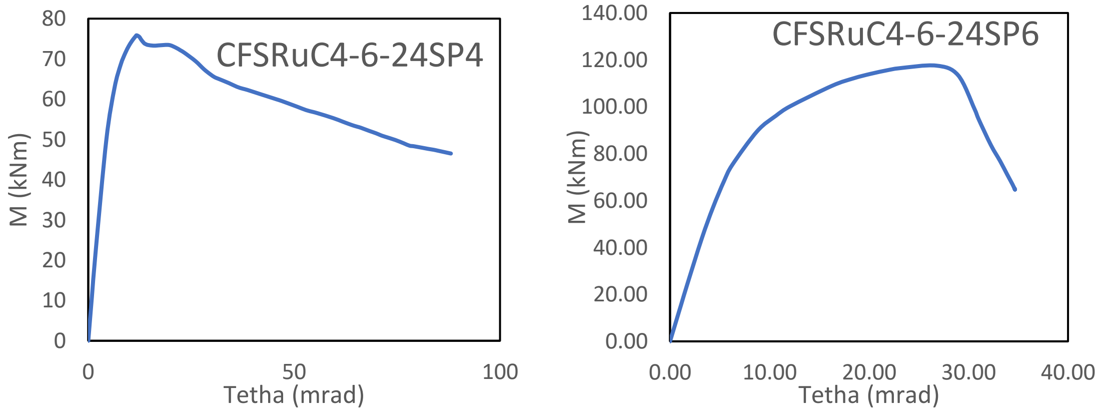

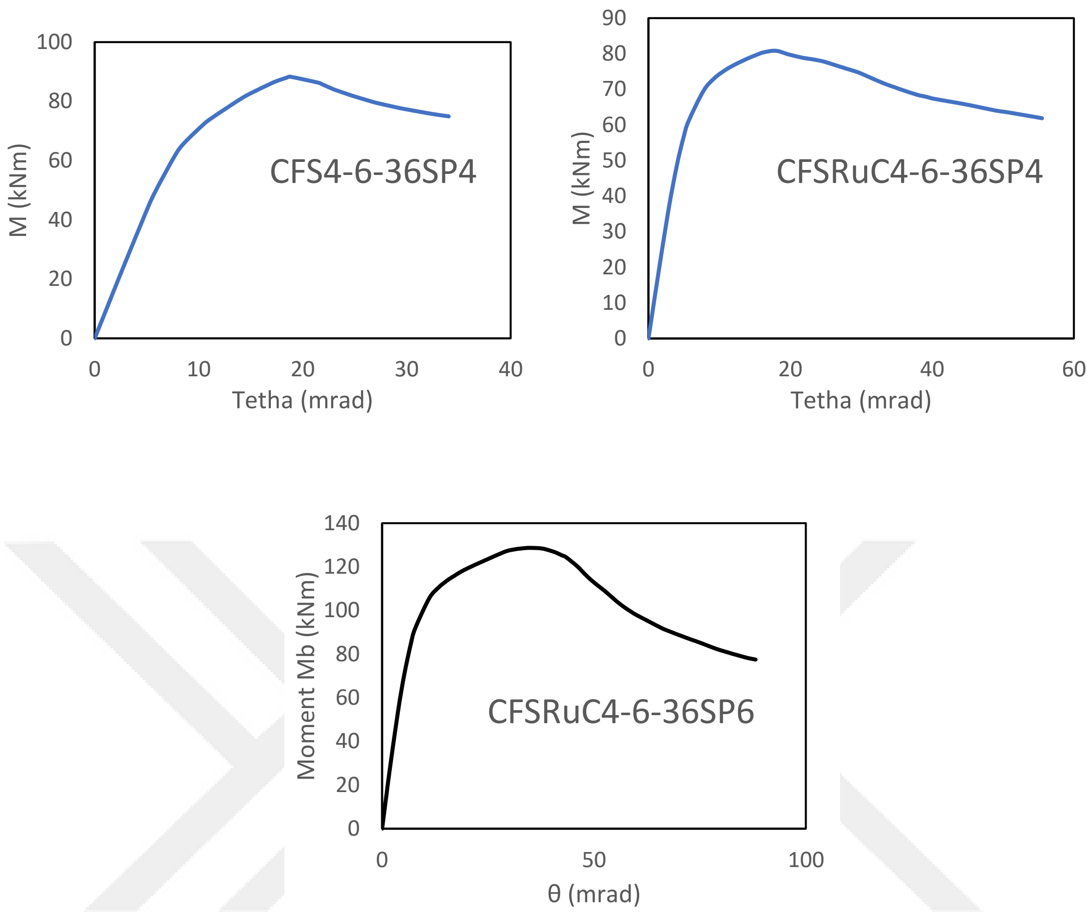

Figure B-1 Moment-rotation curves from the parametric study of the 250x350 section

C. Pushover Curve Data for the Case-study Frames

Table C-1 Capacity curve data of the 2-story CFSRuC frame

Steps	Base shear (kN)	Displacement (mm)
0	0.00	0.00
1	120.04	12.80
2	237.85	25.60
3	354.77	38.40
4	446.67	49.43
5	471.16	55.62
6	475.17	59.43
7	476.37	62.63
8	475.66	65.99
9	474.50	68.96
10	472.79	69.41
11	471.32	70.38

12	470.06	72.06
13	468.88	72.64
14	467.96	73.89
15	467.41	76.25
16	467.42	78.98
17	468.14	83.30
18	470.59	92.80
19	473.25	106.80
20	473.12	111.55
21	472.35	115.02
22	470.94	118.77
23	469.81	119.63
24	467.42	122.60
25	462.72	122.60
26	463.18	123.20
27	463.03	124.57
28	456.17	133.98
29	455.00	134.82
30	446.91	149.28
31	440.37	166.02
32	439.84	168.25
33	436.98	176.26
34	426.69	189.21
35	413.73	206.35
36	404.88	219.24
37	396.39	232.36
38	388.39	245.23
39	380.12	259.33
40	368.28	280.77
41	361.41	293.57
42	354.74	306.37
43	348.19	319.17
44	341.67	331.97
45	335.15	344.77
46	328.62	357.57
47	323.63	367.31
48	317.68	368.46
49	317.68	368.46
50	317.47	368.50
51	317.47	368.50
52	273.50	376.85
53	273.17	377.11
54	275.46	379.67
55	274.58	385.46

Table C-2 Capacity curve data of the 2-story bare frame

Steps	Base shear (kN)	Displacement (mm)
0	0.00	0.00
1	46.38	8.00
2	92.75	16.00
3	139.13	24.00
4	185.50	32.00
5	231.88	40.00
6	278.20	48.00
7	323.18	56.00
8	348.43	60.94
9	372.95	67.80
10	379.74	71.80
11	384.85	79.80
12	389.40	88.65
13	393.50	98.60
14	396.64	107.81
15	396.80	108.85
16	397.21	116.40
17	392.14	125.14
18	386.26	134.03
19	380.81	142.27
20	375.05	150.98
21	368.97	160.17
22	362.21	168.99
23	355.32	177.91
24	353.16	180.96
25	327.84	180.96
26	328.98	181.62
27	329.00	181.65
28	329.00	181.65
29	329.42	182.05
30	329.42	182.05
31	329.42	182.05
32	329.42	182.05
33	329.42	182.05

Table C-3 Capacity curve data of the 5-story CFSRuC frame

Steps	Base shear (kN)	Displacement (mm)
0	0.00	0.00
1	87.88	32.00
2	124.86	45.52
3	211.91	77.52
4	303.17	111.47
5	334.83	128.80

6	350.77	145.93
7	352.34	149.26
8	353.70	153.82
9	352.18	157.65
10	350.32	157.94
11	348.60	158.39
12	348.54	158.41
13	347.93	158.43
14	337.32	166.14
15	330.32	175.06
16	328.46	176.10
17	327.68	176.99
18	315.21	210.59
19	314.69	211.87
20	314.43	211.88
21	314.42	211.89
22	305.15	232.82
23	303.17	241.16
24	302.73	241.98
25	301.63	247.65
26	301.44	248.19
27	296.90	275.38
28	284.98	307.38
29	280.10	317.77
30	274.04	323.04
31	268.60	326.86
32	238.37	343.38
33	149.50	387.58

Table C-4 Capacity curve data of the 5-story bare frame

Steps	Base shear (kN)	Displacement (mm)
0	0.00	0.00
1	54.46	32.00
2	108.92	64.00
3	163.35	96.00
4	216.04	128.00
5	226.77	135.09
6	243.99	153.17
7	246.69	160.41
8	247.05	168.40
9	246.66	174.71
10	237.16	207.51
11	232.06	220.55
12	201.20	266.85
13	184.15	295.30

Table C-5 Capacity curve data of the 8-story CFSRuC frame

Steps	Base shear (kN)	Displacement (mm)
0	0.00	0.00
1	82.98	51.20
2	165.77	102.40
3	240.35	148.75
4	263.94	166.40
5	278.72	192.41
6	282.11	205.52
7	288.00	264.04
8	290.54	299.29
9	290.72	317.79
10	288.52	343.25
11	258.28	352.86
12	211.65	352.88
13	192.77	365.54

Table C-6 Capacity curve data of the 8-story bare frame

Steps	Base shear (kN)	Displacement (mm)
0	0.00	-0.01
1	154.94	160.54
2	179.80	192.44
3	189.67	225.79
4	189.80	229.70
5	190.01	239.41
6	189.10	272.63
7	188.50	283.07
8	188.24	284.98
9	169.90	346.32
10	155.27	369.59
11	153.69	370.48

REFERENCES

[1] A. W. Smyth, G. Altay, G. Deodatis, M. Erdik, , G. Franco, P. Gülkan, , & Ö. Yüzügüllü, “Probabilistic Benefit-Cost Analysis for Earthquake Damage Mitigation: Evaluating Measures for Apartment Houses in Turkey,” *Earthquake Spectra*, vol. 20, no. 1, pp. 171–203, Feb. 2004.

[2] A. Kashani, T. D. Ngo, P. Mendis, J. R. Black, and A. Hajimohammadi, “A sustainable application of recycled tyre crumbs as insulator in lightweight cellular concrete,” *Journal of Cleaner Production*, vol. 149, pp. 925–935, Apr. 2017.

[3] J. Xue and M. Shinozuka, “Rubberized concrete: A green structural material with enhanced energy-dissipation capability,” *Construction and Building Materials*, vol. 42, pp. 196–204, May 2013.

[4] D. C. Fratamico, “Experiments, analysis, and design of built-up cold-formed steel columns,” Doctoral dissertation, Johns Hopkins University, Baltimore, https://jscholarship.library.jhu.edu/handle/1774.2/62379 (accessed: Feb. 15, 2022).

[5] MJ Hough, RM Lawson. Proceedings of the Institution of Civil. Eng. – Civ. Eng.2019;172(6):17–44.

[6] A. Bagheri Sabbagh, N. Jafarifar, P. Davidson, and K. Ibrahimov, “Experiments on cyclic behaviour of cold-formed steel-rubberised concrete semi-rigid moment-resisting connections,” *Engineering Structures*, vol. 271, p. 114956, Nov. 2022.

[7] C. M. Uang, A. Sato, J.-K. Hong, and K. Wood, “Cyclic Testing and Modeling of Cold-Formed Steel Special Bolted Moment Frame Connections,” *Journal of Structural Engineering-asce*, vol. 136, no. 8, pp. 953–960, Aug. 2010.

[8] A. B. Sabbagh, M. Petkovski, K. Pilakoutas, and R. Mirghaderi, “Experimental work on cold-formed steel elements for earthquake resilient moment frame buildings,” *Engineering Structures*, vol. 42, pp. 371–386, Sep. 2012.

[9] A. Sato and C.-M. Uang, “Seismic Performance Factors for Cold-Formed Steel Special Bolted Moment Frames,” *Journal of Structural Engineering*, vol. 136, no. 8, pp. 961–967, Aug. 2010.

[10] P. Kirk, Design of a cold formed section portal frame building system, in: Proc. 8th Int. Speciality Conf. on Cold-Formed Steel Structures, Vol. 259, Univ.of Missouri-Rolla, St. Louis, MO, 1986.

[11] S. M. Mojtabaei, M. Z. Kabir, I. Hajirasouliha, and M. Kargar, “Analytical and experimental study on the seismic performance of cold-formed steel frames,” *Journal of Constructional Steel Research*, vol. 143, pp. 18–31, Apr. 2018.

[12] J. B. P. Lim, G. J. Hancock, G. Charles Clifton, C. H. Pham, and R. Das, “DSM for ultimate strength of bolted moment-connections between cold-

formed steel channel members,” *Journal of Constructional Steel Research*, vol. 117, pp. 196–203, Feb. 2016.

[13] D. Dubina, A. Stratan, and Z. Nagy, “Full – scale tests on cold-formed steel pitched-roof portal frames with bolted joints,” pp. 175–194, Jan. 2009.

[14] L. Yin, Y. Niu, , G. Quan, H. Gao, & J. Ye, ‘Development of new types of bolted joints for cold-formed steel moment frame buildings’’. *Journal of Building Engineering*, *50*, p. 104171, Jun. 2022.

[15] J. Ye, S. M. Mojtabaei, and I. Hajirasouliha, “Seismic performance of cold-formed steel bolted moment connections with bolting friction-slip mechanism,” *Journal of Constructional Steel Research*, vol. 156, pp. 122–136, May 2019.

[16] A. B. Sabbagh, M. Petkovski, K. Pilakoutas, and R. Mirghaderi, “Ductile moment-resisting frames using cold-formed steel sections: An analytical investigation,” *Journal of Constructional Steel Research*, vol. 67, no. 4, pp. 634–646, Apr. 2011.

[17] A. B. Sabbagh, N. Jafarifar, D. Deniz, and S. Torabian, “Development of composite cold-formed steel-rubberised concrete semi-rigid moment-resisting connections,” *Structures*, vol. 40, pp. 866–879, Jun. 2022.

[18] S. Costanzo, M. D’Aniello, and R. Landolfo, “Seismic design criteria for Chevron CBFs: European vs North American codes (Part-1),” *Journal of Constructional Steel Research*, vol. 135, pp. 83–96, Aug. 2017.

[19] C. Molina Hutt, I. Almufti, M. Willford, and G. Deierlein, “Seismic Loss and Downtime Assessment of Existing Tall Steel-Framed Buildings and Strategies for Increased Resilience,” *Journal of Structural Engineering*, vol. 142, no. 8, Aug. 2016.

[20] L.-H. Han, W. Li, and R. Bjorhovde, “Developments and advanced applications of concrete-filled steel tubular (CFST) structures: Members,” *Journal of Constructional Steel Research*, vol. 100, pp. 211–228, Sep. 2014.

[21] R. Li, ‘Seismic properties of joints composed of CFST columns and RBS composite beams’’ (Doctoral dissertation, Western Sydney University (Australia)), 2016.

[22] K. Thirunavukkarasu, E. Kanthasamy, P. Gatheeshgar, K. Poologanathan, H. Rajanayagam, T. Suntharalingam, & M. Dissanayake, “Sustainable Performance of a Modular Building System Made of Built-Up Cold-Formed Steel Beams,” *Buildings*, vol. 11, no. 10, p. 460, Oct. 2021.

[23] O. Iuorio, V. Macillo, M. T. Terracciano, T. Pali, L. Fiorino, and R. Landolfo, “Seismic response of Cfs strap-braced stud walls: Experimental investigation,” *Thin-Walled Structures*, vol. 85, pp. 466–480, Dec. 2014.

[24] H.-W. Tian, Y.-Q. Li, and C. Yu, “Testing of steel sheathed cold-formed steel trussed shear walls,” *Thin-Walled Structures*, vol. 94, pp. 280–292, Sep. 2015.

[25] AISC. American, *Seismic provisions for structural steel buildings*. Chicago, Ill.: American Institute Of Steel Construction, 2016.

[26] I. Papargyriou, S. M. Mojtabaei, I. Hajirasouliha, J. Becque, and K. Pilakoutas, “Cold-formed steel beam-to-column bolted connections for seismic applications,” *Thin-Walled Structures*, vol. 172, p. 108876, Mar. 2022.

[27] S. Raffoul, R. Garcia, K. Pilakoutas, M. Guadagnini, and N. F. Medina, “Optimisation of rubberised concrete with high rubber content: An experimental investigation,” *Construction and Building Materials*, vol. 124, pp. 391–404, Oct. 2016.

[28] E. Güneyisi, “Fresh properties of self-compacting rubberized concrete incorporated with fly ash,” *Materials and Structures*, vol. 43, no. 8, pp. 1037–1048, Oct. 2010.

[29] R. Bušić, I. Miličević, T. K. Šipoš, and K. Strukar, “Recycled Rubber as an Aggregate Replacement in Self-Compacting Concrete—Literature Overview,” *Materials*, vol. 11, no. 9, Sep. 2018.

[30] A. Silva, Y. Jiang, J. M. Castro, N. Silvestre, and R. Monteiro, “Experimental assessment of the flexural behaviour of circular rubberized concrete-filled steel tubes,” *Journal of Constructional Steel Research*, vol. 122, pp. 557–570, Jul. 2016.

[31] M. Elchalakani, “High strength rubberized concrete containing silica fume for the construction of sustainable road side barriers,” *Structures*, vol. 1, pp. 20–38, Feb. 2015.

[32] M. Emiroglu, M. H. Kelestemur, & S. Yildiz, ‘An investigation on ITZ microstructure of the concrete containing waste vehicle tire’’. In *Proceedings of 8th international fracture conference* (pp. 453-459), Nov. 2007.

[33] M. Dong, M. Elchalakani, A. Karrech, M. F. Hassanein, T. Xie, and B. Yang, “Behaviour and design of rubberised concrete filled steel tubes under combined loading conditions,” *Thin-Walled Structures*, vol. 139, pp. 24–38, Jun. 2019.

[34] A. Silva, Y. Jiang, J. M. Castro, N. Silvestre, and R. Monteiro, “Experimental assessment of the flexural behaviour of circular rubberized concrete-filled steel tubes,” *Journal of Constructional Steel Research*, vol. 122, pp. 557–570, Jul. 2016.

[35] R. Rahnavard, H. D. Craveiro, R. A. Simões, L. Laím, and A. Santiago, “Buckling resistance of concrete-filled cold-formed steel (CF-CFS) built-up short columns under compression,” *Thin-Walled Structures*, vol. 170, p. 108638, Jan. 2022.

[36] Abaqus Analysis User’s Manual. version 6.21; 2019.

[37] A. Bagheri Sabbagh, N. Jafarifar, D. Deniz, and S. Torabian, “Development of composite cold-formed steel-rubberised concrete semi-rigid moment-resisting connections,” *Structures*, vol. 40, pp. 866–879, Jun. 2022.

[38] Disaster and Emergency Management Agency (AFAD), Turkish Seismic Code 2018, TSC 2018, 2018.

[39] W. G. Altman, Atorod Azizinamini, J. H. Bradburn, and J.B. Radziminski, “Moment-rotation characteristics of semi-rigid steel beam-column connections,” Jun. 1982.

[40] X. L. Zhao, L.-H. Han, and H. Lu, *Concrete-filled tubular members and connections*. Abingdon, Oxon ; New York, Ny: Routledge, 2017.

[41] Turkish Standard Instution (TSE), TS EN 1991-1-3: Actions on structures-Part 1-3: General actions–Snow loads (Eurocode 1), Ankara, Türkiye, 2007.

[42] Istanbul Municipality, ‘Earthquake risk management department, soil classification maps per the earthquake code’ http://www.ibb.gov.tr/tr-TR/SubSites/DepremSite/Documents/EK16_Zemin_Siniflamasi_Haritasi (accessed June 21, 2022).

[43] ASCE 7-22, American Society of Civil Engineers. Minimum design loads and associated criteria for buildings and other structures. American Society of Civil Engineers, 2022.

[44] Code, P. Eurocode 8: Design of structures for earthquake resistance-part 1: general rules, seismic actions and rules for buildings. *Brussels: European Committee for Standardization,2005*.

[45] S. Etli and E. Güneyisi, “Assessment of Seismic Behavior Factor of Code-Designed Steel–Concrete Composite Buildings,” vol. 46, no. 5, pp. 4271–4292, May 2021.

[46] Republic of Turkey Ministry of Environment and Urbanisation, Turkish specification for the design, calculation and construction of steel structures TCSC2016, 2016.

[47] Z. B. Li and B. W. Schafer, “Buckling Analysis of Cold-formed Steel Members with General Boundary Conditions Using CUFSM Conventional and Constrained Finite Strip Methods,” Jan. 2010.

[48] AISI-S100-16. North American Specification for the Design of Cold-Formed Steel Structural Members. Washington, D.C.: American Iron and Steel Institute; 2016.

[49] N. Torunbalci, & G. Ozpalanlar ‘Earthquake response analysis of mid-story buildings isolated with various seismic isolation techniques’’ . In *The 14th World Conference on Earthquake Engineering, Beijing, China, Oct. 2008*.

[50] ATC, Seismic Evaluation and Retrofit of Concrete Buildings, Report ATC-40; Applied Technology Council. Redwood City, CA, U.S.A, 1996.

[51] K. A. Porter, ‘An overview of PEER’s performance-based earthquake engineering methodology’’. In *Proceedings of ninth international conference on applications of statistics and probability in civil engineering* (pp. 1-8).

[52] FEMA-273, NEHRP guidilines for the seismic rehabilitation of buildings, 1997.

[53] FEMA-356, Prestandard and commentary for the seismic rehabilitation of buildings, 2000.

[54] A. K. Chopra and R. K. Goel, “Capacity-Demand-Diagram Methods for Estimating Seismic Deformation of Inelastic Structures: SDF Systems,” Jan. 1999.

[55] FEMA-274, NEHRP commentary on the guidilines for the seismic rehabilitation of buildings, 2000.

[56] Recommended lateral force requirements and commentary. Seismology Committee, Structural Engineers Association of California, SEAOC, Sacramento, CA, 1988.

[57] M. S. Saiidi and M. A. Sozen, “Simple Nonlinear Seismic Analysis of R/C Structures,” *Journal of the Structural Division*, vol. 107, no. 5, pp. 937–953, May 1981.

[58] A. K. Chopra and R. K. Goel, “Capacity-Demand-Diagram Methods for Estimating Seismic Deformation of Inelastic Structures: SDF Systems,” Jan. 1999.

[59] CSI, “SAP2000 Integrated Software for Structural Analysis and Design,” Computers and Structures Inc., Berkeley, California.

[60] ASCE/SEI 41-17, Seismic Evaluation and Retrofit of Existing Buildings. Reston, VA: American Society of Civil Engineers; 2017

[61] ASCE/SEI 41-13, Seismic Evaluation and Retrofit of Existing Buildings. Reston, VA: American Society of Civil Engineers; 2013

[62] G. Baltzopoulos, R. Baraschino, I. Iervolino, and D. Vamvatsikos, “SPO2FRAG: software for seismic fragility assessment based on static pushover,” *Bulletin of Earthquake Engineering*, vol. 15, no. 10, pp. 4399–4425, May 2017.

[63] D. Vamvatsikos and C. Allin Cornell, “Direct estimation of the seismic demand and capacity of oscillators with multi-linear static pushovers through IDA,” *Earthquake Engineering & Structural Dynamics*, vol. 35, no. 9, pp. 1097–1117, 2006

[64] S. Ruggieri, F. Porco, and G. Uva, “A practical approach for estimating the floor deformability in existing RC buildings: evaluation of the effects in the structural response and seismic fragility,” *Bulletin of Earthquake Engineering*, vol. 18, no. 5, pp. 2083–2113, Dec. 2019.

[65] A. H. Barbat, L. G. Pujades, and N. Lantada, “Seismic damage evaluation in urban areas using the capacity spectrum method: Application to Barcelona,” *Soil Dynamics and Earthquake Engineering*, vol. 28, no. 10, pp. 851–865, Oct. 2008.

VITA

Dieudonne Iraguha graduated from Byimana School of Sciences (Rwanda) in November 2014, where he developed a strong interest in the engineering field. Later on, he was selected for a highly selective scholarship program to pursue his undergraduate degree in Civil Engineering at Akdeniz University and graduated in July 2020. Following the completion of his undergraduate studies, he enrolled at Özyeğin University to undertake a research-focused Master's degree, while also serving as a Graduate Teaching and Research Assistant. His thesis work is about the assessment of the lateral resistance of low-carbon seismic-resistant buildings. His current research interests are in Cold-Formed Steel, Performance-Based Design, and Thin-Walled Structures.